

Morphological Demographics of Galaxies at $z \sim 10\text{--}16$: Log-Normal Size Distribution and Exponential Profiles Consistent with the Disk Formation Scenario

YOSHIAKI ONO ¹, MASAMI OUCHI ^{2,1,3}, YUICHI HARIKANE ¹, HIDENOBU YAJIMA ⁴, KIMIHIKO NAKAJIMA ²,
SEIJI FUJIMOTO ⁵, MINAMI NAKANE ^{1,6} AND YI XU ^{1,7}

¹Institute for Cosmic Ray Research, The University of Tokyo, 5-1-5 Kashiwanoha, Kashiwa, Chiba 277-8582, Japan

²National Astronomical Observatory of Japan, 2-21-1 Osawa, Mitaka, Tokyo 181-8588, Japan

³Kavli Institute for the Physics and Mathematics of the Universe (WPI), The University of Tokyo, 5-1-5 Kashiwanoha, Kashiwa-shi, Chiba, 277-8583, Japan

⁴Center for Computational Sciences, University of Tsukuba, Ten-nodai, 1-1-1 Tsukuba, Ibaraki 305-8577, Japan

⁵Department of Astronomy, The University of Texas at Austin, Austin, TX 78712, USA

⁶Department of Physics, Graduate School of Science, The University of Tokyo, 7-3-1 Hongo, Bunkyo, Tokyo 113-0033, Japan

⁷Department of Astronomy, Graduate School of Science, The University of Tokyo, 7-3-1 Hongo, Bunkyo, Tokyo 113-0033, Japan

ApJ in press

ABSTRACT

We homogeneously investigate the morphological properties of 169 galaxies at $z \sim 10\text{--}16$ with deep JWST NIRC*am* images employing our established techniques of GALFIT modeling and uncertainty evaluation (systematics+statistics). We obtain effective radii r_e ranging 20–500 pc, with a distribution significantly broader than the scatter made by the uncertainties. We find that the r_e distribution is well described by a log-normal distribution with a mean of $r_e = 133^{+13}_{-12}$ pc and a standard deviation of $\sigma_{\ln r_e} = 0.52 \pm 0.08$. The standard deviation is comparable to that of local galaxies, indicating no significant evolution over $z \sim 0\text{--}10$. We also find that the axis ratio distribution is nearly uniform, statistically similar to that of local spirals. We estimate the virial radius r_{vir} from the stellar masses via the star-formation main sequence and stellar-to-halo mass relation, obtaining a stellar-to-halo size ratio $r_e/r_{\text{vir}} = 0.015^{+0.015}_{-0.005}$, which is comparable to those of star-forming galaxies in the local and low- z Universe. Our results of 1) the log-normal r_e distribution, 2) the uniform axis ratio distribution, and 3) a mean radial profile consistent with an exponential profile ($n = 1.3 \pm 0.6$) suggest that galaxies at $z \sim 10\text{--}16$ generally follow the classical galaxy disk formation scenario with a specific disk angular momentum fraction of $j_d/m_d \sim 0.5\text{--}1$. Interestingly, we identify two remarkable outliers GN-z11 ($z_{\text{spec}} = 10.60$) and GHZ2 ($z_{\text{spec}} = 12.34$) with $r_e = 55^{+5}_{-6}$ pc and 39 ± 11 pc, respectively, that may not be explained by disk structures but by AGN or compact star-forming galaxies merging underway in short periods of time, as reproduced in numerical simulations.

Unified Astronomy Thesaurus concepts: High-redshift galaxies (734); Lyman-break galaxies (979); Galaxy evolution (594); Galaxy formation (595); Galaxy structure (622); Galaxy radii (617); Galaxies (573); Galactic and extragalactic astronomy (563)

1. INTRODUCTION

Morphological properties of galaxies play a vital role in characterizing galaxy evolution (Conselice 2014; Stark et al. 2025). Thanks to the superior spatial resolution and sensitivity of NIRC*am* (Rieke et al. 2005; Rieke et al. 2023b) onboard the James Webb Space Telescope (JWST; Gardner et al. 2006; Gardner et al. 2023; McElwain et al. 2023), significant progress has been made in investigating the morphological properties

of high- z star-forming galaxies primarily found based on their rest-frame UV spectral features (Yang et al. 2022; Treu et al. 2023; Ono et al. 2023; Morishita et al. 2024; Ono et al. 2024). Additionally, morphological studies have also been conducted for high- z galaxies selected with other methods, including dusty star-forming galaxies (Gillman et al. 2023; Le Bail et al. 2024; Fujimoto et al. 2023; Hodge et al. 2024; Umehata et al. 2025), strong emission-line selected star-forming

galaxies (Ning et al. 2024; Laishram et al. 2024; Liu et al. 2024; Guo et al. 2024), quiescent galaxies (Ito et al. 2024; Wright et al. 2024; Cutler et al. 2024; Ji et al. 2024; Clausen et al. 2025) and little red dots (Baggen et al. 2024; Rinaldi et al. 2024). Furthermore, several studies have focused on robust samples of galaxies limited to spectroscopically confirmed ones (Calabrò et al. 2024a; Langeroodi & Hjorth 2023) and on more general samples selected using photometric redshifts (Suess et al. 2022; Yao et al. 2023; Baggen et al. 2023; van der Wel et al. 2024; Sun et al. 2024; Ormerod et al. 2024; Ward et al. 2024; Lee et al. 2024; Martorano et al. 2024; Varadaraj et al. 2024; Allen et al. 2024; Jia et al. 2024; Miller et al. 2024; Westcott et al. 2024). Comprehensive morphological classifications have also been performed including those based on visual inspection (Ferreira et al. 2022; Kartaltepe et al. 2023; Ferreira et al. 2023; Conselice et al. 2024; Smethurst et al. 2025; Geron et al. 2025) and approaches utilizing machine learning techniques (Robertson et al. 2023; Vega-Ferrero et al. 2024; Tohill et al. 2024; Huertas-Company et al. 2024; Huertas-Company et al. 2025). In addition, theoretical studies based on cosmological simulations have explored the morphological properties of high- z galaxies and compared their results with observations (e.g., Costantin et al. 2023; Yajima et al. 2023; Shen et al. 2024a; Shen et al. 2024b; Nakazato et al. 2024; LaChance et al. 2024).

Through deep surveys conducted by the Hubble Space Telescope (HST), the morphological properties of high- z galaxies have been investigated (e.g., Ferguson et al. 2004; Bouwens et al. 2004; Bouwens et al. 2006; Hathi et al. 2008; Oesch et al. 2010; Grazian et al. 2012; Ono et al. 2013; Huang et al. 2013; Jiang et al. 2013; Kawamata et al. 2015; Holwerda et al. 2015; Shibuya et al. 2015; Curtis-Lake et al. 2016; Allen et al. 2017; Bowler et al. 2017; Bouwens et al. 2017; Kawamata et al. 2018; Bridge et al. 2019; Holwerda et al. 2020; Bouwens et al. 2022). Nevertheless, many open questions regarding the early stages of galaxy evolution remain unresolved, such as when the first galaxy disks formed in the early universe, which is related to the strength of feedback processes in the early stages of galaxy formation. Using HST WFC3 data, van der Wel et al. (2014) have demonstrated that the slope of the galaxy size–stellar mass relation and the scatter in the galaxy size distribution show no significant evolution for galaxies at $z \sim 0\text{--}3$. Shibuya et al. (2015) have reported that, based on HST extragalactic legacy survey data, the me-

dian Sérsic index for star-forming galaxies at $z \sim 0\text{--}8$ is 1.5, and that their size distributions follow a log-normal form with standard deviations that do not evolve significantly (see also, Kawamata et al. 2015; Kawamata et al. 2018). These findings are consistent with the picture that high- z star-forming galaxies possess disk-like stellar components (e.g., Mo et al. 1998; Shen et al. 2003).

Observational studies using the Atacama Large Millimeter/submillimeter Array (ALMA) have explored the formation of disks at high redshift from the perspective of kinematic properties, utilizing far-infrared emission lines such as [CII]158 μm and [OIII]88 μm . Rizzo et al. (2020) have analyzed the kinematics of the high-resolution [CII] emission of the gravitationally lensed $z = 4.22$ galaxy SPT0418-47 (Weiß et al. 2013), reporting that its rotation curve resembles those of typical nearby spiral galaxies and that the ratio of rotational velocity to velocity dispersion is as high as those obtained for nearby spiral galaxies. Rowland et al. (2024) have reported that, from high-resolution ALMA observations of the [CII] emission from the $z = 7.31$ galaxy REBELS-25, the [CII] flux distribution closely resembles an exponential disk with a Sérsic index of $n = 1.3 \pm 0.2$, and the ratio of rotational velocity to velocity dispersion is consistent with a dynamically cold disk. These findings suggest that galaxies with disk structures already exist at $z \sim 4\text{--}9$ (see also, Smit et al. 2018; Neeleman et al. 2020; Lelli et al. 2021; Fraternali et al. 2021; Neeleman et al. 2021; Tsukui & Iguchi 2021; Yue et al. 2021; Tokuoka et al. 2022; Herrera-Camus et al. 2022; Rizzo et al. 2022; Posses et al. 2023; Parlanti et al. 2023; Roman-Oliveira et al. 2023; Neeleman et al. 2023; Wang et al. 2024).

Early results from JWST have also reported findings on the morphological and kinematic properties of high- z galaxies. Robertson et al. (2023) have derived the Sérsic index for $z = 2\text{--}5$ galaxies classified as disks using convolutional neural networks applied to JWST images, showing that the average Sérsic index is approximately $n = 1$. Ward et al. (2024) have examined the size–stellar mass relation for galaxies at $z = 0.5\text{--}5.5$ using both HST and JWST images and reported that the galaxy size scatter exhibits little to no evolution (see also, Varadaraj et al. 2024; Morishita et al. 2024; Allen et al. 2024; Miller et al. 2024). From a kinematic perspective, de Graaff et al. (2024) have carried out JWST NIRSpec spectroscopy for six galaxies at $z = 5.5\text{--}7.4$ and found that half of them show rotation-dominated velocity structures based on the H α and [OIII] emission lines. In addition, using NIRSpec integral field spectroscopy, Xu et al. (2024) have demonstrated that the CIII] $\lambda\lambda 1907, 1909$ emission in the $z = 10.6$ galaxy GN-

z11 exhibits a velocity gradient consistent with disk rotation (see also, Nelson et al. 2024; Li et al. 2023; Fujimoto et al. 2024). However, most of these results focus on galaxies up to $z \sim 10$, and a statistical investigation into the presence of disks in galaxies at even higher redshifts is worth pursuing.

In this paper, we investigate the morphological properties of $z \sim 10\text{--}16$ galaxies using deep JWST NIRCам images obtained from the Cosmic Evolution Early Release Science (CEERS; Finkelstein et al. 2025; see also, Finkelstein et al. 2022; Finkelstein et al. 2023b; Bagley et al. 2023) survey and the JWST Advanced Deep Extragalactic Survey (JADES; Eisenstein et al. 2023a; Bunker et al. 2024; Rieke et al. 2023c; Eisenstein et al. 2023b; D'Eugenio et al. 2024; Hainline et al. 2024). Our analysis primarily relies on the high- z galaxy catalogs constructed for the CEERS fields by Finkelstein et al. (2024) and for the JADES fields by Hainline et al. (2024). This paper is structured as follows. Section 2 describes the JADES and CEERS NIRCам data and provides an overview of $z \sim 10\text{--}16$ galaxies analyzed in this study. Section 3 details the two-dimensional surface brightness profile fitting method that we employ, along with an investigation of its systematic and statistical uncertainties based on Monte Carlo simulations. In Section 4, we present the results of profile fittings such as sizes and total magnitudes for $z \sim 10\text{--}16$ galaxies in the rest-frame UV continuum and derive their size and axis ratio distributions. In addition, we explore the relation between galaxy UV size and luminosity, as well as the redshift evolution of galaxy sizes. In Section 5, we estimate the stellar-to-halo size ratios of $z \sim 10\text{--}16$ galaxies and discuss whether the morphological properties of $z \sim 10\text{--}16$ galaxies are consistent with the disk formation scenario. Furthermore, we compare our observational results with cosmological simulation results to discuss the origin of the diversity in galaxy sizes ranging from compact to extended ones. Section 6 provides a summary of this study.

Throughout this paper, we use magnitudes in the AB system (Oke & Gunn 1983) and assume a flat universe (e.g., Planck Collaboration et al. 2020) with $\Omega_m = 0.3$, $\Omega_\Lambda = 0.7$, and $H_0 = 70 \text{ km s}^{-1} \text{ Mpc}^{-1}$. In this cosmological model, an angular dimension of $1''.0$ corresponds to a physical dimension of 4.159 kpc at $z = 10$, 3.659 kpc at $z = 12$, and 3.268 kpc at $z = 14$ (Equation 18 of Hogg 1999).¹ These values are provided as il-

lustrative examples; in our analysis, we calculate the physical dimensions using the exact redshifts of individual galaxies, adopting spectroscopic redshifts when available and photometric redshifts otherwise. Following previous studies, we describe the UV luminosities of galaxies in units of the characteristic luminosity of $z \sim 3$ galaxies, $L_{z=3}^*$, which corresponds to $M_{\text{UV}} = -21.0 \text{ mag}$ (Steidel et al. 1999). In this case, $0.048L_{z=3}^*$, $0.12L_{z=3}^*$, and $0.3L_{z=3}^*$ correspond to $M_{\text{UV}} = -17.7$, -18.7 , and -19.7 mag , respectively.

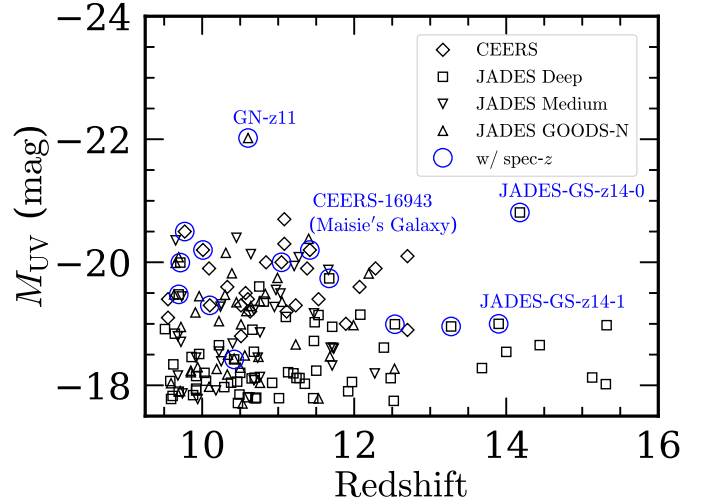


Figure 1. M_{UV} vs. redshift for the $z \sim 10\text{--}16$ galaxies analyzed in this study. The black diamonds represent CEERS galaxies (Finkelstein et al. 2024), the black squares correspond to JADES Deep, the black downward triangles indicate JADES Medium, and the black upward triangles denote JADES GOODS-N galaxies (Hainline et al. 2024; Carniani et al. 2024a; Schouws et al. 2024; Carniani et al. 2024b). Objects outlined with large blue circles are spectroscopically confirmed. The names of well-studied galaxies are labeled in blue near their respective data points.

2. DATA AND SAMPLES

We measure the sizes of $z \sim 10\text{--}16$ galaxies found in the CEERS and JADES programs. For CEERS, we use the high- z galaxy sample from Finkelstein et al. (2024), and for JADES, we use the sample from Hainline et al. (2024). From these high- z galaxy samples, which are primarily selected based on photometric redshifts, we include those with $z > 9.5$. The GOODS-S field in JADES is divided into deeper regions (JADES Deep and 1210 Parallel) and moderately deep regions (JADES Medium). For simplicity, we refer to the former as

¹ The cosmic ages at these redshifts are 464 Myr, 361 Myr, and 291 Myr, respectively.

Table 1. Numbers of Objects Analyzed in This Study

	CEERS	JADES Deep	JADES Medium	JADES GOODS-N
Number of galaxies at $z = 9.5\text{--}13$	26 (5)	56 (5)	34 (0)	41 (1)
Number of galaxies at $z = 9.5\text{--}13$ with $S/N > 10$ in F200W	7 (4)	10 (4)	8 (0)	7 (1)
Number of galaxies at $z = 13\text{--}16$	3 (0)	9 (3)	0 (0)	0 (0)
Number of galaxies at $z = 13\text{--}16$ with $S/N > 10$ in F277W	0 (0)	3 (3)	0 (0)	0 (0)
Total	29 (5)	65 (8)	34 (0)	41 (1)

NOTE— The numbers in parentheses indicate the number of objects with spectroscopic redshifts. The total number of $z = 9.5\text{--}16$ galaxies analyzed in this study is $29+65+34+41 = 169$, and the number of $z = 9.5\text{--}16$ galaxies with $S/N > 10$ is $7+10+8+7+3 = 35$.

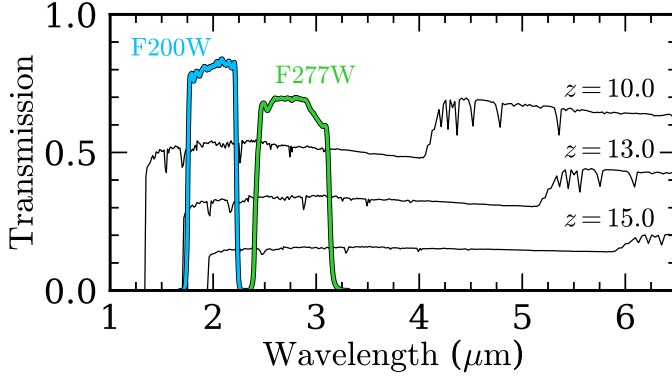


Figure 2. Transmission curves of the NIRCam broadband filters F200W (cyan) and F277W (green), along with the spectra of a star-forming galaxy at $z = 10$, $z = 13$, and $z = 15$ based on the Bruzual & Charlot (2003) library (black).

JADES Deep and the latter as JADES Medium. For GOODS-N in JADES, we basically focus on the SE region, which has a depth almost comparable to JADES Medium. GN-z11 is an exception among the objects in the NW region of JADES GOODS-N, because it is a spectroscopically confirmed luminous high- z source that has been studied in detail (e.g., Oesch et al. 2016; Tacchella et al. 2023; Bunker et al. 2023; Senchyna et al. 2024; Maiolino et al. 2024; Xu et al. 2024; Nakane et al. 2024; Álvarez-Márquez et al. 2024). We thus include it in our sample as a special case. Additionally, for JADES, we incorporate two spectroscopically confirmed galaxies at $z = 14.18$ and $z = 13.90$, namely JADES-GS-z14-0 and JADES-GS-z14-1 (Carniani et al. 2024a; Schouws et al. 2024; Carniani et al. 2024b). On the other hand, JADES-GS-53.12692-27.79102, included in the Hainline et al. (2024) catalog, has been identified as a lower- z transient interloper by the JADES Transient Survey (DeCoursey et al. 2024), and is therefore excluded from this study. The total number of $z \sim 10\text{--}16$ galaxies analyzed in this study

Table 2. Numbers of Stacked Objects in Each Field and Luminosity Bin

ID	luminosity range	N
$L/L_{z=3}^*$		
$z = 9.5\text{--}13$		
z11-stack-CEERS	0.3–1	5
z11-stack-CEERS-f	0.12–0.3	14
z11-stack-JADES-f	0.12–0.3	5
z11-stack-JADES-f2	0.048–0.12	41
z11-stack-JADESM-f	0.12–0.3	8
z11-stack-JADESM-f2	0.048–0.12	17
z11-stack-JADESGN	0.3–1	3
z11-stack-JADESGN-f	0.12–0.3	12
z11-stack-JADESGN-f2	0.048–0.12	19
$z = 13\text{--}16$		
z15-stack-JADES-f	0.048–0.3	6

NOTE— The third part of the ID from the left, separated by hyphens, indicates the field where the stacked objects are located. “CEERS” corresponds to the CEERS field, “JADES” to the JADES Deep field, “JADESM” to the JADES Medium field, and “JADESGN” to the JADES GOODS-N field.

is 169, of which 14 are spectroscopically confirmed. The number of $z \sim 10\text{--}16$ galaxies in each region is summarized in Table 1. Figure 1 illustrates the distribution of their redshifts and rest-frame UV magnitudes, M_{UV} . More detailed lists are provided in Appendix A. Among these, two objects in CEERS and one object in JADES are included in the catalog of little red dots compiled by Kocevski et al. (2024); we mark them with a dagger symbol in Table A.1 and Table A.2.

Table 3. Limiting Magnitudes and PSF FWHMs of the JWST NIRCам Images for Size Analysis

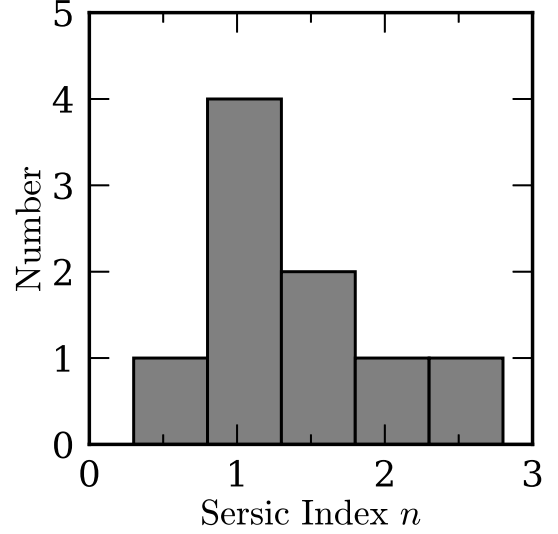
Field	10 σ Depth / PSF FWHM	
	F200W	F277W
CEERS1	28.5 / 0''.0716	— / —
CEERS2	28.9 / 0''.0792	— / —
CEERS3	28.6 / 0''.0711	— / —
CEERS4	28.5 / 0''.0711	— / —
CEERS5	28.5 / 0''.0725	— / —
CEERS6	28.5 / 0''.0744	— / —
CEERS7	28.5 / 0''.0729	— / —
CEERS8	28.5 / 0''.0720	— / —
CEERS9	28.5 / 0''.0762	— / —
CEERS10	28.5 / 0''.0764	— / —
JADES Deep	29.3 / 0''.0771	29.8 / 0''.1215
JADES Medium	28.8 / 0''.0771	29.1 / 0''.1215
JADES GOODS-N	29.0 / 0''.0789	29.2 / 0''.1161

NOTE— Limiting magnitudes are measured with randomly distributed 0''.2 diameter circular apertures (Harikane et al. 2023; Y. Harikane et al. in preparation; Hainline et al. 2024; see also, Finkelstein et al. 2024).

To investigate the sizes of $z \sim 10\text{--}16$ galaxies in their rest-frame UV continuum, we use JWST NIRCам F200W images for $z = 9.5\text{--}13$ galaxies and F277W images for $z = 13\text{--}16$ galaxies. Figure 2 shows the transmission curves of these filters plotted together with example SEDs of high- z star-forming galaxies. For CEERS, we use NIRCам images reduced by Harikane et al. (2023) and Y. Harikane et al. in preparation, with a pixel scale of 0''.015 pix^{−1}. For JADES, we utilize the official JADES images available on MAST,² which have a pixel scale of 0''.03 pix^{−1}.³ The 10 σ limiting magnitudes of these images are summarized in Table 3. Following the previous studies, we select sources with a signal-to-noise ratio (S/N) greater than 10 for individual analyses, based on apparent magnitudes measured within 0''.2 diameter circular apertures. The numbers of sources meeting this S/N threshold is listed in Table 1.

² <https://archive.stsci.edu/hlsp/jades>

³ Initially, we considered using the images from the DAWN JWST Archive, which have a finer pixel scale of 0''.02 pix^{−1}. However, the latest versions available at that time, i.e., the v7.0 to v7.2 images of JADES GOODS-S, were unexpectedly cropped in the southwest direction; we thus decided not to use them in this paper.

**Figure 3.** Histogram of the best-fit Sérsic index values for spectroscopically confirmed galaxies in our sample with $S/N > 10$. The mean value is $n = 1.3 \pm 0.6$.

To extend our size measurements to fainter objects, we divide the sample in each field basically into three luminosity bins, $L/L_{z=3}^* = 0.3\text{--}1$, $0.12\text{--}0.3$, and $0.048\text{--}0.12$, based on their M_{UV} magnitudes reported in the original catalogs (Finkelstein et al. 2024; Hainline et al. 2024), and make median stacked images separately for these luminosity bins. The number of objects stacked for each luminosity bin in each field is summarized in Table 2. For $z = 9.5\text{--}13$, since there are no objects in the $L/L_{z=3}^* = 0.3\text{--}1$ luminosity bin in JADES Deep, and only one object in this bin in JADES Medium, stacked images are not created for these cases. Additionally, no objects in CEERS fall into the $L/L_{z=3}^* < 0.12$ luminosity bins. For $z = 13\text{--}16$, no stacked images are created for CEERS due to the small number of objects. In JADES Deep, due to the limited number of objects, we combine the objects in the $L/L_{z=3}^* = 0.048\text{--}0.12$ and $L/L_{z=3}^* = 0.12\text{--}0.3$ luminosity bins into a single stacked image. We confirm that the S/Ns of the aperture magnitudes of these stacked objects are $\gtrsim 10$.

Measurements of galaxy sizes require accounting for image smearing characterized with the point spread function (PSF). To correct for this effect, we use empirical PSFs constructed by stacking bright point sources from the NIRCам images. In each field, we select four to eleven unsaturated bright point sources with magnitudes of $\sim 22\text{--}24$ mag. More specifically, we run SExtractor (Bertin & Arnouts 1996) on each image to detect sources and select bright unresolved objects that lie in the stellar locus in the half-light radius vs. magnitude plane as point sources (e.g., Figure 2 of Holwerda et al.

2024). Among these selected point sources, we further choose those that are isolated from nearby objects and not located around the edges of the image. We then stack these sources to construct the empirical PSFs. In the CEERS field, Holwerda et al. (2024) have similarly identified unresolved sources in the stellar locus and classified brown dwarf types using the k -means nearest neighbor algorithm. We confirm that the vast majority of our selected point sources in the CEERS field (55 out of 57) match those listed in the catalog of Holwerda et al. (2024). The FWHM values of the resulting PSFs are summarized in Table 3.

3. SURFACE BRIGHTNESS PROFILE FITTING

To measure the half-light radii of the $z \sim 10$ –16 galaxies in the CEERS and JADES fields summarized in Section 2, we fit their two-dimensional surface brightness profiles with a Sérsic profile (Sérsic 1968). The Sérsic profile is defined as

$$\Sigma(r) = \Sigma_e \exp \left(-b_n \left[\left(\frac{r}{r_e} \right)^{1/n} - 1 \right] \right), \quad (1)$$

where Σ_e is the surface brightness at the half-light radius r_e , n is the Sérsic index, and b_n is a constant determined such that the flux within r_e equals half of the total flux. We perform surface brightness profile fitting using GALFIT version 3 (Peng et al. 2002; Peng et al. 2010), a software package that optimizes the fit by convolving the surface brightness distribution with the PSF profile and minimizing χ^2 using the Levenberg-Marquardt algorithm. The output parameters from GALFIT include the central coordinates, total magnitude, semi-major axis radius a , Sérsic index n , axis ratio b/a , and position angle. For each object, we calculate the circularized half-light radius as $r_e = a\sqrt{b/a}$, which is commonly used as the galaxy size in previous studies (e.g., Mosleh et al. 2012; Newman et al. 2012; Ono et al. 2013; Shibuya et al. 2015; Kawamata et al. 2018). The initial parameters for GALFIT are derived from running SExtractor on the images. All the parameters except the Sérsic index are treated as free parameters during the fitting process. To weight individual pixels during the profile fitting, we use noise images that are calculated as the inverse square root of the weight maps. Additionally, segmentation images generated by SExtractor are used to mask nearby objects during profile fitting to focus on the target objects of interest.

We fix the Sérsic index at $n = 1.5$. This value corresponds to the median Sérsic index determined for star-forming galaxies with UV luminosities comparable to our objects reported in the literature (Shibuya et al. 2015). Indeed, when we allow the Sérsic index to vary

as a free parameter in the GALFIT profile fitting for 12 spectroscopically confirmed galaxies with $S/N > 10$ in our sample,⁴ the fitting converges successfully for 9 galaxies and the resulting Sérsic index values yield a mean value of $n = 1.3 \pm 0.6$ (see also, Martorano et al. 2023; Sun et al. 2024; Martorano et al. 2025).⁵ Figure 3 shows the histogram of the obtained Sérsic index values. However, as noted in our previous work, the currently available data are not sufficient to obtain reliable measurements on the Sérsic index and the other morphological parameters simultaneously for high- z galaxies (see Section 3.1 of Ono et al. 2024). Therefore, following the approach of previous high- z galaxy size studies, we perform surface brightness profile fitting with a fixed Sérsic index. Our choice to fix the Sérsic index at $n = 1.5$ represents a pragmatic approach. We acknowledge that while Sérsic index values for star-forming galaxies are generally found around $n = 1$ (corresponding to an exponential disk) with a somewhat broad distribution (e.g., Martorano et al. 2023; Sun et al. 2024; Martorano et al. 2025), the primary goal of this study is to robustly constrain r_e and total magnitude values for our sample. Fixing the Sérsic index helps to mitigate degeneracies between fitting parameters, thereby enhancing the reliability of the derived values, particularly for faint sources where the S/N is limited.

As in previous studies (Ono et al. 2013; Shibuya et al. 2015), we perform Monte Carlo simulations to quantify both statistical and systematic uncertainties in the GALFIT profile fitting. For CEERS, we adopt the results of the Monte Carlo simulations conducted in Ono et al. (2023). For JADES, we run Monte Carlo simulations for JADES Deep and JADES GOODS-N. For JADES Medium, we shift the results of JADES Deep according to the difference in the limiting magnitudes.

First, we generate galaxy images using GALFIT, fixing the Sérsic index at $n = 1.5$. The half-light radius is randomly selected from a range of 0.3 pix to 10.0 pix, while the axis ratio is randomly chosen from values between 0.2 and 1.0, and the total magnitude is chosen between 25.5 mag and 31.0 mag. These simulated galaxy images are convolved with the PSF images created in Section 2 and inserted into blank regions of the actual

⁴ Our analysis of the varying Sérsic index is limited to spectroscopically confirmed galaxies to ensure high reliability and minimize contamination from, e.g., low- z interlopers. While these galaxies tend to be brighter within our overall sample, it would be important to note that reliably determining the Sérsic index requires a sufficiently high S/N , meaning that such measurements are inherently biased toward brighter objects, even when galaxies without spectroscopic confirmation are included.

⁵ The median value is also $n = 1.3$.

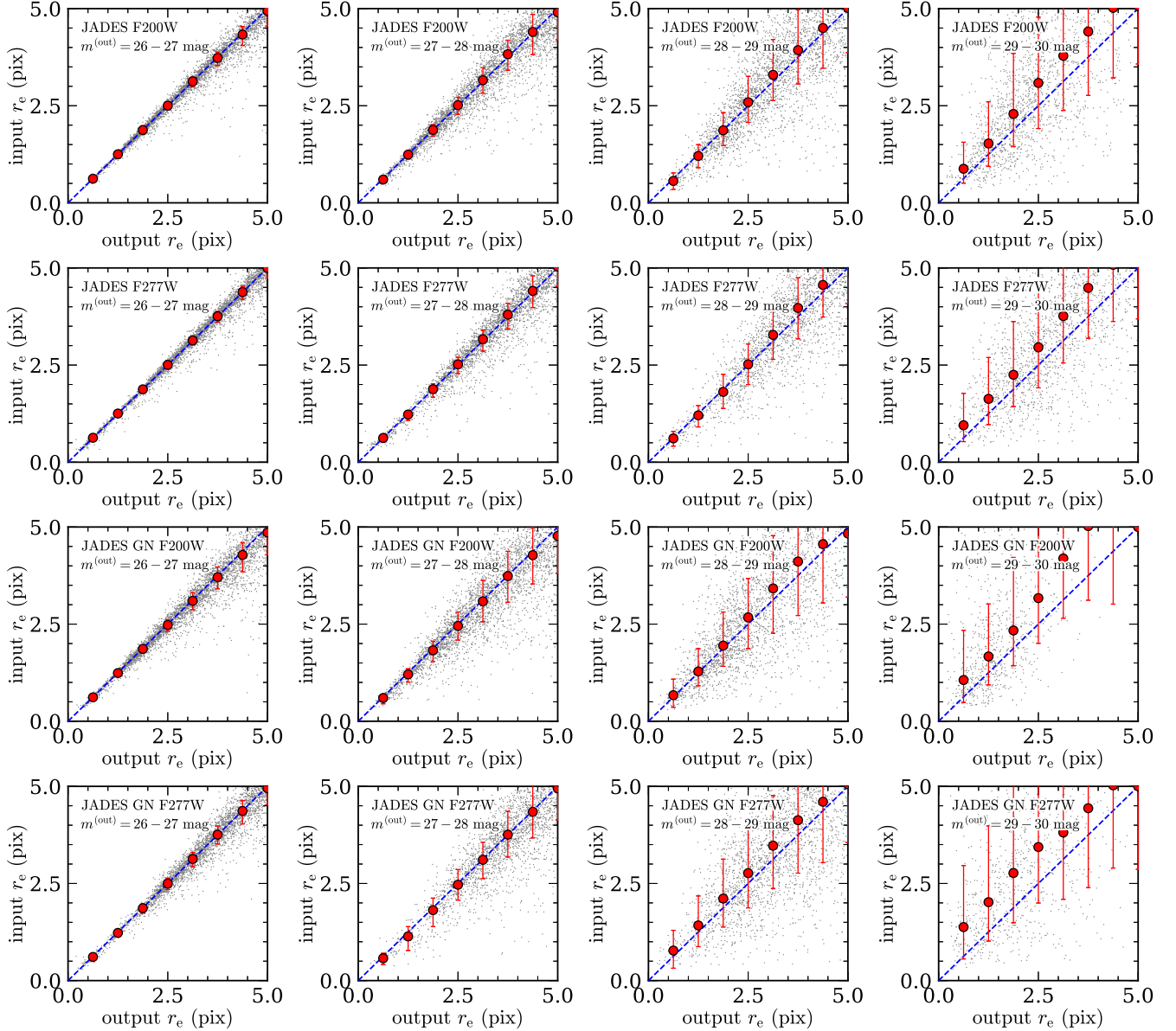


Figure 4. Input circularized radius vs. output circularized radius for a range of output total magnitude $m^{(\text{out})} = 26\text{--}27$ mag, $27\text{--}28$ mag, $28\text{--}29$ mag, and $29\text{--}30$ mag from left to right, based on our GALFIT Monte Carlo simulations. From top to bottom, the results for the JADES Deep field in F200W and F277W, and the JADES GOODS-N field in F200W and F277W are presented. The red filled circles and the red error bars correspond to the median values of the difference between the input and output circularized radii and the 68 percentile ranges, respectively. The gray dots are the results for individual simulated objects. The blue dashed line represents the relation that the input and output circularized radius are equal. The measured sizes are generally consistent with the input sizes on average, even for galaxies with sizes smaller than the PSF FWHMs, i.e., about 2.5 and 4.0 pixels in F200W and F277W, respectively.

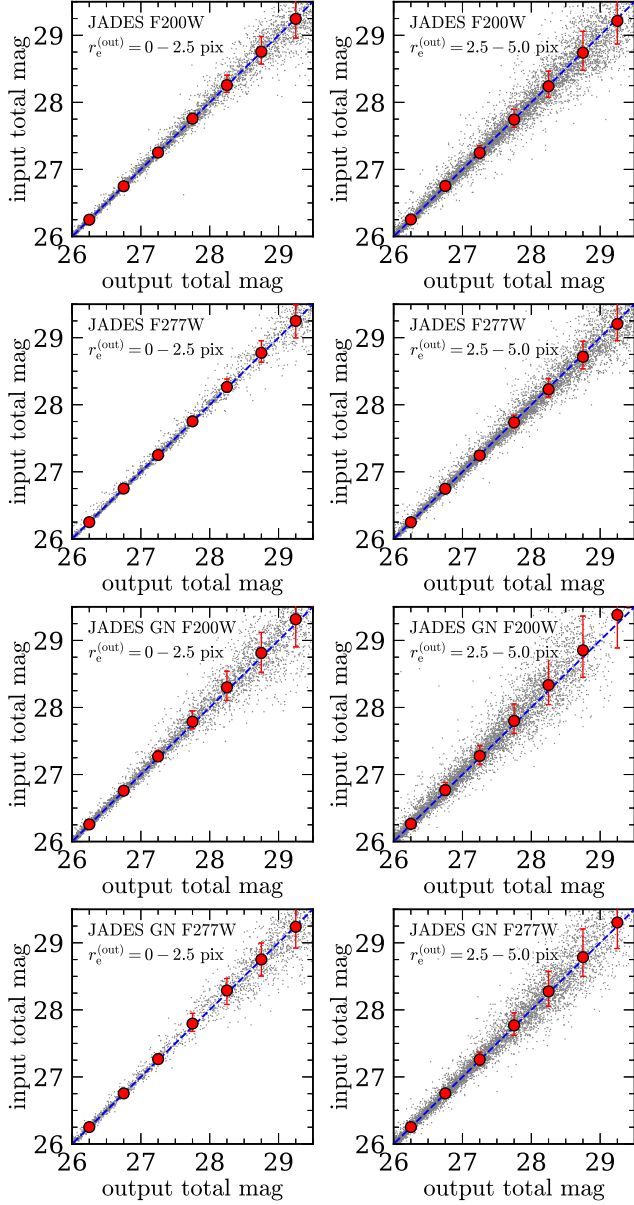


Figure 5. Input total magnitude vs. output total magnitude for a range of output half-light radii $r_e^{(\text{out})} = 0\text{--}2.5$ pixels (left) and $2.5\text{--}5.0$ pixels (right) based on our GALFIT Monte Carlo simulations. From top to bottom, the results for the JADES Deep field in F200W and F277W, and the JADES GOODS-N field in F200W and F277W are presented. The red filled circles and the red error bars correspond to the median values of the difference between the input and output magnitudes and the 68 percentile ranges, respectively. The gray dots are the results for individual simulated objects. The blue dashed line represents the relation that the input and output magnitudes are equal.

NIRCam images. We then perform surface brightness profile fitting with GALFIT in the same way as for real

high- z galaxies to measure the sizes and total magnitudes.

The comparisons between the measured sizes and the input sizes are shown in Figure 4, while the comparisons between the measured total magnitudes and the input total magnitudes are presented in Figure 5. Figure 4 demonstrates that even when the galaxy sizes are smaller than the PSF FWHMs (about 2.5 pixels in F200W and 4.0 pixels in F277W), the measured sizes are, on average, reasonably consistent with the input sizes. In agreement with the results of Ono et al. (2023), our Monte Carlo simulations confirm that the half-light radius is systematically underestimated for faint objects. For instance, examining the results for the F200W image in the JADES Deep field, the median difference between input and output sizes is nearly zero for the brightest magnitude range of 26–27 mag, whereas it is approximately 15–25% for the faintest range of 29–30 mag. Furthermore, statistical uncertainties increase for fainter and larger objects. For example, for the F200W image in the JADES Deep field, the statistical uncertainties are several percent in the brightest magnitude range, but increase to about 40–100% in the faintest magnitude range. We account for these systematic and statistical uncertainties in the measurements of real high- z galaxies. Briefly, for each high- z galaxy in our sample, we correct the measured size by the median difference between the input and output sizes in the magnitude bin corresponding to its output total magnitude. Additionally, we take the 68th percentile difference between the input and output sizes in each bin as the statistical uncertainty. A similar approach is applied to the total magnitudes (see Section 3 of Ono et al. 2023 for details).

In addition to the circularized half-light radius and total magnitude, we also compare the input and output values for the axis ratio b/a . As shown in Figure 6, the measured b/a values are, on average, consistent with the input b/a across all input values. Similar to the sizes and total magnitudes, the statistical uncertainties for the axis ratio increase with decreasing brightness. For example, considering the results for the F200W image in the JADES Deep field, the statistical uncertainties are about several percent in the brightest magnitude range, but increase to about 10–50% for the 28–29 mag range. For the axis ratio, as with sizes and total magnitudes, we account for these systematic and statistical uncertainties in the measurements of real high- z galaxies.

4. RESULTS

4.1. Surface Brightness Profile Fitting Results

Table 4. Surface Brightness Profile Fitting Results

ID	z_{photo}	z_{spec}	S/N	m_{UV}	M_{UV}	r_e	b/a
(1)	(2)	(3)	(4)	(mag)	(mag)	(kpc)	(8)
CEERS							
CEERS-11384	11.53	$11.043^{+0.003}_{-0.003}$	13	$27.53^{+0.20}_{-0.21}$	$-20.09^{+0.20}_{-0.21}$	$0.336^{+0.079}_{-0.059}$	$0.35^{+0.14}_{-0.07}$
CEERS-16943 ^{†1}	11.08	$11.416^{+0.005}_{-0.005}$	16	$27.16^{+0.13}_{-0.13}$	$-20.51^{+0.13}_{-0.13}$	$0.453^{+0.120}_{-0.082}$	$0.67^{+0.18}_{-0.16}$
CEERS-35590	10.15	$10.01^{+0.14}_{-0.19}$	15	$27.61^{+0.12}_{-0.14}$	$-19.87^{+0.12}_{-0.14}$	$0.167^{+0.056}_{-0.049}$	$0.71^{+0.18}_{-0.16}$
CEERS-54306	11.23	—	11	$27.93^{+0.21}_{-0.21}$	$-19.72^{+0.21}_{-0.21}$	$0.089^{+0.052}_{-0.045}$	$0.75^{+0.19}_{-0.16}$
CEERS-85546	11.08	—	11	$27.98^{+0.21}_{-0.21}$	$-19.65^{+0.21}_{-0.21}$	$0.106^{+0.129}_{-0.068}$	$0.76^{+0.19}_{-0.30}$
CEERS-98518 ^{†2}	10.09	—	19	$27.46^{+0.12}_{-0.14}$	$-20.03^{+0.12}_{-0.14}$	$0.121^{+0.056}_{-0.048}$	$0.64^{+0.18}_{-0.16}$
CEERS-99715	9.76	$9.77^{+0.37}_{-0.29}$	13	$28.15^{+0.27}_{-0.29}$	$-19.30^{+0.27}_{-0.29}$	$0.159^{+0.141}_{-0.074}$	$0.57^{+0.27}_{-0.16}$
CEERS-99715b	9.76	$9.77^{+0.37}_{-0.29}$	13	$27.47^{+0.12}_{-0.14}$	$-19.98^{+0.12}_{-0.14}$	$0.340^{+0.086}_{-0.064}$	$0.78^{+0.18}_{-0.21}$
JADES Deep							
JADES-GS-z14-0	—	$14.1793^{+0.0007}_{-0.0007}$	46	$26.91^{+0.02}_{-0.02}$	$-21.08^{+0.02}_{-0.02}$	$0.288^{+0.005}_{-0.007}$	$0.48^{+0.35}_{-0.18}$
JADES-GS-z14-1	—	$13.9^{+0.17}_{-0.17}$	10	$28.85^{+0.18}_{-0.14}$	$-19.11^{+0.18}_{-0.14}$	$0.158^{+0.017}_{-0.020}$	$0.20^{+0.02}_{-0.02}$
JADES-GS-53.14988-27.7765 ^{†3}	13.41	13.274	10	$29.27^{+0.18}_{-0.14}$	$-18.62^{+0.18}_{-0.14}$	$0.061^{+0.084}_{-0.043}$	$0.29^{+0.35}_{-0.18}$
JADES-GS-53.16476-27.77463 ^{†4}	12.31	11.671	18	$28.20^{+0.08}_{-0.06}$	$-19.50^{+0.08}_{-0.06}$	$0.108^{+0.023}_{-0.024}$	$0.56^{+0.19}_{-0.14}$
JADES-GS-53.16635-27.82156 ^{†5}	12.46	12.535	10	$28.79^{+0.23}_{-0.18}$	$-19.01^{+0.23}_{-0.18}$	$0.148^{+0.022}_{-0.023}$	$0.76^{+0.16}_{-0.18}$
JADES-GS-53.16736-27.80751	9.54	9.691	23	$28.10^{+0.08}_{-0.06}$	$-19.33^{+0.08}_{-0.06}$	$0.105^{+0.026}_{-0.028}$	$0.75^{+0.16}_{-0.18}$
JADES-GS-53.17551-27.78064	9.66	9.712	29	$27.78^{+0.08}_{-0.06}$	$-19.66^{+0.08}_{-0.06}$	$0.122^{+0.009}_{-0.011}$	$0.65^{+0.07}_{-0.06}$
JADES-GS-53.05177-27.88727	9.51	—	11	$28.79^{+0.23}_{-0.18}$	$-18.61^{+0.23}_{-0.18}$	$0.138^{+0.027}_{-0.028}$	$0.81^{+0.16}_{-0.18}$
JADES-GS-53.16594-27.83424	10.75	—	25	$27.63^{+0.06}_{-0.04}$	$-19.96^{+0.06}_{-0.04}$	$0.194^{+0.009}_{-0.010}$	$0.36^{+0.04}_{-0.04}$
JADES-GS-53.19051-27.74982	12.08	—	17	$28.47^{+0.15}_{-0.11}$	$-19.29^{+0.15}_{-0.11}$	$0.023^{+0.023}_{-0.023}$	$0.20^{+0.16}_{-0.08}$
JADES Medium							
JADES-GS-53.05511-27.84555	9.65	—	15	$27.88^{+0.15}_{-0.11}$	$-19.54^{+0.15}_{-0.11}$	$0.150^{+0.027}_{-0.028}$	$0.53^{+0.19}_{-0.14}$
JADES-GS-53.07076-27.86544	11.03	—	11	$28.32^{+0.23}_{-0.18}$	$-19.31^{+0.23}_{-0.18}$	$0.077^{+0.024}_{-0.025}$	$0.49^{+0.16}_{-0.11}$
JADES-GS-53.10798-27.8776	10.97	—	15	$27.97^{+0.15}_{-0.11}$	$-19.65^{+0.15}_{-0.11}$	$0.077^{+0.024}_{-0.025}$	$0.57^{+0.19}_{-0.14}$
JADES-GS-53.1216-27.90813	11.66	—	13	$27.92^{+0.15}_{-0.11}$	$-19.78^{+0.15}_{-0.11}$	$0.153^{+0.023}_{-0.024}$	$0.36^{+0.16}_{-0.08}$
JADES-GS-53.13918-27.84849	10.45	—	12	$27.87^{+0.15}_{-0.11}$	$-19.68^{+0.15}_{-0.11}$	$0.192^{+0.025}_{-0.026}$	$0.36^{+0.16}_{-0.08}$
JADES-GS-53.07597-27.80654	11.27	—	11	$28.55^{+0.23}_{-0.18}$	$-19.10^{+0.23}_{-0.18}$	$0.118^{+0.079}_{-0.043}$	$0.78^{+0.25}_{-0.29}$
JADES-GS-53.07597-27.80654b	11.27	—	11	$28.32^{+0.23}_{-0.18}$	$-19.34^{+0.23}_{-0.18}$	$0.132^{+0.024}_{-0.025}$	$0.43^{+0.16}_{-0.11}$
JADES GOODS-N							
JADES-GN-189.10604+62.24204 ^{†6}	11.00	10.603	102	$25.97^{+0.03}_{-0.03}$	$-21.59^{+0.03}_{-0.03}$	$0.055^{+0.005}_{-0.006}$	$0.83^{+0.06}_{-0.06}$
JADES-GN-189.21769+62.19949	10.31	—	22	$27.54^{+0.09}_{-0.06}$	$-19.98^{+0.09}_{-0.06}$	$0.122^{+0.010}_{-0.018}$	$0.44^{+0.12}_{-0.09}$
JADES-GN-189.25354+62.19416	9.63	—	14	$28.07^{+0.16}_{-0.11}$	$-19.35^{+0.16}_{-0.11}$	$0.137^{+0.053}_{-0.040}$	$0.46^{+0.32}_{-0.13}$
JADES-GN-189.26202+62.20109	9.69	—	12	$27.52^{+0.09}_{-0.06}$	$-19.91^{+0.09}_{-0.06}$	$0.369^{+0.030}_{-0.037}$	$0.31^{+0.08}_{-0.06}$
JADES-GN-189.26804+62.15158	10.99	—	12	$28.19^{+0.16}_{-0.11}$	$-19.43^{+0.16}_{-0.11}$	$0.118^{+0.048}_{-0.036}$	$0.40^{+0.32}_{-0.13}$
JADES-GN-189.28903+62.22905	10.39	—	15	$27.96^{+0.16}_{-0.11}$	$-19.58^{+0.16}_{-0.11}$	$0.137^{+0.010}_{-0.018}$	$0.69^{+0.17}_{-0.12}$
JADES-GN-189.30296+62.21075	10.30	—	15	$28.14^{+0.16}_{-0.11}$	$-19.38^{+0.16}_{-0.11}$	$0.029^{+0.051}_{-0.029}$	$0.25^{+0.32}_{-0.13}$

NOTE—The systematic effects and statistical uncertainties in these obtained size and total magnitude measurements are considered based on our MC simulation results. (1) Object ID. (2) Photometric redshift (Finkelstein et al. 2024; Hainline et al. 2024). (3) Spectroscopic redshift (Finkelstein et al. 2024; Hainline et al. 2024; Carniani et al. 2024a; Schouws et al. 2024; Carniani et al. 2024b). (4) S/N values based on apparent magnitudes measured within $0''.2$ diameter circular apertures. For $z < 13$, F200W images are used, and for $z > 13$, F277W images are used. (5) Total apparent UV magnitude measured by GALFIT. (6) Total absolute UV magnitude, calculated using z_{spec} if available, otherwise using z_{photo} . (7) Circularized half-light radius $r_e = a\sqrt{b/a}$. (8) Axis ratio.

^{†1} Maisie’s Galaxy (Finkelstein et al. 2022).

^{†2} CEERS 23931 selected as a little red dot (Kocevski et al. 2024).

^{†3} GS-z13-0 (Curtis-Lake et al. 2023).

^{†4} UDFj-39546284 (Bouwens et al. 2011); UDF12-3954-6284 (Ellis et al. 2013); GS-z11-0 (Curtis-Lake et al. 2023).

^{†5} GS-z12-0 (Curtis-Lake et al. 2023).

^{†6} GN-z11 (Oesch et al. 2016).

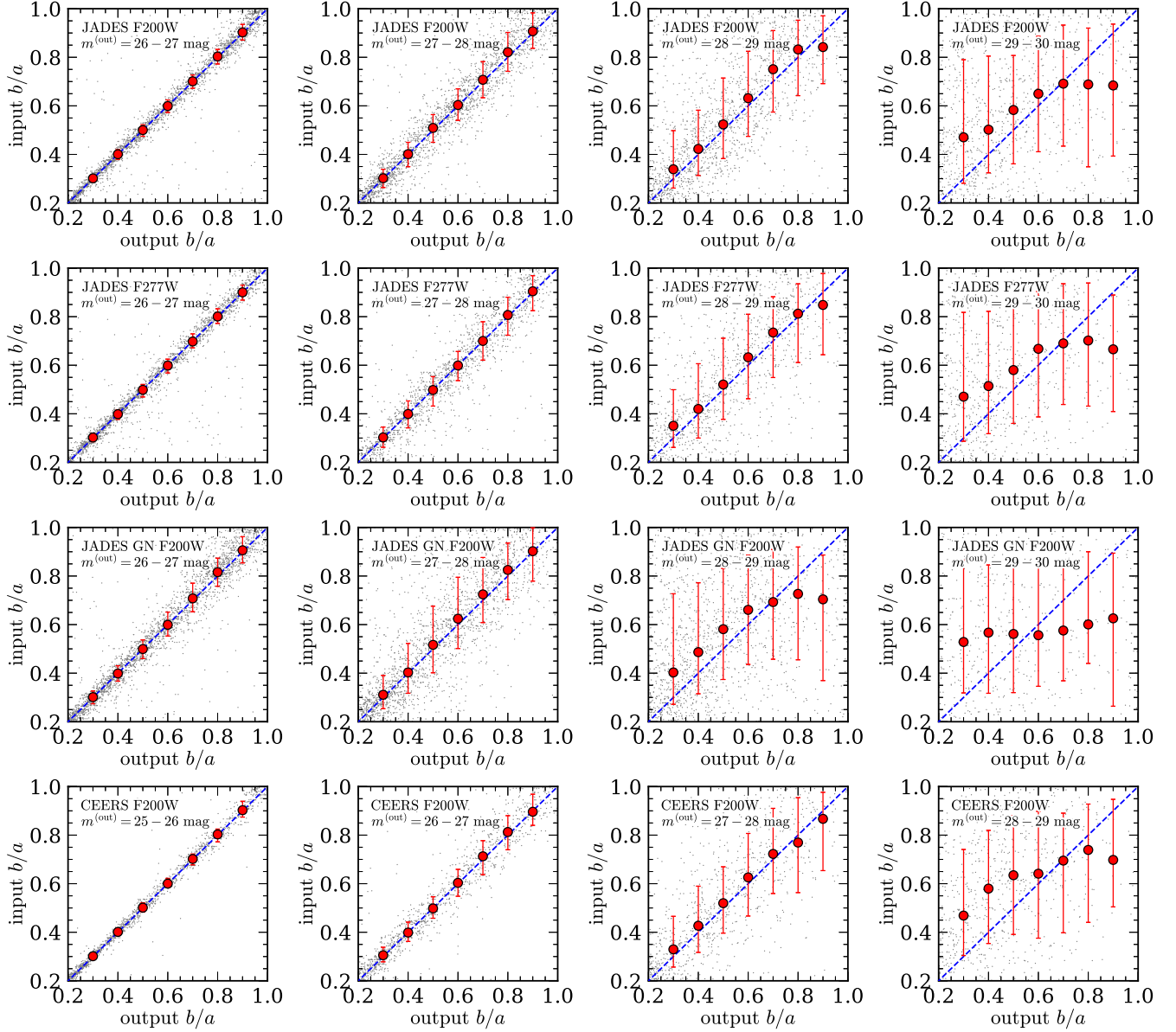


Figure 6. Input axis ratio vs. output axis ratio based on our GALFIT Monte Carlo simulations. From top to bottom, the results for the JADES Deep field in F200W and F277W, the JADES GOODS-N field in F200W and the CEERS field in F200W are presented. From left to right, the results for fainter magnitude ranges are shown. The red filled circles and associated error bars are the median difference between the input and output axis ratios and their 68 percentile ranges, respectively. The gray dots depict the results for individual simulated objects. The blue dashed line marks the one-to-one correspondence between input and output axis ratios. On average, the output axis ratios demonstrate general agreement with their input values.

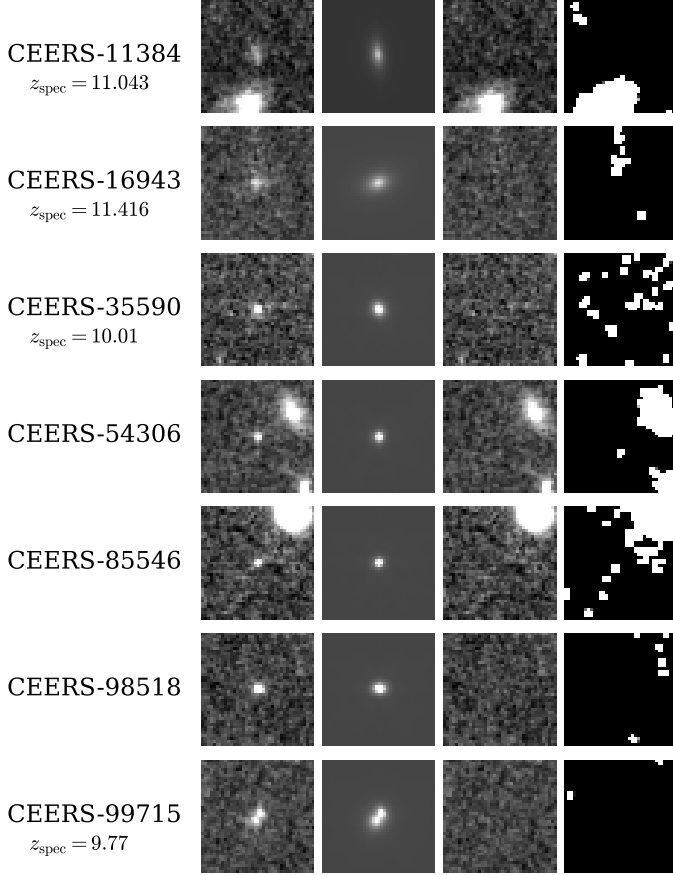


Figure 7. Sérsic profile fitting results for high- z galaxies found in the CEERS field. Spectroscopically confirmed galaxies are labeled with their z_{spec} values. From left to right, the $1''.5 \times 1''.5$ cutouts of the original image, the best-fit Sérsic model profile images, the residual images that are made by subtracting the best-fit images from the original ones, and the segmentation maps used for masking all the neighboring objects during the profile fitting are presented.

We perform surface brightness profile fitting using GALFIT for the $z \sim 10\text{--}16$ galaxies in the CEERS and JADES fields summarized in Section 2. For galaxies with an aperture magnitude $S/N > 10$, we fit their profiles individually, while for fainter objects, we perform fitting on the stacked images to determine their average properties. Systematic uncertainties are corrected based on the results of the Monte Carlo simulations described in Section 3. Note that among the objects with $S/N > 10$, the individual fitting processes do not converge successfully for five galaxies in the JADES sam-

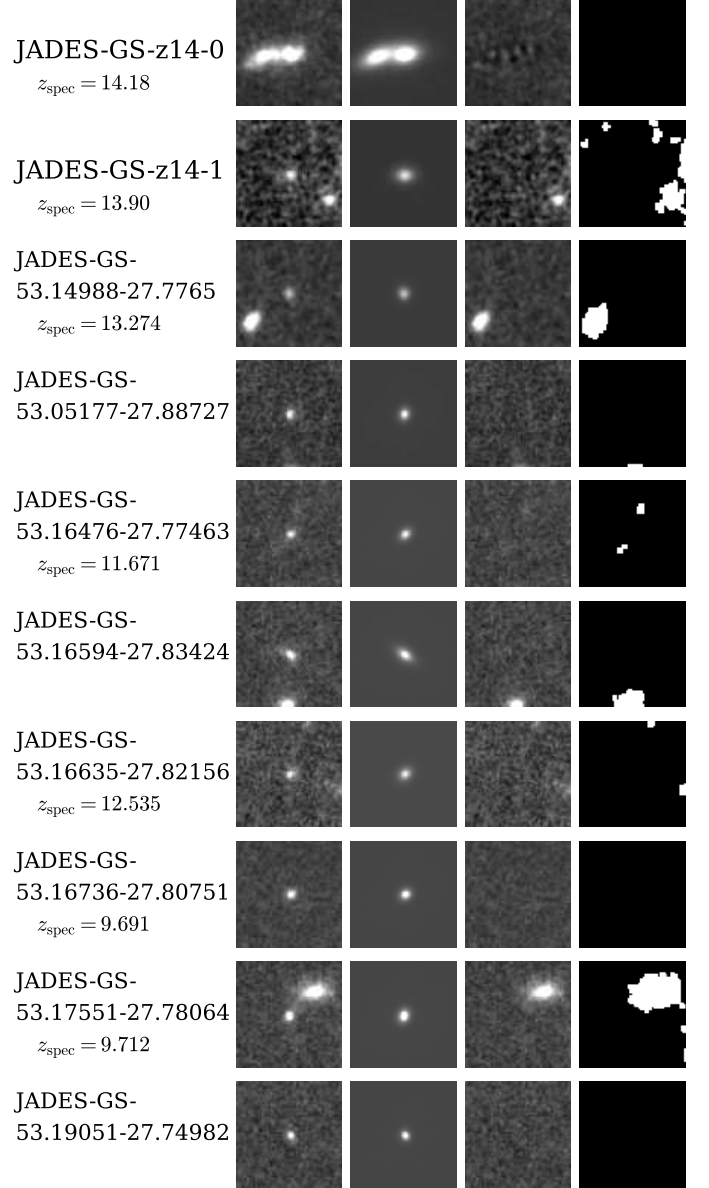


Figure 8. Same as Figure 7, but for JADES Deep.

ple,⁶ probably due to their very compact sizes and the slightly large pixel scale of the JADES images; they are excluded from this analysis for simplicity.

Figure 7, Figure 8, Figure 9, and Figure 10 present the surface brightness profile fitting results for individual objects with $S/N > 10$ in CEERS, JADES Deep, JADES Medium, and JADES GOODS-N, respectively. From left to right, each panel shows the original image

⁶ Their IDs are JADES-GS-53.06699-27.80884, JADES-GS-53.06708-27.80877, and JADES-GS-53.14528-27.82359 in JADES Deep, and JADES-GS-53.06683-27.87294 and JADES-GS-53.11763-27.88818 in JADES Medium.

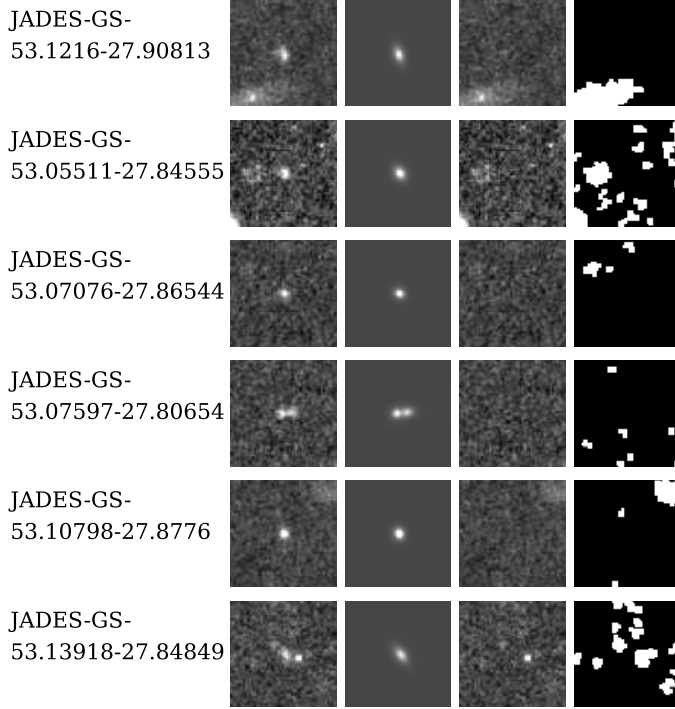


Figure 9. Same as Figure 7, but for JADES Medium.

cutout at $1''.5 \times 1''.5$, the best-fit model image, the residual image, and the segmentation map. Their pseudocolor images are shown in Figure A.1. In Figure 11, the observed and best-fit radial profiles for two galaxies in the CEERS field are presented as examples. In our fitting process, we prioritize fitting each galaxy individually. When a neighboring object is close by, we first attempt to mask it using a segmentation map to minimize its influence on the fit of the target galaxy. Alternatively, for galaxies composed of multiple components, we run the fitting on one component while masking the other using a segmentation map. However, in cases where multiple components are too close to be effectively masked, we perform simultaneous fitting for all of them. For example, CEERS-99715 and JADES-GS-53.07597-27.80654 are resolved into two components; we perform simultaneous fitting for both components and report the obtained results separately. For JADES-GS-z14-0, since a foreground object is located very close to it on the sky, we perform simultaneous fitting for JADES-GS-z14-0 and the foreground object, reporting only the results for JADES-GS-z14-0. The best-fit total magnitudes, circularized half-light radii, and axis ratios for all the individually analyzed galaxies with $S/N > 10$ are listed in Table 4. These values are corrected for systematic uncertainties and accompanied by statistical

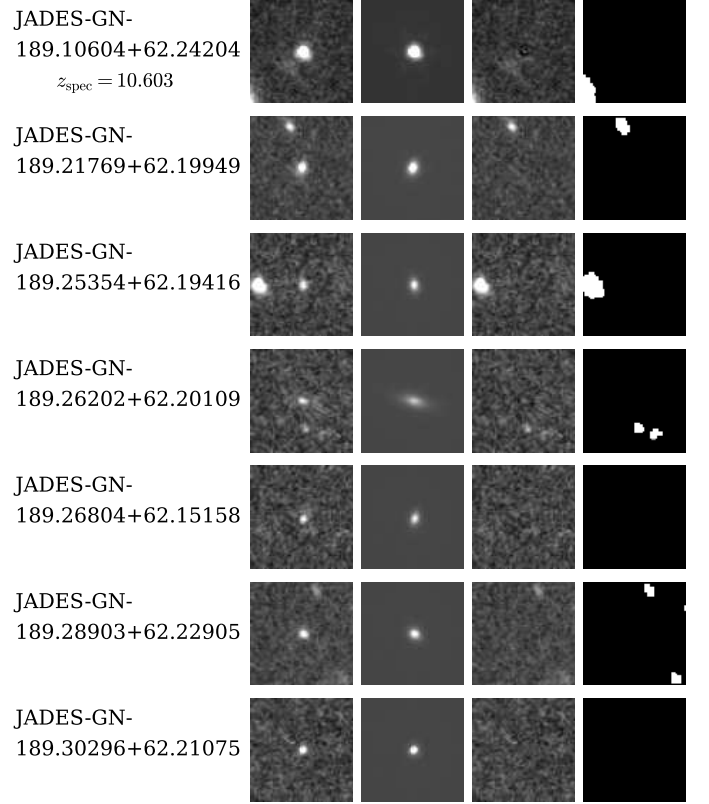


Figure 10. Same as Figure 7, but for JADES GOODS-N.

uncertainties based on our Monte Carlo simulation results.

Among the objects analyzed in this study, some luminous galaxies have been investigated in detail including their sizes in the literature. Carniani et al. (2024a) have performed surface brightness profile fitting for JADES-GS-z14-0 and JADES-GS-z14-1 using ForcePho (B. D. Johnson in preparation) and obtained results of $r_e = 260 \pm 20$ pc and $r_e < 160$ pc, respectively. Our results are consistent with these findings. Finkelstein et al. (2022) have analyzed CEERS-16943 (Maisie’s Galaxy) using GALFITM (Häußler et al. 2013), a modified version of GALFIT, and STATMORPH (Rodriguez-Gomez et al. 2019) to perform Sérsic profile fitting, and reported $r_e = 340 \pm 14$ pc. Our results are in broad agreement with their result. For GN-z11, Tacchella et al. (2023) have utilized ForcePho for surface brightness profile fitting, providing a detailed analysis that has yielded $r_e = 64 \pm 20$ pc. Our results are consistent with this previous measurement within the 1σ uncertainty range.

The sizes of the individual galaxies at $z \sim 10$ –16 obtained in this study range from compact values about 20 pc to larger values around 500 pc, with a median size of 130 pc. In Figure 12, we present the normal-

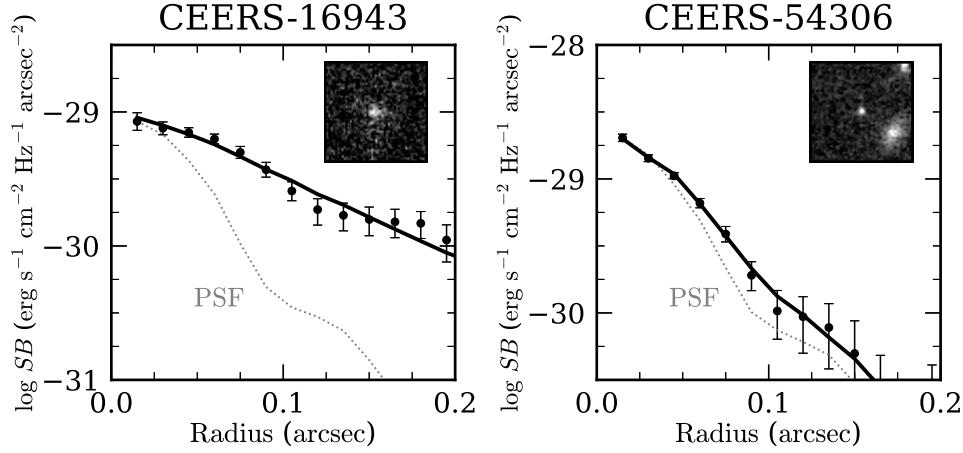


Figure 11. Radial profiles of surface brightness profile fitting results for CEERS-16943 (left) and CEERS-54306 (right) shown as examples from our sample. In each panel, the black filled circles indicate the observed radial profile, and the black solid line represents the best-fit Sérsic profile. The gray dotted line shows the normalized PSF radial profile. In the top-right corner of each panel, a $1''.5 \times 1''.5$ F200W image centered on the respective galaxy is displayed.

ized best-fit intrinsic Sérsic profiles of CEERS-16943 (Maisie’s Galaxy) and GN-z11, selected as representative extended galaxy and compact galaxy examples from our sample, respectively. Additionally, as another example of compact galaxies, we also present the normalized best-fit Sérsic profile of GHZ2, whose size is only 39 ± 11 pc as reported in Ono et al. (2023). These profiles represent the intrinsic light distributions of the galaxies before being convolved with the PSFs, allowing for a direct comparison of their structural differences. The origins of this diversity in galaxy sizes are discussed later by comparing with cosmological zoom-in simulation results in Section 5.

In particular, for the extremely compact GN-z11 and GHZ2, two possible explanations have been suggested as summarized in Harikane et al. (2024) (see also, Ono et al. 2023). One possibility is that they host AGNs. From deep NIRSpectroscopy, GN-z11 and GHZ2 exhibit high-ionization emission lines in their rest-frame UV spectra, with their emission line ratios and equivalent widths compared to photoionization models suggesting the possibility of AGN activity (for GN-z11, e.g., Bunker et al. 2023; Senchyna et al. 2024; Maiolino et al. 2024; Xu et al. 2024; Nakane et al. 2024; Álvarez-Márquez et al. 2024; for GHZ2, e.g., Castellano et al. 2024; Calabrò et al. 2024b; Zavala et al. 2024a; cf. Zavala et al. 2024b). Alternatively, the compact morphologies could result from significantly enhanced star formation efficiency due to suppressed radiative feedback in high gas surface density regions, as indicated with recent 3D radiation hydrodynamic simulations (Fukushima & Yajima 2021; see also, Kim et al. 2018; Fukushima et al. 2020). Dekel et al.

(2023) have further discussed that in the feedback-free starburst scenario, compact galaxies with high star formation efficiency can form if the density of star-forming clouds is sufficiently high. Further investigations are required to elucidate the physical origins of these compact morphologies.

Figure 13 shows the surface brightness profile fitting results for the stacked images of galaxies at $z \sim 10\text{--}16$. Since the surface brightness profile of stacked galaxies is expected to be isotropic, the axis ratio is fixed to 1, and the position angle is set to 0 deg in these fits. The best-fit total magnitudes and circularized half-light radii for these stacked galaxies are summarized in Table 5. As with the individual objects, the systematic uncertainties and statistical uncertainties in the size and total measurements are taken into account based on our Monte Carlo simulation results. The measured sizes of the stacked images of $z \sim 10\text{--}16$ galaxies are approximately in the range of 100 pc to 300 pc, with a median size of 160 pc, comparable to the sizes of the individually analyzed objects. Our results suggest that the typical size of galaxies at $z \sim 10\text{--}16$ is around 100–300 pc.

To characterize the size measurement results for high- z galaxies more quantitatively, Figure 14 shows the histogram of r_e , where r_e is displayed in natural logarithmic scale following the literature (Shibuya et al. 2015).⁷ Since the number of galaxies for which individual sizes are determined in this study is not large, we combine

⁷ In this manuscript, “ln” refers to the natural logarithm (base e) and “log” refers to the common logarithm (base 10).

Table 5. Surface Brightness Profile Fitting Results for Stacked Objects of $z \sim 10\text{--}16$ Galaxies

ID	z_{mean}	m_{UV}	M_{UV}	r_e
		(mag)	(mag)	(kpc)
(1)	(2)	(3)	(4)	(5)
CEERS				
z11-stack-CEERS	11.55	$27.80^{+0.13}_{-0.13}$	$-19.89^{+0.13}_{-0.13}$	$0.340^{+0.024}_{-0.017}$
z11-stack-CEERS-f	10.83	$28.43^{+0.06}_{-0.06}$	$-19.16^{+0.06}_{-0.06}$	$0.188^{+0.053}_{-0.046}$
JADES Deep				
z15-stack-JADES-f	14.62	$29.87^{+0.12}_{-0.08}$	$-18.15^{+0.12}_{-0.08}$	$0.059^{+0.017}_{-0.019}$
z11-stack-JADES-f	10.99	$28.98^{+0.08}_{-0.06}$	$-18.64^{+0.08}_{-0.06}$	$0.174^{+0.024}_{-0.025}$
z11-stack-JADES-f2	10.66	$29.80^{+0.08}_{-0.06}$	$-17.77^{+0.08}_{-0.06}$	$0.101^{+0.009}_{-0.010}$
JADES Medium				
z11-stack-JADESM-f	10.25	$28.81^{+0.06}_{-0.04}$	$-18.71^{+0.06}_{-0.04}$	$0.251^{+0.012}_{-0.014}$
z11-stack-JADESM-f2	10.72	$29.36^{+0.08}_{-0.06}$	$-18.22^{+0.08}_{-0.06}$	$0.142^{+0.009}_{-0.010}$
JADES GOODS-N				
z11-stack-JADESGN	11.08	$28.55^{+0.16}_{-0.11}$	$-19.08^{+0.16}_{-0.11}$	$0.116^{+0.010}_{-0.017}$
z11-stack-JADESGN-f	10.53	$28.48^{+0.05}_{-0.04}$	$-19.07^{+0.05}_{-0.04}$	$0.278^{+0.018}_{-0.024}$
z11-stack-JADESGN-f2	10.55	$29.40^{+0.16}_{-0.11}$	$-18.16^{+0.16}_{-0.11}$	$0.109^{+0.010}_{-0.018}$

NOTE—The systematic effects and statistical uncertainties in these obtained size and total magnitude measurements are considered based on our MC simulation results. (1) Object ID. The fields and luminosity ranges corresponding to each ID are summarized in Table 2. (2) Mean redshift. (3) Total apparent UV magnitude measured by GALFIT. (4) Total absolute UV magnitude, calculated using z_{mean} . (5) Circularized half-light radius $r_e = a\sqrt{b/a}$.

them into a single histogram despite the wide redshift range.⁸ To extend the redshift range examined here, we incorporate the results of Ono et al. (2024), who have individually measured the sizes of 149 galaxies at lower redshifts of $z = 4.5\text{--}9.5$ in the CEERS field using the same method as in this study. The top and middle panels are based on the results of Ono et al. (2024) for galaxies at $z = 4.5\text{--}6.0$ and $z = 6.0\text{--}9.5$, respectively, while the bottom panel represents the results of this study for galaxies at $z = 9.5\text{--}16$. Their mean redshifts are $z = 5.02$, 6.76 , and 10.94 , respectively. The median val-

ues of $\ln(r_e \text{ [kpc]})$ are -0.65 for $z = 4.5\text{--}6.0$, -1.06 for $z = 6.0\text{--}9.5$, and -2.01 for $z = 9.5\text{--}16$.⁹

Following previous work (Shibuya et al. 2015), we fit these distributions with a log-normal function:

$$p(r_e)dr_e = \frac{1}{\sqrt{2\pi}\sigma_{\ln r_e}} \exp\left(-\frac{[\ln(r_e/\bar{r}_e)]^2}{2\sigma_{\ln r_e}^2}\right) \frac{dr_e}{r_e}, \quad (2)$$

where \bar{r}_e corresponds to the half-light radius at the peak of the distribution, and $\sigma_{\ln r_e}$ represents the standard deviation of the distribution.¹⁰ The best-fit log-normal distributions are shown as solid curves in Figure 14. All the curves reasonably match the observed r_e histograms with reduced χ^2 values of $\simeq 0.3\text{--}0.9$. Note

⁸ Although our sample spans a wide range not only in redshift but also in luminosity, we present them in a single histogram due to the limited number of galaxies. However, considering the galaxy size-luminosity relation as presented in Section 4.3, this approach is suboptimal. Future studies with sufficiently larger samples should allow for a more thorough characterization of galaxy size distributions including their luminosity dependence.

⁹ These values correspond to 0.52 kpc, 0.35 kpc, and 0.13 kpc, respectively.

¹⁰ Here we follow previous studies in using natural logarithms (e.g., Shibuya et al. 2015; see also, Mo et al. 1998; Bullock et al. 2001; Gardner 2001; van den Bosch et al. 2002; Vitvitska et al. 2002; Bailin & Steinmetz 2005). However, some studies use common logarithms, which are based on 10 as the base; one should be careful when making comparisons.

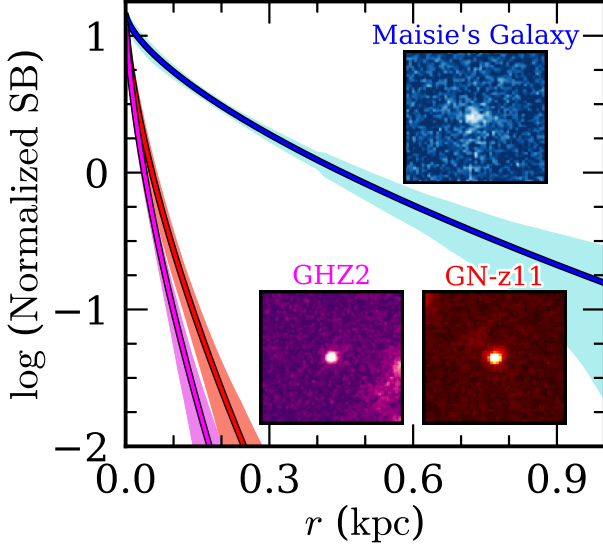


Figure 12. Normalized radial profiles of GN-z11 (red), GHZ2 (magenta), and Maisie's Galaxy (CEERS-16943, blue), selected as representative examples of a compact and an extended galaxy from the $z \sim 10\text{--}16$ galaxies analyzed in this study and Ono et al. (2023). The solid curves are the best-fit Sérsic profiles and the shaded areas indicate the 1σ uncertainties, computed from the 68th percentile ranges of radial profiles measured at randomly selected positions in the F200W images. The inset panels display $1''.5 \times 1''.5$ cutouts of the original images.

that a small number of objects with very small sizes appear to slightly deviate from the log-normal distribution. In particular, at $z = 9.5\text{--}16$, two objects are distributed around $\ln(r_e [\text{kpc}]) \simeq -4$; these are JADES-GS-53.19051-27.74982 in JADES Deep and JADES-GN-189.30296+62.21075 in JADES GOODS-N. Neither of these objects has been spectroscopically confirmed, and their nature remains unknown. Although their size measurements have relatively large uncertainties, they are interesting sources that could have sizes comparable to or even smaller than those of GN-z11 and GHZ2, which are suggested to host AGNs and/or compact star formation as described above.

The best-fit \bar{r}_e values are $\bar{r}_e = 0.503^{+0.018}_{-0.017}$ kpc for $z = 4.5\text{--}6.0$, $\bar{r}_e = 0.357^{+0.028}_{-0.026}$ kpc for $z = 6.0\text{--}9.5$, and $\bar{r}_e = 0.133^{+0.013}_{-0.012}$ kpc for $z = 9.5\text{--}16$. The best-fit standard deviations are $\sigma_{\ln r_e} = 0.59 \pm 0.03$ for $z = 4.5\text{--}6.0$, $\sigma_{\ln r_e} = 0.82 \pm 0.07$ for $z = 6.0\text{--}9.5$, and $\sigma_{\ln r_e} = 0.52 \pm 0.08$ for $z = 9.5\text{--}16$. For reference, the unbiased standard deviation of $\ln r_e$ is calculated as $0.63^{+0.05}_{-0.04}$, $0.79^{+0.09}_{-0.06}$, and $0.65^{+0.10}_{-0.07}$ for these redshift ranges, respectively. For $z = 4.5\text{--}6.0$ and $z = 6.0\text{--}9.5$, the unbiased standard deviations are consistent with the best-fit log-normal standard deviations within the 1σ

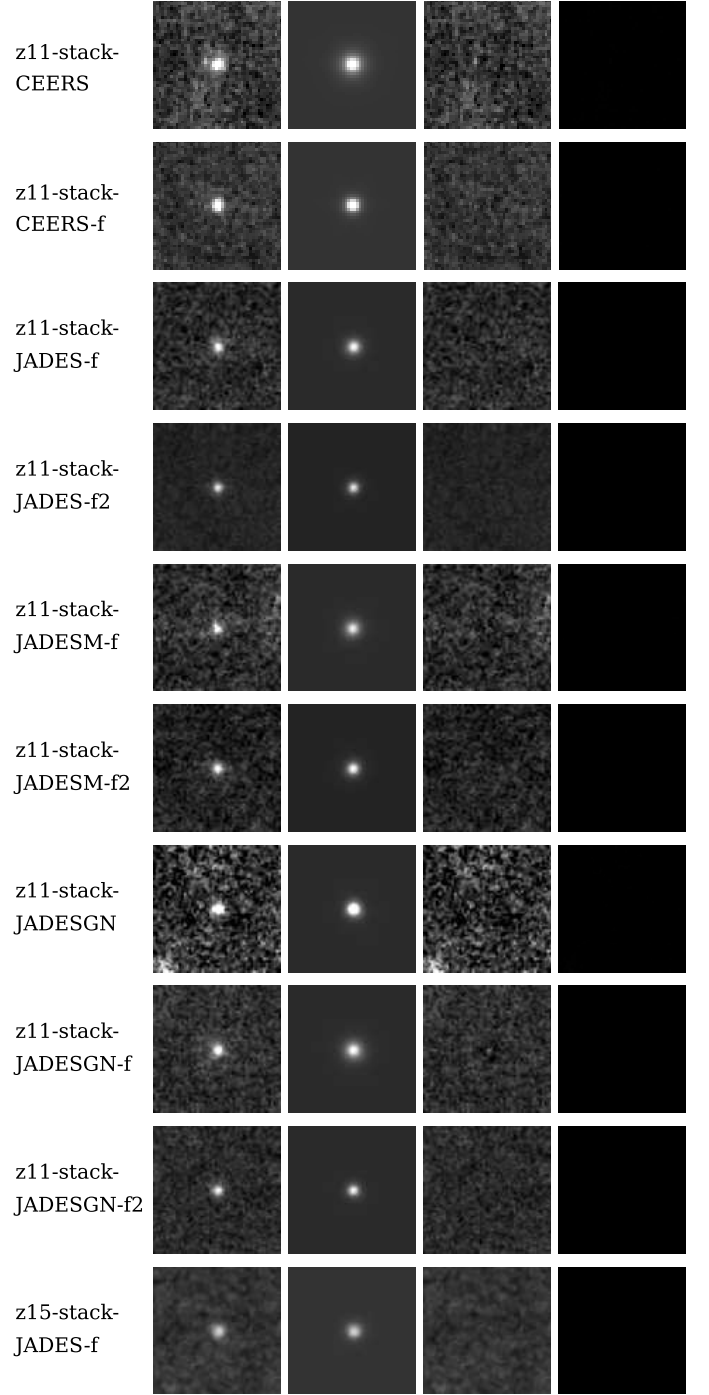


Figure 13. Same as Figure 7, but for our stacked objects. The fields and luminosity ranges corresponding to each ID are summarized in Table 2.

uncertainties. For $z = 9.5\text{--}16$, likely due to the smaller sample size, the unbiased standard deviation slightly differs from the best-fit value. However, the difference, $0.65 - 0.52 = 0.13$, is still within 2σ of the combined uncertainty, which is calculated as $\sqrt{0.08^2 + 0.07^2} \simeq 0.11$.

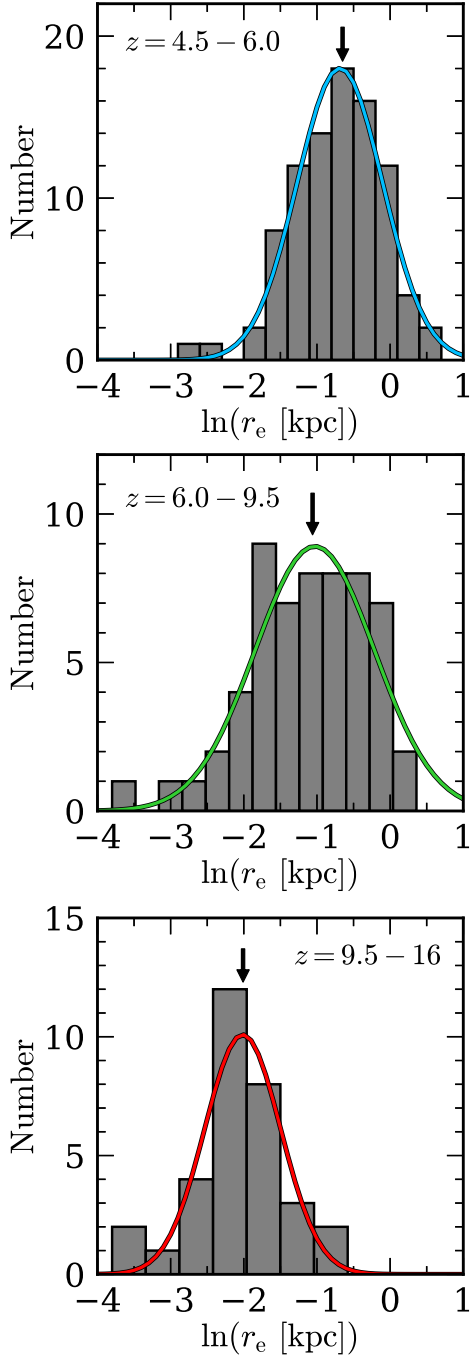


Figure 14. Distributions of r_e for high- z galaxies. The top panel shows the distribution for galaxies at $z = 4.5$ – 6.0 , the middle panel for $z = 6.0$ – 9.5 , and the bottom panel for $z = 9.5$ – 16 . The downward black arrows indicate the median r_e values. The colored curves represent the best-fit log-normal distributions.

Figure 15 presents the standard deviations of galaxy size distributions as a function of redshift, combining results from this study with those from previous

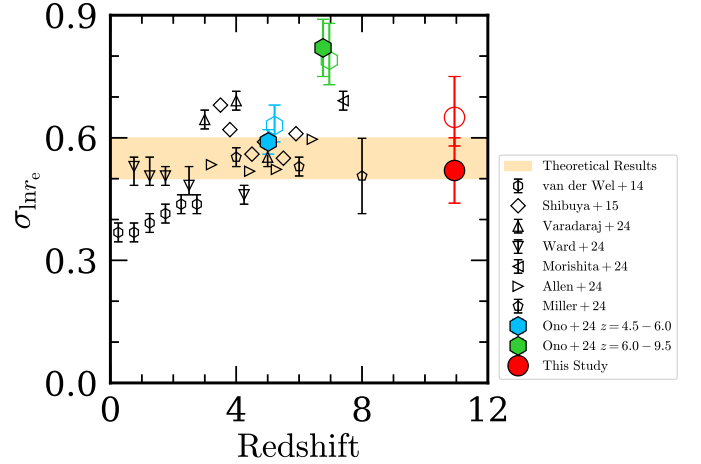


Figure 15. Standard deviation of the log-normal size distribution, $\sigma_{\ln r_e}$, as a function of redshift. The red filled circle represents the results for $z \sim 10$ – 16 galaxies in this study, while the green and cyan filled hexagons represent the results for $z = 6.0$ – 9.5 and $z = 4.5$ – 6.0 galaxies, respectively, based on the size measurement results of Ono et al. (2024). The corresponding open symbols in these colors indicate the unbiased standard deviations, and for clarity, those at $z = 6.0$ – 9.5 and $z = 4.5$ – 6.0 are shifted by $+0.2$ in redshift. The black open symbols represent results from previous studies, with the symbol shapes and corresponding references shown in the legend (van der Wel et al. 2014; Shibuya et al. 2015; Varadaraj et al. 2024; Ward et al. 2024; Morishita et al. 2024; Allen et al. 2024; Miller et al. 2024). The orange shaded region shows the width of the spin parameter λ distribution, $\sigma_{\ln \lambda}$, predicted from theoretical studies (e.g., Mo et al. 1998; Bullock et al. 2001; Gardner 2001; van den Bosch et al. 2002; Vitvitska et al. 2002; Bailin & Steinmetz 2005; Davis & Natarajan 2009; Zjupa & Springel 2017).

studies (van der Wel et al. 2014; Shibuya et al. 2015; Varadaraj et al. 2024; Ward et al. 2024; Morishita et al. 2024; Allen et al. 2024; Miller et al. 2024). For the redshift value of the data point from Morishita et al. (2024), we use the median redshift of the galaxies in their catalog. Previous observational studies have reported that the $\sigma_{\ln r_e}$ values range from approximately 0.4 to 0.7 across a wide range of redshifts, showing no significant evolution. The standard deviation of the size distribution derived from the results of Ono et al. (2024) is broadly consistent with these earlier findings. Moreover, the standard deviation of the size distribution for $z \sim 10$ – 16 galaxies obtained in this study is also comparable to the values reported at lower redshifts within the 1σ uncertainty. This indicates that $\sigma_{\ln r_e}$ shows no clear evolution toward $z \gtrsim 10$. The implication of this result for the disk formation scenario is discussed in Section 5.

4.2. Axis Ratio Distribution

We investigate the axis ratio distribution of $z \sim 10\text{--}16$ galaxies. Figure 16 shows the axis ratio distribution for the $z \sim 10\text{--}16$ galaxies whose axis ratios are individually determined through profile fitting in this study. Although the number of the high- z galaxies is limited, resulting in a coarse frequency distribution, the number of objects appears to be roughly constant across b/a values from 0.2 to 0.8, suggesting a distribution close to uniform.

As is well known from observations of local galaxies, the axis ratio distribution for elliptical galaxies peaks around 0.8 and decreases for both larger and smaller values. In contrast, the axis ratio distribution for spiral galaxies is nearly uniform (Lambas et al. 1992). A similar uniform distribution has also been obtained for star-forming galaxies at $z \sim 1\text{--}5$ (Ravindranath et al. 2006; see also, Ferguson et al. 2004). For comparison, Figure 16 also displays the axis ratio distributions for local elliptical and spiral galaxies, scaled appropriately, alongside the obtained distribution for our $z \sim 10\text{--}16$ galaxies. As can be seen from the figure, the axis ratio distribution for the $z \sim 10\text{--}16$ galaxies is closer to that of local spiral galaxies than to that of local elliptical galaxies.

To quantitatively evaluate this visual similarity, we use the Kolmogorov-Smirnov (K-S) test to examine whether the axis ratio distribution of our $z \sim 10\text{--}16$ galaxies is statistically consistent with those of local elliptical and spiral galaxies. The K-S test is a non-parametric test that assesses the maximum vertical distance (K-S statistic D) between the empirical cumulative distribution functions of two samples.

We perform the K-S test using our raw axis ratio data for the $z \sim 10\text{--}16$ galaxies and the axis ratio distribution data for local elliptical and spiral galaxies from Lambas et al. (1992). Here we adopt a statistical significance level of $\alpha = 0.01$. As a result, comparing our galaxy distribution with that of local elliptical galaxies, we obtain $D = 0.3590$ and a p -value of 0.0004, which is much smaller than the significance level, providing strong evidence to reject the null hypothesis that both distributions are the same. This indicates that the axis ratio distribution of our $z \sim 10\text{--}16$ galaxies is statistically significantly different from that of local elliptical galaxies. On the other hand, when comparing our galaxy distribution with that of local spiral galaxies, we obtain $D = 0.1876$ and a p -value of 0.1849. Since this p -value is larger than the significance level, we cannot reject the null hypothesis, indicating that there is no statistically significant difference between the axis ratio distribution of our $z \sim 10\text{--}16$ galaxies and that of local

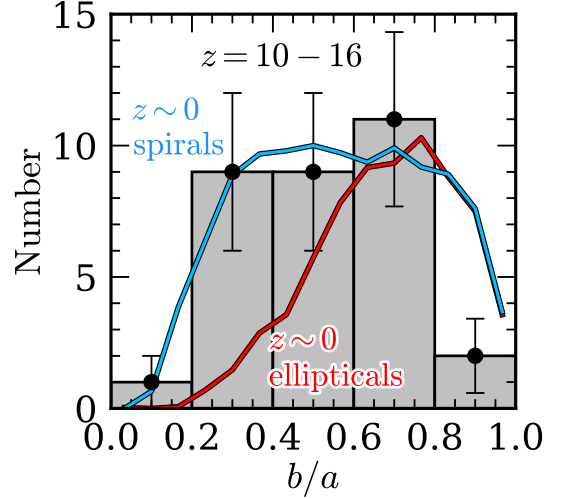


Figure 16. Axis ratio b/a distribution. The black circles and gray histogram represent the axis ratio distribution of the $z \sim 10\text{--}16$ galaxies investigated in this study. The cyan and red solid lines denote the axis ratio distributions of local spiral and elliptical galaxies, respectively, obtained by Lambas et al. (1992) and scaled appropriately.

spiral galaxies. These quantitative results corroborate our visual inspection, statistically suggesting that the axis ratio distribution of $z \sim 10\text{--}16$ galaxies differs from that of local elliptical galaxies and is instead closer to the uniform distribution observed in local spiral galaxies.

4.3. Size-UV Luminosity Relation

We investigate the relation between size and UV luminosity for $z \sim 10\text{--}16$ galaxies. Figure 17 plots the size-luminosity relation for our $z \sim 10\text{--}16$ galaxy sample, along with the galaxies at similar redshifts analyzed in the literature (Yang et al. 2022; Ono et al. 2023). As noted in Section 4.1, the sizes of galaxies with $M_{\text{UV}} \lesssim -20$ mag show significant variation, ranging from relatively large sizes of up to around 500 pc to very small sizes below 100 pc such as GN-z11 and GHZ2. As described there, the compact morphologies are suggested to originate from AGN activity and/or compact star formation. For the latter case, a comparison with cosmological zoom-in simulations is presented in Section 5.

Note that, among the three objects overlapped with the little red dots selected by Kocevski et al. (2024), CEERS-98518 is the only object with an aperture magnitude $S/N > 10$ and is marked with a large green circle in Figure 17. Its size is not remarkably small compared to the other galaxies with comparable UV luminosities at similar redshifts. Although little red dots are often

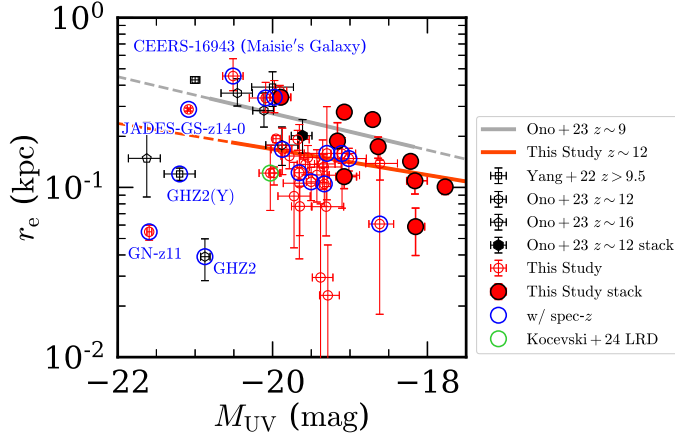


Figure 17. Relation between galaxy size r_e and M_{UV} . The red open circles represent the results for relatively luminous $z \sim 10$ – 16 galaxies analyzed individually in this study, while the red filled circles show the results for stacked images of relatively faint $z \sim 10$ – 16 galaxies. The red solid line denotes the best-fit size–luminosity relation for our $z \sim 10$ – 13 galaxies, and the red dashed line indicates its extrapolation. The black open symbols represent the results for relatively luminous $z \sim 10$ – 16 galaxies analyzed individually in previous studies, and the black filled hexagon represents the results for stacked images from previous studies (Yang et al. 2022; Ono et al. 2023). The blue large circles indicate spectroscopically confirmed galaxies (Finkelstein et al. 2024; Hainline et al. 2024; Carniani et al. 2024a; Castellano et al. 2024; Schouws et al. 2024; Carniani et al. 2024b). The large green circle represents the object included in the catalog of little red dots (Kocevski et al. 2024). The names of the well-studied galaxies GN-z11, GHZ2, JADES-GS-z14-0, and CEERS-16943 (Maisie’s Galaxy) are labeled in blue near their respective data points. GHZ2(Y) indicates the measurement result for GHZ2 obtained by Yang et al. (2022). The gray solid line shows the best-fit size–luminosity relation for $z \sim 9$ galaxies obtained in previous studies, and the gray dashed line indicates its extrapolation (Ono et al. 2023).

selected as compact objects in the rest-frame optical (e.g., Matthee et al. 2024; Pérez-González et al. 2024; Kokorev et al. 2024; Kocevski et al. 2024), our results may indicate that they are not necessarily as compact as point sources in the rest-frame UV probably because of the significant contribution from the stellar component (see also, Rinaldi et al. 2024).

Following previous studies (e.g., Grazian et al. 2012; Ono et al. 2013; Huang et al. 2013; Jiang et al. 2013; Kawamata et al. 2015; Shibuya et al. 2015; Holwerda et al. 2015; Curtis-Lake et al. 2016; Bowler et al. 2017; Bouwens et al. 2017; Kawamata et al. 2018; Holwerda et al. 2020; Bouwens et al. 2022; Yang et al. 2022; Ono et al. 2023;

Sun et al. 2024; Morishita et al. 2024; Varadaraj et al. 2024), to characterize the size–luminosity relation, we fit a power-law function to the data points,

$$r_e = r_0 \left(\frac{L_{UV}}{L_0} \right)^\alpha, \quad (3)$$

where r_0 is the effective radius at the luminosity of L_0 , corresponding to -21.0 mag (Huang et al. 2013; Shibuya et al. 2015), and α is the slope of the size–luminosity relation. Since galaxy sizes evolve with redshift as presented in the next subsection, we fit the power-law function to the data points for $z = 9.5$ – 13 galaxies in our sample, as well as the $z \sim 12$ data points from Ono et al. (2023), to limit the impact of redshift evolution by restricting the redshift range. We do not perform the fit for the $z = 13$ – 16 data points, as their small sample size prevents a reliable constraint. With this approach, we obtain best-fit values of $r_0 = 0.20 \pm 0.01$ kpc and $\alpha = 0.19 \pm 0.03$. In this fitting, we exclude GN-z11 and GHZ2, for which the presence of AGN has been suggested (Section 4.1). For r_0 , Shibuya et al. (2015) fit their results with a functional form $r_0 \propto (1+z)^{\beta z}$, as shown in their Figure 10. Compared to their extrapolated results, our value for r_0 is slightly smaller but broadly consistent. For α , we find a slightly smaller value compared to Shibuya et al. (2015).

For comparison, we also show the size–luminosity relation obtained in previous studies for galaxies at a slightly lower redshift of $z \sim 9$ (Ono et al. 2023). At the same UV luminosity, our results suggest that the sizes of $z \sim 10$ – 16 galaxies are slightly smaller on average.

Next, we compare the star formation rate (SFR) surface densities, Σ_{SFR} , of the $z \sim 10$ – 16 galaxies with previous results for lower- z galaxies. The SFRs of the $z \sim 10$ – 16 galaxies are derived from the UV luminosities using the following equation:

$$SFR = 1.4 \times 10^{-28} \alpha_{SC} L_\nu, \quad (4)$$

where L_ν is the rest-frame UV luminosity density in units of $\text{erg s}^{-1} \text{Hz}^{-1}$ (Kennicutt 1998). We multiply by the factor $\alpha_{SC} = 0.63$ (Madau & Dickinson 2014) to convert from the Salpeter initial mass function (IMF; Salpeter 1955) to the Chabrier IMF (Chabrier 2003). Dust extinction is not corrected here, since high- z galaxies tend to exhibit blue UV slopes (e.g., Topping et al. 2024; Cullen et al. 2024; Roberts-Borsani et al. 2024; Austin et al. 2024; Saxena et al. 2024; Yanagisawa et al. 2024). In this conversion, we assume that the UV luminosities originate from star formation for all objects analyzed in this study including GN-z11 and GHZ2. We then calculate the SFR surface density in units of $M_\odot \text{yr}^{-1} \text{kpc}^{-2}$. This

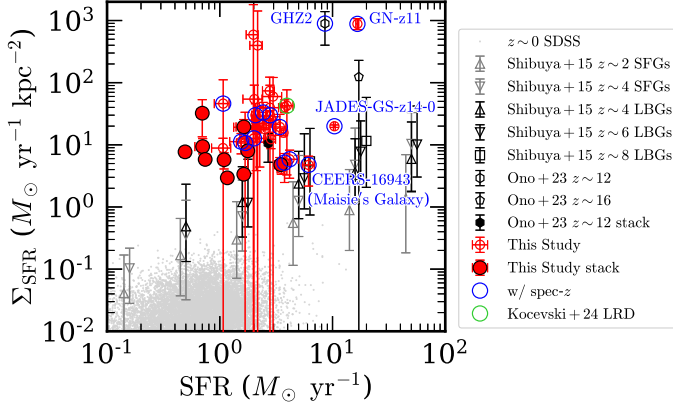


Figure 18. SFR surface density Σ_{SFR} vs. SFR. The red open circles show the results for relatively luminous $z \sim 10\text{--}16$ galaxies individually analyzed in this study. The red filled circles indicate the results for stacked images of fainter $z \sim 10\text{--}16$ galaxies. The black pentagons and hexagons represent previous results at similar redshifts (Ono et al. 2023). Among them, those marked with large blue circles correspond to spectroscopically confirmed galaxies (Finkelstein et al. 2024; Hainline et al. 2024; Carniani et al. 2024a; Castellano et al. 2024; Schouws et al. 2024; Carniani et al. 2024b). The large green circle denotes the object included in the catalog of little red dots (Kocevski et al. 2024). The names of well-studied objects, GN-z11, GHZ2, JADES-GS-z14-0, and CEERS-16943 (Maisie’s Galaxy), are labeled near their respective data points. The gray dots represent $z \sim 0$ galaxies compiled by Shibuya et al. (2015) from the Sloan Digital Sky Survey (SDSS), with Σ_{SFR} values calculated using the catalog of Lackner & Gunn (2012). The other black and gray data points are the results for $z \sim 2\text{--}8$ galaxies reported by Shibuya et al. (2015).

quantity represents the average SFR within a circular region enclosed by the half-light radius, given by

$$\Sigma_{\text{SFR}} = \frac{\text{SFR}}{2\pi r_e^2}, \quad (5)$$

where the factor 1/2 is included because the SFR is estimated based on the total luminosity, while the area used for division is based on the half-light radius (e.g., Hathi et al. 2008; Tacconi et al. 2013; Decarli et al. 2016).

Figure 18 plots the SFR surface density on the vertical axis and the SFR on the horizontal axis, comparing the $z \sim 10\text{--}16$ galaxies analyzed in this study with lower- z galaxies investigated in previous work. As expected from the evolution of the size–UV luminosity relation, the Σ_{SFR} values increase on average with redshift even beyond $z = 10$, which is consistent with previous results (Ono et al. 2023). The Σ_{SFR} values are on average comparable to those obtained within the frame-

work of the L-GALAXIES2020 semi-analytical model by Nadolny et al. (2025). Interestingly, the extremely compact luminous sources GN-z11 and GHZ2 exhibit very high Σ_{SFR} values, around $1000 M_\odot \text{ yr}^{-1} \text{ kpc}^{-2}$, and occupy a distinct region in this plane compared to other galaxies. This origin can be attributed to the two possibilities described in Section 4.1.

4.4. Size Evolution

We investigate the size evolution of galaxies. Figure 19 shows the measured half-light radii of our $z \sim 10\text{--}16$ galaxies plotted as a function of redshift, along with results from previous studies. Since galaxy size depends on UV luminosity, we follow previous studies and divide the data into two luminosity ranges: $L/L_{z=3}^* = 0.3\text{--}1$ and $0.12\text{--}0.3$.

The size evolution of galaxies has been characterized in previous studies using the functional form $r_e \propto (1+z)^s$ (e.g., Ferguson et al. 2004; Bouwens et al. 2004; Bouwens et al. 2006; Hathi et al. 2008; Oesch et al. 2010; Ono et al. 2013; Kawamata et al. 2015; Holwerda et al. 2015; Shibuya et al. 2015; Curtis-Lake et al. 2016; Allen et al. 2017; Kawamata et al. 2018; Bridge et al. 2019; Holwerda et al. 2020), where s represents the slope of the power-law relation. We fit this functional form to these data points. For the uncertainty in the Shibuya et al. (2015) data points, we follow their methodology and use the 68th percentile of the size distribution of individual galaxies. For the uncertainties in the other data points, we use the measurement uncertainties of the individual galaxy sizes. As a result, we obtain $s = -1.28^{+0.26}_{-0.22}$ for $L/L_{z=3}^* = 0.3\text{--}1$ and $s = -1.52^{+0.20}_{-0.19}$ for $L/L_{z=3}^* = 0.12\text{--}0.3$. The slope for the brighter luminosity sample is consistent with the previous results of Ono et al. (2023), while the slope for the fainter luminosity bin is slightly smaller than the previous results beyond the 1σ uncertainty. This may be due to the limited number of high- z galaxies in the previous work.

Table 6 compiles a summary of previously reported power-law slopes from various studies. Observations primarily based on HST data generally show convergence towards slope values between approximately -1.0 and -1.5 . Several recent studies utilizing JWST data have reported slopes with significantly smaller absolute values. While a detailed investigation into the exact reasons of these differences is beyond the scope of this paper, they may arise from variations in sample selection (e.g., stellar mass-selected versus UV luminosity-

Table 6. Summary of Galaxy Size Evolution Results

Reference	Telescope	Software	Redshift	Rest-frame	Luminosity or	s of $(1+z)^s$
(1)	(2)	(3)	Range	Wavelength	M_{star} Range	(7)
Bouwens et al. (2004)	HST	SExtractor	2–6	UV	—	-1.05 ± 0.21
Ferguson et al. (2004)	HST	SExtractor	2–5	UV	—	$\sim -1.5^{\dagger 1}$
Bouwens et al. (2006)	HST	SExtractor	~ 6	UV	—	-1.1 ± 0.3
Hathi et al. (2008)	HST	SExtractor	4–6	UV	—	$\sim -1.5^{\dagger 1}$
Oesch et al. (2010)	HST	SExtractor	7–8	UV	$(0.3-1)L_{z=3}^*$	-1.12 ± 0.17
					$(0.12-0.3)L_{z=3}^*$	-1.32 ± 0.52
Mosleh et al. (2012)	HST	GALFIT	4–7	UV	$10^{9.5-10.4} M_{\odot}$	-1.20 ± 0.11
					$10^{8.6-9.5} M_{\odot}$	-1.18 ± 0.10
Ono et al. (2013)	HST	GALFIT	7–8	UV	$(0.12-1)L_{z=3}^*$	$-1.30^{+0.12}_{-0.14}$
Kawamata et al. (2015)	HST	glafic	6–8	UV	$(0.3-1)L_{z=3}^*$	-1.24 ± 0.1
Holwerda et al. (2015)	HST	GALFIT	9–10	UV	$> 0.3L_{z=3}^*$	-1.04 ± 0.09
					$< 0.3L_{z=3}^*$	-0.8 ± 0.1
Shibuya et al. (2015)	HST	GALFIT	4–10	UV	$(0.3-1)L_{z=3}^*$	-1.10 ± 0.06
					$(0.12-0.3)L_{z=3}^*$	-1.22 ± 0.05
Curtis-Lake et al. (2016)	HST	SExtractor	4–8	UV	$(0.3-1)L_{z=3}^*$	-0.20 ± 0.26
					$(0.12-0.3)L_{z=3}^*$	-0.47 ± 0.62
Allen et al. (2017)	HST	GALFIT	1–7	UV	$> 10^{10} M_{\odot}$	-0.89 ± 0.01
Kawamata et al. (2018)	HST	glafic	6–9	UV	$(0.3-1)L_{z=3}^*$	-1.28 ± 0.11
Ono et al. (2023)	JWST	GALFIT	9–16	UV	$(0.3-1)L_{z=3}^*$	$-1.22^{+0.17}_{-0.16}$
					$(0.12-0.3)L_{z=3}^*$	-1.17 ± 0.16
Morishita et al. (2024)	JWST	GALFIT	5–14	UV	$—^{\dagger 2}$	-0.4 ± 0.2
Sun et al. (2024)	JWST	GALFITM	4–10	optical	$10^{9.4-10.5} M_{\odot}$	-1.27 ± 0.60
					$10^{8-9.4} M_{\odot}$	-1.39 ± 0.33
Ormerod et al. (2024)	JWST	GALFIT	1–8	optical	$> 10^{9.5} M_{\odot}$	-0.71 ± 0.19
Varadaraj et al. (2024)	JWST	PYAUTOGALAXY	3–5	optical	$> 10^9 M_{\odot}$	-0.60 ± 0.22
Ward et al. (2024)	JWST	GALFITM	0.5–5.5	optical	$5 \times 10^{10} M_{\odot}^{\dagger 3}$	-0.63 ± 0.07
Allen et al. (2024)	JWST	GALFITM	3–9	optical	$5 \times 10^{10} M_{\odot}^{\dagger 3}$	-0.807 ± 0.026
Westcott et al. (2024)	JWST	GALFIT	7–13	optical/UV	—	-0.67 ± 0.06
Yang et al. (2025)	JWST	GaLight	2–10	optical/UV	$> 10^9 M_{\odot}$	-1.21 ± 0.05
This Study	JWST	GALFIT	10–16	UV	$(0.3-1)L_{z=3}^*$	$-1.28^{+0.26}_{-0.22}$
					$(0.12-0.3)L_{z=3}^*$	$-1.52^{+0.20}_{-0.1}$

NOTE—(1) Reference. (2) Telescope used to obtain the imaging data. (3) Software used for size measurements. (4) Redshift range of the galaxy sample whose sizes are measured. (5) Rest-frame wavelength in which size evolution is investigated. (6) Luminosity or stellar mass range of the galaxies used for fitting the size evolution. (7) Power-law index of $(1+z)$ fitted to the measured size evolution.

^{†1} Technically, reported to follow $\propto H(z)^{-1}$.

^{†2} Sizes corrected based on the size-stellar mass relation are used.

^{†3} Sizes at a specific stellar mass based on the size-stellar mass relation are used.

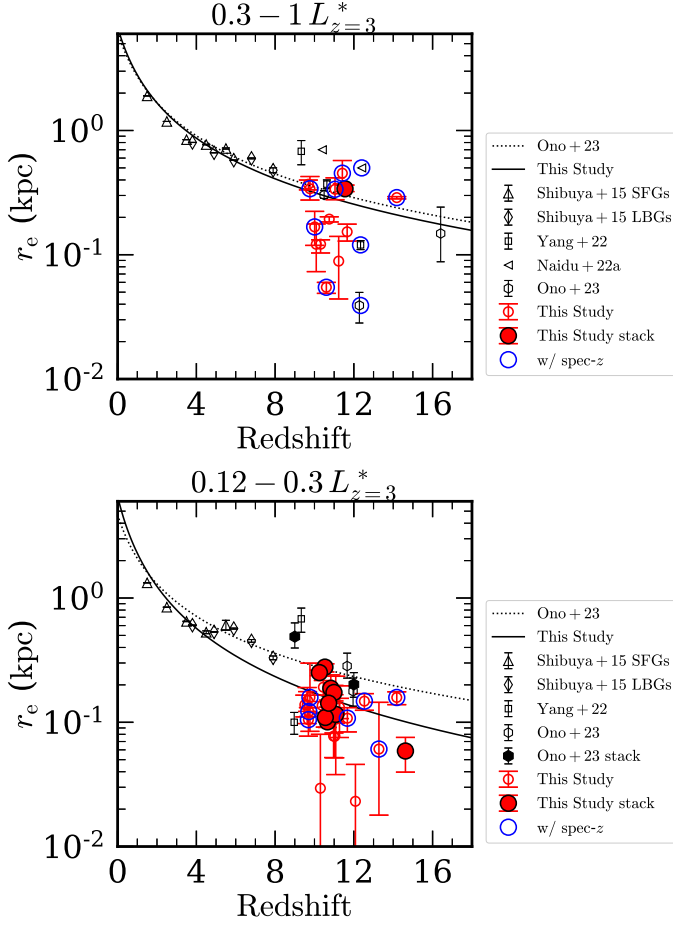


Figure 19. Evolution of the half-light radius of star-forming galaxies with UV luminosities in the ranges $(0.3\text{--}1) L_{z=3}^*$ (top) and $(0.12\text{--}0.3) L_{z=3}^*$ (bottom). The red open circles correspond to the sizes of relatively luminous $z \sim 10\text{--}16$ galaxies measured individually in this study, while the red filled circles represent the results for stacked images of fainter $z \sim 10\text{--}16$ galaxies. The black open symbols show the sizes of star-forming galaxies analyzed individually in previous studies, and the black filled hexagon indicates the results for stacked images in previous studies (Shibuya et al. 2015; Yang et al. 2022; Ono et al. 2023). The blue large circles mark spectroscopically confirmed galaxies (Finkelstein et al. 2024; Hainline et al. 2024; Carniani et al. 2024a; Castellano et al. 2024; Schouws et al. 2024; Carniani et al. 2024b). The solid curve shows the best-fit $r_e \propto (1+z)^s$ function derived in this study, while the dotted curve represents the best-fit result from Ono et al. (2023).

selected samples), the specific redshift ranges adopted for power-law fitting, and/or the rest-frame wavelength at which the sizes are measured.

5. DISCUSSION

5.1. Implications of the Log-Normal Size Distribution: Are $z \sim 10\text{--}16$ Galaxies Disk Galaxies?

Previous studies have shown that the sizes of star-forming galaxies at $z \sim 0\text{--}6$ follow a log-normal distribution with a standard deviation of $\sigma_{\ln r_e} \sim 0.4\text{--}0.7$ independent of redshift (Shibuya et al. 2015; see also, Kawamata et al. 2015; Kawamata et al. 2018). They have also reported that the Sérsic index is typically as low as $\simeq 1.5$ and that the stellar-to-halo size ratio r_e/r_{vir} , which is the ratio of galaxy size to host dark matter halo size, remains nearly constant at approximately 0.02. According to the galaxy disk formation scenario, the rotationally supported gas that forms the basis of the galaxy disk acquires angular momentum from the host dark matter halo through tidal interactions (e.g., Fall & Efstathiou 1980; White 1984; Barnes & Efstathiou 1987), and the galaxy size is expected to be proportional to r_{vir} and the dark matter halo spin parameter λ (Equation 28 of Mo et al. 1998; see also, Kravtsov 2013). Moreover, theoretical studies suggest that λ follows a log-normal distribution with a standard deviation of $\sigma_{\ln \lambda} \sim 0.5\text{--}0.6$ (e.g., Mo et al. 1998; Bullock et al. 2001; Gardner 2001; van den Bosch et al. 2002; Vitvitska et al. 2002; Bailin & Steinmetz 2005; Davis & Natarajan 2009; Zjupa & Springel 2017; see also, Warren et al. 1992; Steinmetz & Bartelmann 1995; Bett et al. 2007), which is similar to those of the galaxy size distributions. Based on these results, it has been suggested that typical star-forming galaxies at $z \sim 0\text{--}6$ have stellar components that can be explained by the galaxy disk formation scenario (Shibuya et al. 2015).

In Section 4.1, based on the deep JWST images and incorporating the results from our previous work, we have demonstrated that the size distribution of galaxies at $z \sim 4\text{--}16$ also follows a log-normal distribution (Figure 14). Furthermore, by combining our results with those from previous studies (van der Wel et al. 2014; Shibuya et al. 2015; Varadaraj et al. 2024; Ward et al. 2024; Morishita et al. 2024; Allen et al. 2024; Miller et al. 2024), we have reported that the standard deviation of the log-normal distribution of galaxy sizes shows no clear evolution toward $z \gtrsim 10$ (Figure 15). Additionally, for the $z \sim 10\text{--}16$ galaxies investigated in this study, we have derived their axis ratio distribution in Section 4.2, finding it to be nearly uniform across $b/a \sim 0.2\text{--}0.8$, similar to the distribution observed for local spiral galaxies.

In this section, we further estimate the stellar-to-halo size ratio, r_e/r_{vir} , for the $z \sim 10\text{--}16$ galaxies analyzed in this study. The virial radii of the host dark matter halos for the $z \sim 10\text{--}16$ galaxies are calculated based

on their UV luminosities through the SFR and stellar mass, as follows, although the systematic uncertainties are not small. First, the SFRs of the $z \sim 10\text{--}16$ galaxies are derived from the UV luminosities using Equation 4. Next, based on the SFRs, we estimate the stellar masses of the $z \sim 10\text{--}16$ galaxies using the star formation main sequence relation given as Equation 5 of Cole et al. (2023) (see also their Table 2).¹¹ Subsequently, the virial masses of the host dark matter halos are calculated using the stellar mass – halo mass relations from Behroozi et al. (2019) (see the right panel of their Figure 9). Specifically, we employ their Equations J1–J8 and adopt the parameter values listed in the top row of their Table J. Note that their relations show a turnover at high redshifts, where stellar mass decreases with increasing halo mass, and the turnover mass decreases with redshift. For some of our galaxies, particularly the luminous ones at high redshifts, the derived halo mass exceeds the turnover mass, making it impossible to determine the halo mass. For such cases, we simply scale the $z = 9$ stellar mass – halo mass relation for our analysis. Finally, the virial radius r_{vir} is calculated from the halo mass using the following equation:

$$r_{\text{vir}} = \left(\frac{2GM_{\text{vir}}}{\Delta_{\text{vir}}H(z)^2} \right)^{1/3}, \quad (6)$$

where $\Delta_{\text{vir}} = 18\pi^2 + 82x - 39x^2$ and $x = \Omega_m(z) - 1$ (Bryan & Norman 1998; see also, Kawamata et al. 2015; Shibuya et al. 2015; Kawamata et al. 2018).

Figure 20 shows r_e/r_{vir} as a function of redshift. The $z \sim 10\text{--}16$ galaxies analyzed in this study exhibit r_e/r_{vir} values of $\simeq 0\text{--}0.04$, with a median value and 68th percentile range of $r_e/r_{\text{vir}} = 0.015^{+0.015}_{-0.005}$. Previous studies have reported that the r_e/r_{vir} values for galaxies at $z \sim 0\text{--}8$ remain approximately constant at $r_e/r_{\text{vir}} \simeq 0.02$ (Kawamata et al. 2015; Shibuya et al. 2015; Kawamata et al. 2018; see also, Salucci et al. 2007; Huang et al. 2017). Very recently, Yang et al. (2025) have estimated r_e/r_{vir} values for $z \sim 2\text{--}10$ galaxies based on JWST COSMOS-Web data, obtaining a median value of approximately 0.027. Our results indicate that this trend continues to higher redshifts, up to $z \sim 16$, with no significant evolution.

As described above, the size distribution of $z \sim 10\text{--}16$ galaxies can be explained by a log-normal distribution, with its standard deviation comparable to that of the

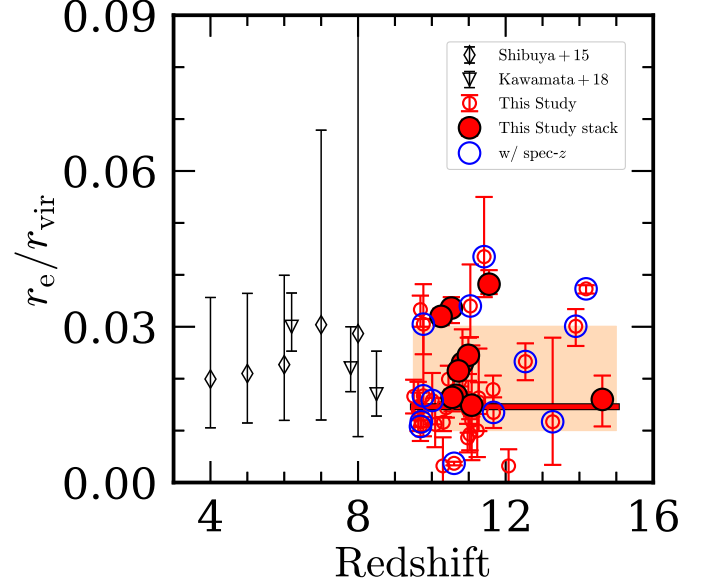


Figure 20. Ratio of galaxy UV continuum size to host dark matter halo size, r_e/r_{vir} , as a function of redshift. The red open circles represent the results of relatively luminous $z \sim 10\text{--}16$ galaxies measured individually in this study, while the red filled circles show the results for stacked images of fainter $z \sim 10\text{--}16$ galaxies. The blue large circles indicate spectroscopically confirmed galaxies (Finkelstein et al. 2024; Hainline et al. 2024; Carniani et al. 2024a; Castellano et al. 2024; Schouws et al. 2024; Carniani et al. 2024b). The red solid line represents the median of the results for the individually analyzed galaxies in this study, and the orange shaded region indicates the 68th percentile range. The black diamonds and downward triangles indicate the results from previous studies of $z \sim 4\text{--}8$ star-forming galaxies (Shibuya et al. 2015; Kawamata et al. 2018).

spin parameter of dark matter halos. Moreover, their axis ratio distribution is similar to that of local spiral galaxies. Additionally, the stellar-to-halo size ratio remains nearly constant regardless of redshift. Furthermore, as reported in Section 3, the median Sérsic index for the luminous $z \sim 10\text{--}16$ galaxies in our sample is consistent with the exponential disk profile. These findings suggest that $z \sim 10\text{--}16$ galaxies, like the star-forming galaxies at lower redshifts studied in previous work, have stellar components that are consistent with the galaxy disk formation scenario. This may imply that stellar feedback is not very effective in these high- z galaxies, which could be attributed to the compact nature of these high- z galaxies, a consequence of the smaller virial radii of dark matter halos at higher redshifts for a given stellar mass.

Recent simulations have shown that at high redshifts, supernova feedback can significantly disrupt galaxy

¹¹ For galaxies at $z \gtrsim 10$, the uncertainties of the stellar mass estimates would not be small, because NIRCам only probes their rest-frame UV. Additional data, such as those from MIRI, are required to probe the rest-frame optical and improve the accuracy of the stellar mass estimates.

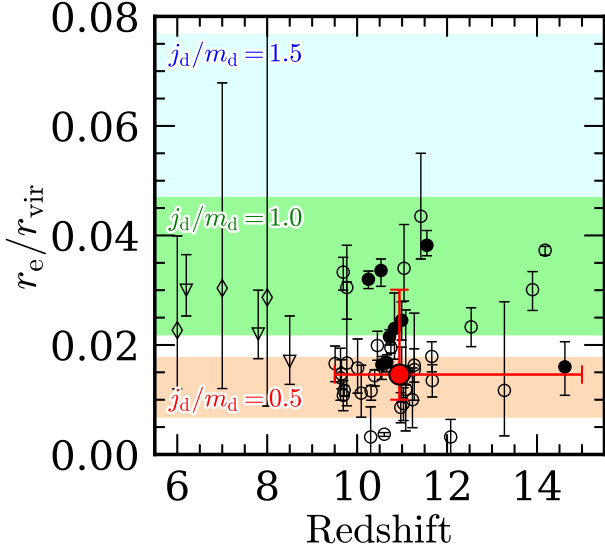


Figure 21. Comparison between the observed galaxy-to-host dark matter halo size ratio and the expected values from the galaxy disk formation model. The black open circles represent the results for relatively luminous $z \sim 10\text{--}16$ galaxies analyzed individually in this study, while the black filled circles show the results for stacked images of fainter $z \sim 10\text{--}16$ galaxies. The red filled circle indicates the median value from this study, along with its 68th percentile range. The data points for lower- z galaxies are the same as those in Figure 20. The red, green, and blue shaded regions represent the ranges of values expected from Equation 7 for specific disk angular momentum fractions of $j_d/m_d = 0.5$, 1.0, and 1.5, respectively, based on the model of Mo et al. (1998).

disks, making it challenging for them to sustain a stable disk structure over long periods, often resulting in clumpy morphologies instead (Kimm et al. 2015; Yajima et al. 2017; Yajima et al. 2023). On the other hand, for compact galaxies at high redshifts, it has been suggested that feedback processes may be less effective, potentially allowing for more efficient star formation (Dekel et al. 2023; Andalman et al. 2024). Our results do not explicitly favor either scenario. However, the fact that the size distribution of $z \sim 10\text{--}16$ galaxies is similar to that of the spin parameter distribution of dark matter halos suggests that the latter scenario might be more plausible. If feedback is indeed less effective in these galaxies, their star formation efficiency could be significantly enhanced. In this context, JWST may be preferentially observing such galaxies with high star formation efficiency. This potential observational bias warrants further investigation in future studies.

In the case that $z \sim 10\text{--}16$ galaxies host disks, a comparison with the galaxy disk formation scenario

allows us to place rough constraints on their specific disk angular momentum fraction (e.g., Kravtsov 2013; Kawamata et al. 2015; Shibuya et al. 2015). Based on the galaxy disk formation model of Mo et al. (1998), the stellar-to-halo size ratio is given by

$$\frac{r_e}{r_{\text{vir}}} = \frac{1.678}{\sqrt{2}} \left(\frac{j_d}{m_d} \lambda \right) \frac{f_R(\lambda, c_{\text{vir}}, m_d, j_d)}{\sqrt{f_c(c_{\text{vir}})}}. \quad (7)$$

Here we adopt $r_e = 1.678 R_d$, where R_d is the scale length of an exponential disk. The parameters m_d and j_d represent the mass fraction and angular momentum fraction of the disk relative to the halo, respectively. The functions $f_c(c_{\text{vir}})$ and $f_R(\lambda, c_{\text{vir}}, m_d, j_d)$ depend on the halo concentration factor c_{vir} , with their functional forms provided in Equation 23 and Equation 29 of Mo et al. (1998), respectively.¹² By adopting the values of the spin parameter λ and c_{vir} obtained from theoretical studies, we can use this comparison to obtain rough constraints on the specific disk angular momentum fraction, j_d/m_d .

Figure 21 compares the observed values of r_e/r_{vir} with the theoretical ranges corresponding to specific disk angular momentum fractions of $j_d/m_d = 0.5$, 1.0, and 1.5. The spin parameter λ is varied within the range of the mean values obtained from theoretical studies, $\lambda = 0.035\text{--}0.045$ (e.g., Bullock et al. 2001; Gardner 2001; van den Bosch et al. 2002; Vitvitska et al. 2002; Bailin & Steinmetz 2005; Davis & Natarajan 2009; Zjupa & Springel 2017), and the halo concentration factor c_{vir} is varied within the range of $c_{\text{vir}} = 3\text{--}5$ following Figure 11 of Ishiyama et al. (2021) (see also, Prada et al. 2012). Additionally, for the mass fraction, we adopt a conservative range of $m_d = 0.05\text{--}0.1$ (Shibuya et al. 2015; see also, Mo et al. 1998). This comparison suggests that the specific disk angular momentum fraction is roughly $j_d/m_d \sim 0.5\text{--}1$. This implies that disk galaxies acquire at least half of their specific angular momentum from their host dark matter halos. As shown in Figure 21, this value is comparable to previous results for lower- z galaxies (Kawamata et al. 2015; Shibuya et al. 2015; Okamura et al. 2018). Moreover, it is also in good agreement with values estimated from kinematic data for nearby disk galaxies ($j_d/m_d \sim 0.6\text{--}1.0$, e.g., Dutton & van den Bosch 2012; Romanowsky & Fall 2012; Fall & Romanowsky 2013; Fall & Romanowsky 2018; see also, Romeo et al. 2023). These results suggest no significant evolution of j_d/m_d even beyond $z = 10$.

¹² For the latter, the actual calculation follows Equation 32 of Mo et al. (1998).

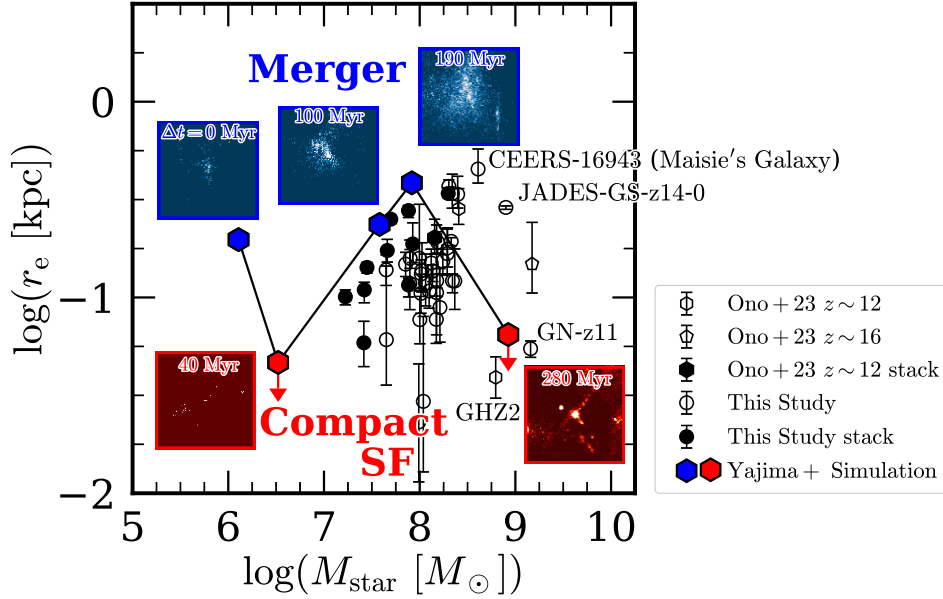


Figure 22. Comparison with theoretical results on the half-light radius vs. stellar mass plane. The black open symbols represent the sizes of relatively luminous $z \sim 10$ – 16 galaxies individually analyzed in this study and our previous work (Ono et al. 2023) and the black filled symbols indicate the results for stacked images of fainter $z \sim 10$ – 16 galaxies. The well-studied objects, GN-z11, GHZ2, JADES-GS-z14-0, and CEERS-16943 (Maisie’s Galaxy) are labeled near their corresponding data points. The filled hexagons represent the evolutionary track of a galaxy with a similar stellar mass and redshift to our galaxies, obtained from cosmological hydrodynamic zoom-in simulations (Yajima et al. 2022; Yajima et al. 2023). For this simulated galaxy, data points with $\log r_e$ (kpc) > -1 are marked in blue, whereas those with $\log r_e$ (kpc) < -1 are in red. The inner images represent 2D projected stellar mass distribution snapshots of the corresponding simulated galaxy, each covering a $1''.5 \times 1''.5$ region, and are color-coded similarly: snapshots with $\log r_e > -1$ are shaded in blue tones, while those with $\log r_e \leq -1$ are in red tones. The time difference in Myr, relative to the starting data point at the top left, is indicated for each snapshot.

5.2. Size Comparisons with Cosmological Zoom-in Simulation Results: Origins of Extended and Extremely Compact Morphologies

As reported in Section 4.1, the sizes of $z \sim 10$ – 16 galaxies exhibit significant diversity, ranging from compact sources smaller than 100 pc to extended ones reaching around 500 pc. As described there, two possible origins have been suggested for the compact galaxies: one possibility is that they host AGNs, and the other is that they undergo compact star formation (e.g., Harikane et al. 2024). Here, we focus on the latter case and explore the origin of this size diversity by comparing our results with those from cosmological zoom-in simulations. This discussion serves as a revised version of the analysis presented in Section 5.3 of Ono et al. (2023), now incorporating the new observational results from this study.

We use the simulation results from the FOREVER22 project (Yajima et al. 2022), which has performed cosmological hydrodynamics zoom-in simulations to investigate the formation and evolution of galaxies within a large comoving volume of $(714 \text{ Mpc})^3$ (see also, Yajima et al. 2023). Among their simulations, we focus

on the highest-resolution run, which has a mass resolution of $\sim 8 \times 10^3 M_\odot$ (first run). We select a galaxy that has a stellar mass comparable to the galaxies analyzed in this study at $z \sim 10$ and extract its 2D projected stellar mass density distributions at four different epochs spanning from an initial redshift of $z = 17$ to approximately 40 Myr to 280 Myr later.

Figure 22 shows the evolution of the half-light radius and stellar mass of the simulated galaxy. The stellar mass of the simulated galaxy increases over time, but its size exhibits both growth and shrinkage at different stages. As explained in Yajima et al. (2023), the simulated galaxy grows through mass accretion including minor mergers, leading to an increase in the size of its stellar components. However, when major mergers occur, the stellar components temporarily appear larger, but as angular momentum is lost, their size rapidly decreases. According to the Illustris simulation results, galaxies typically experience one to two major mergers by $z = 10$ (Rodríguez-Gomez et al. 2015), and at that time, the cosmic age corresponds to several times the dynamical timescale, suggesting that their morphologies are expected to be strongly affected by merger events.

We present our observational results alongside the simulated galaxy in Figure 22. Many of the $z \sim 10\text{--}16$ galaxies exhibit sizes that fall between the compact phase and the relatively extended phase of the simulated galaxy. This suggests that a large fraction of $z \sim 10\text{--}16$ galaxies are either in the process of increasing their size through mass accretion or in the stage of size reduction following a major merger. The particularly extended galaxies, CEERS-16943 (Maisie’s Galaxy) and JADES-GS-z14-0, have sizes comparable to the largest size reached by the simulated galaxy at the snapshots taken in the simulation. This may indicate that CEERS-16943 and JADES-GS-z14-0 are currently undergoing events such as major mergers and/or tidal interactions with surrounding objects. On the other hand, the compact objects GN-z11 and GHZ2 have sizes consistent with those observed in the simulated galaxy when it undergoes significant size shrinkage after a major merger, leading to extremely compact star formation. Such compact phases naturally emerge in cosmological simulations, where major mergers can trigger high-density gas concentrations, resulting in intense star formation within a small region. If GN-z11 and GHZ2 are indeed compact star-forming galaxies, this suggests that they may have just experienced size shrinkage due to a major merger.

These results indicate that mergers play an important role in shaping the diverse sizes of high- z galaxies. While major mergers can significantly alter galaxy structures, either compacting them or temporarily making them appear more extended, gas accretion and feedback processes also contribute to their structural evolution. At high redshifts, the high baryon accretion (including minor mergers) rate ensures a continuous supply of gas with angular momentum comparable to those of the host dark matter halos. Additionally, feedback processes may not be highly effective in these early galaxies due to their high gas densities. This combination of mergers, high accretion rates, and weak feedback could explain why the observed size distribution follows a log-normal distribution with a standard deviation similar to that of the spin parameter of dark matter halos. The observed approximately constant stellar-to-halo size ratios further support the idea that, even in the presence of mergers, the morphological properties of high- z galaxies are regulated by the angular momentum acquired from their dark matter halos. However, these interpretations remain speculative, and further studies are required to fully understand the interplay between mergers, gas accretion, and feedback at high redshifts.

6. SUMMARY

In this study, we have performed morphological analyses for the statistical sample of 169 galaxies at $z \sim 10\text{--}16$ found in the CEERS and JADES surveys, 14 of which have spectroscopic confirmations. Using the deep JWST NIRCcam images, we have conducted surface brightness profile fitting for these galaxies. For the 30 galaxies with aperture magnitudes $S/N > 10$, we have conducted individual analyses, while the remaining galaxies have been stacked to determine their average properties. When allowing the Sérsic index to vary as a free parameter in the profile fitting, the obtained value is $n = 1.3 \pm 0.6$ on average. However, due to the large uncertainty, we have fixed the Sérsic index for the profile fitting, following previous studies. Our main results are as follows:

1. The sizes of the individually analyzed $z \sim 10\text{--}16$ galaxies range from compact sources smaller than 100 pc to larger ones around 500 pc, but are typically in the range of 100–300 pc. Similarly, the sizes of stacked galaxies are also in the range of 100–300 pc. Thus, the typical size of $z \sim 10\text{--}16$ galaxies is 100–300 pc.
2. We have derived the size distribution of $z \sim 10\text{--}16$ galaxies and found that it is well described by a log-normal distribution with a mean of $r_e = 133^{+13}_{-12}$ pc and a standard deviation of $\sigma_{\ln r_e} = 0.52 \pm 0.08$. Compared to previous results, we have found that the standard deviation of the log-normal distribution of galaxy sizes shows no significant evolution even at $z \gtrsim 10$.

We have found that the axis ratio distribution of $z \sim 10\text{--}16$ galaxies appears nearly uniform over $b/a \sim 0.2\text{--}0.8$. A K-S test quantitatively confirms that this distribution is statistically similar to local spiral galaxies, unlike local ellipticals, suggesting that these high- z galaxies may already exhibit disk-like morphologies.

3. Investigating the relation between galaxy size and UV luminosity has revealed that for galaxies brighter than $M_{UV} \lesssim -20$ mag, the sizes span a wide range from large to small. On the other hand, for fainter galaxies, very large sizes are not obtained. Excluding the very compact luminous sources for which the presence of AGNs has been suggested based on previous spectroscopic studies, we have fitted the size–luminosity relation with a power-law function. We have found that the normalization broadly agrees with the trend of decreasing size with increasing redshift reported in previous studies, while the slope is slightly smaller compared to those studies.

4. Combining our results with previous findings, we have fitted the size evolution of galaxies with a power-law function of $r_e \propto (1+z)^s$. For the sample with $L/L_{z=3}^* = 0.3-1$, the slope is consistent with previous results. However, for the sample with $L/L_{z=3}^* = 0.12-0.3$, the slope appears to be slightly steeper.
5. Using the UV luminosities, we have estimated the virial radii of the $z \sim 10-16$ galaxies through the star formation main sequence relation and the stellar mass – halo mass relation. We have then calculated their ratios of galaxy sizes to virial radii, r_e/r_{vir} , and obtained the median value of $r_e/r_{\text{vir}} = 0.015^{+0.015}_{-0.005}$. This value is consistent with those derived for lower- z galaxies within the 1σ ranges, indicating no significant evolution toward $z \gtrsim 10$.
6. Our findings that the size distribution of $z \sim 10-16$ galaxies follows the log-normal distribution with the almost constant standard deviation, which is comparable to the standard deviation of the spin parameter distribution of dark matter halos, that their axis ratio distribution shows a uniform distribution similar to spiral galaxies, that the stellar-to-halo size ratio shows no significant evolution toward $z \gtrsim 10$, and that the mean Sérsic index is around 1.3 albeit with large uncertainties, are all consistent with the classical disk formation scenario. In summary, our results suggest that galaxies at $z \sim 10-16$ possess stellar components that align with the galaxy disk formation scenario.
7. In the case that $z \sim 10-16$ galaxies host disks, a comparison with the galaxy disk formation model suggests that their specific disk angular momentum fraction is approximately $j_d/m_d \sim 0.5-1$, implying that disk galaxies acquire at least half of their specific angular momentum from their host halos. This value is comparable to those for lower- z galaxies including local disk galaxies.
8. Based on comparisons with cosmological simulations, in the case that these galaxies originate from star formation, their diverse sizes likely reflect different evolutionary stages. Extended galaxies like CEERS-16943 (Maisie’s Galaxy) and JADES-GS-

z14-0 may be undergoing mergers or tidal interactions, while very compact objects such as GN-z11 and GHZ2 host compact star formation with sizes consistent with post-merger contraction phases.

ACKNOWLEDGEMENTS

We thank Kentaro Nagamine, Arjen van der Wel, and Kazuhiro Shimasaku for providing insightful comments on our results. We are also grateful to Takatoshi Shibuya for kindly sharing the data files from their previous work. This work is based on observations made with the NASA/ESA/CSA James Webb Space Telescope. The data (Finkelstein et al. 2023a; Rieke et al. 2023a) were obtained from the Mikulski Archive for Space Telescopes at the Space Telescope Science Institute, which is operated by the Association of Universities for Research in Astronomy, Inc., under NASA contract NAS 5-03127 for JWST. These observations are associated with programs ERS-1345 (CEERS), GTO-1180, GTO-1181, GTO-1210, GTO-1286, GO-1895, GO-1963, and GO-3215 (JADES). The authors acknowledge the CEERS team led by Steven L. Finkelstein and the JADES team led by Daniel Eisenstein and Nora Luetzgendorf for developing their observing programs. This work was partially performed using the computer facilities of the Institute for Cosmic Ray Research, The University of Tokyo. This work was supported by the World Premier International Research Center Initiative (WPI Initiative), MEXT, Japan, as well as KAKENHI Grant Numbers 15K17602, 15H02064, 17H01110, 17H01114, 19K14752, 20H00180, 21H04467, 21H04489, 22K03670, and 24H00245 through the Japan Society for the Promotion of Science (JSPS). This work was also supported by JST FOREST Program, Grant Number JP-MJFR202Z. This work was partially supported by the joint research program of the Institute for Cosmic Ray Research (ICRR), University of Tokyo.

Software: GALFIT (Peng et al. 2002; Peng et al. 2010), SExtractor (Bertin & Arnouts 1996), IRAF (Tody 1986, 1993),¹³ SAOImage DS9 (Joye & Mandel 2003), Numpy (Harris et al. 2020), Matplotlib (Hunter 2007), Scipy (Virtanen et al. 2020), Astropy (Astropy Collaboration et al. 2013, 2018),¹⁴ Ned Wright’s Javascript Cosmology Calculator (Wright 2006).¹⁵

¹³ IRAF is distributed by the National Optical Astronomy Observatory, which is operated by the Association of Universities for Research in Astronomy (AURA) under a cooperative agreement with the National Science Foundation.

¹⁴ <http://www.astropy.org>

¹⁵ <http://www.astro.ucla.edu/~wright/CosmoCalc.html>

REFERENCES

- Allen, N., Oesch, P. A., Toft, S., et al. 2024, arXiv e-prints, arXiv:2410.16354, doi: [10.48550/arXiv.2410.16354](https://doi.org/10.48550/arXiv.2410.16354)
- Allen, R. J., Kacprzak, G. G., Glazebrook, K., et al. 2017, ApJ, 834, L11, doi: [10.3847/2041-8213/834/2/L11](https://doi.org/10.3847/2041-8213/834/2/L11)
- Álvarez-Márquez, J., Crespo Gómez, A., Colina, L., et al. 2024, arXiv e-prints, arXiv:2412.12826, <https://arxiv.org/abs/2412.12826>
- Andalman, Z. L., Teyssier, R., & Dekel, A. 2024, arXiv e-prints, arXiv:2410.20530, doi: [10.48550/arXiv.2410.20530](https://doi.org/10.48550/arXiv.2410.20530)
- Astropy Collaboration, Robitaille, T. P., Tollerud, E. J., et al. 2013, A&A, 558, A33, doi: [10.1051/0004-6361/201322068](https://doi.org/10.1051/0004-6361/201322068)
- Astropy Collaboration, Price-Whelan, A. M., Sipőcz, B. M., et al. 2018, AJ, 156, 123, doi: [10.3847/1538-3881/aabc4f](https://doi.org/10.3847/1538-3881/aabc4f)
- Austin, D., Conselice, C. J., Adams, N. J., et al. 2024, arXiv e-prints, arXiv:2404.10751, doi: [10.48550/arXiv.2404.10751](https://doi.org/10.48550/arXiv.2404.10751)
- Baggen, J. F. W., van Dokkum, P., Labbé, I., et al. 2023, ApJ, 955, L12, doi: [10.3847/2041-8213/acf5ef](https://doi.org/10.3847/2041-8213/acf5ef)
- Baggen, J. F. W., van Dokkum, P., Brammer, G., et al. 2024, ApJ, 977, L13, doi: [10.3847/2041-8213/ad90b8](https://doi.org/10.3847/2041-8213/ad90b8)
- Bagley, M. B., Finkelstein, S. L., Koekemoer, A. M., et al. 2023, ApJ, 946, L12, doi: [10.3847/2041-8213/acbb08](https://doi.org/10.3847/2041-8213/acbb08)
- Bailin, J., & Steinmetz, M. 2005, ApJ, 627, 647, doi: [10.1086/430397](https://doi.org/10.1086/430397)
- Barnes, J., & Efstathiou, G. 1987, ApJ, 319, 575, doi: [10.1086/165480](https://doi.org/10.1086/165480)
- Behroozi, P., Wechsler, R. H., Hearin, A. P., & Conroy, C. 2019, MNRAS, 488, 3143, doi: [10.1093/mnras/stz1182](https://doi.org/10.1093/mnras/stz1182)
- Bertin, E., & Arnouts, S. 1996, A&AS, 117, 393, doi: [10.1051/aas:1996164](https://doi.org/10.1051/aas:1996164)
- Bett, P., Eke, V., Frenk, C. S., et al. 2007, MNRAS, 376, 215, doi: [10.1111/j.1365-2966.2007.11432.x](https://doi.org/10.1111/j.1365-2966.2007.11432.x)
- Bouwens, R. J., Illingworth, G. D., Blakeslee, J. P., Broadhurst, T. J., & Franx, M. 2004, ApJ, 611, L1, doi: [10.1086/423786](https://doi.org/10.1086/423786)
- Bouwens, R. J., Illingworth, G. D., Blakeslee, J. P., & Franx, M. 2006, ApJ, 653, 53, doi: [10.1086/498733](https://doi.org/10.1086/498733)
- Bouwens, R. J., Illingworth, G. D., Oesch, P. A., et al. 2017, ApJ, 843, 41, doi: [10.3847/1538-4357/aa74e4](https://doi.org/10.3847/1538-4357/aa74e4)
- Bouwens, R. J., Illingworth, G. D., van Dokkum, P. G., et al. 2022, ApJ, 927, 81, doi: [10.3847/1538-4357/ac4791](https://doi.org/10.3847/1538-4357/ac4791)
- Bouwens, R. J., Illingworth, G. D., Labbe, I., et al. 2011, Nature, 469, 504, doi: [10.1038/nature09717](https://doi.org/10.1038/nature09717)
- Bowler, R. A. A., Dunlop, J. S., McLure, R. J., & McLeod, D. J. 2017, MNRAS, 466, 3612, doi: [10.1093/mnras/stw3296](https://doi.org/10.1093/mnras/stw3296)
- Bridge, J. S., Holwerda, B. W., Stefanon, M., et al. 2019, ApJ, 882, 42, doi: [10.3847/1538-4357/ab3213](https://doi.org/10.3847/1538-4357/ab3213)
- Bruzual, G., & Charlot, S. 2003, MNRAS, 344, 1000, doi: [10.1046/j.1365-8711.2003.06897.x](https://doi.org/10.1046/j.1365-8711.2003.06897.x)
- Bryan, G. L., & Norman, M. L. 1998, ApJ, 495, 80, doi: [10.1086/305262](https://doi.org/10.1086/305262)
- Bullock, J. S., Dekel, A., Kolatt, T. S., et al. 2001, ApJ, 555, 240, doi: [10.1086/321477](https://doi.org/10.1086/321477)
- Bunker, A. J., Saxena, A., Cameron, A. J., et al. 2023, A&A, 677, A88, doi: [10.1051/0004-6361/202346159](https://doi.org/10.1051/0004-6361/202346159)
- Bunker, A. J., Cameron, A. J., Curtis-Lake, E., et al. 2024, A&A, 690, A288, doi: [10.1051/0004-6361/202347094](https://doi.org/10.1051/0004-6361/202347094)
- Calabrò, A., Pentericci, L., Santini, P., et al. 2024a, A&A, 690, A290, doi: [10.1051/0004-6361/202449768](https://doi.org/10.1051/0004-6361/202449768)
- Calabrò, A., Castellano, M., Zavala, J. A., et al. 2024b, ApJ, 975, 245, doi: [10.3847/1538-4357/ad7602](https://doi.org/10.3847/1538-4357/ad7602)
- Carniani, S., Hainline, K., D'Eugenio, F., et al. 2024a, Nature, 633, 318, doi: [10.1038/s41586-024-07860-9](https://doi.org/10.1038/s41586-024-07860-9)
- Carniani, S., D'Eugenio, F., Ji, X., et al. 2024b, arXiv e-prints, arXiv:2409.20533, doi: [10.48550/arXiv.2409.20533](https://doi.org/10.48550/arXiv.2409.20533)
- Castellano, M., Napolitano, L., Fontana, A., et al. 2024, ApJ, 972, 143, doi: [10.3847/1538-4357/ad5f88](https://doi.org/10.3847/1538-4357/ad5f88)
- Chabrier, G. 2003, PASP, 115, 763, doi: [10.1086/376392](https://doi.org/10.1086/376392)
- Clausen, M., Momcheva, I., Whitaker, K. E., et al. 2025, arXiv e-prints, arXiv:2501.04788, doi: [10.48550/arXiv.2501.04788](https://doi.org/10.48550/arXiv.2501.04788)
- Cole, J. W., Papovich, C., Finkelstein, S. L., et al. 2023, arXiv e-prints, arXiv:2312.10152, doi: [10.48550/arXiv.2312.10152](https://doi.org/10.48550/arXiv.2312.10152)
- Conselice, C. J. 2014, ARA&A, 52, 291, doi: [10.1146/annurev-astro-081913-040037](https://doi.org/10.1146/annurev-astro-081913-040037)
- Conselice, C. J., Basham, J. T. F., Bettaney, D. O., et al. 2024, MNRAS, 531, 4857, doi: [10.1093/mnras/stae1180](https://doi.org/10.1093/mnras/stae1180)
- Costantin, L., Pérez-González, P. G., Vega-Ferrero, J., et al. 2023, ApJ, 946, 71, doi: [10.3847/1538-4357/acb926](https://doi.org/10.3847/1538-4357/acb926)
- Cullen, F., McLeod, D. J., McLure, R. J., et al. 2024, MNRAS, 531, 997, doi: [10.1093/mnras/stae1211](https://doi.org/10.1093/mnras/stae1211)
- Curtis-Lake, E., McLure, R. J., Dunlop, J. S., et al. 2016, MNRAS, 457, 440, doi: [10.1093/mnras/stv3017](https://doi.org/10.1093/mnras/stv3017)
- Curtis-Lake, E., Carniani, S., Cameron, A., et al. 2023, Nature Astronomy, 7, 622, doi: [10.1038/s41550-023-01918-w](https://doi.org/10.1038/s41550-023-01918-w)
- Cutler, S. E., Whitaker, K. E., Weaver, J. R., et al. 2024, ApJ, 967, L23, doi: [10.3847/2041-8213/ad464c](https://doi.org/10.3847/2041-8213/ad464c)
- Davis, A. J., & Natarajan, P. 2009, MNRAS, 393, 1498, doi: [10.1111/j.1365-2966.2008.14267.x](https://doi.org/10.1111/j.1365-2966.2008.14267.x)
- de Graaff, A., Rix, H.-W., Carniani, S., et al. 2024, A&A, 684, A87, doi: [10.1051/0004-6361/202347755](https://doi.org/10.1051/0004-6361/202347755)

- Decarli, R., Walter, F., Aravena, M., et al. 2016, *ApJ*, 833, 70, doi: [10.3847/1538-4357/833/1/70](https://doi.org/10.3847/1538-4357/833/1/70)
- DeCoursey, C., Egami, E., Pierel, J. D. R., et al. 2024, arXiv e-prints, arXiv:2406.05060, doi: [10.48550/arXiv.2406.05060](https://doi.org/10.48550/arXiv.2406.05060)
- Dekel, A., Sarkar, K. C., Birnboim, Y., Mandelker, N., & Li, Z. 2023, *MNRAS*, 523, 3201, doi: [10.1093/mnras/stad1557](https://doi.org/10.1093/mnras/stad1557)
- D'Eugenio, F., Cameron, A. J., Scholtz, J., et al. 2024, arXiv e-prints, arXiv:2404.06531, doi: [10.48550/arXiv.2404.06531](https://doi.org/10.48550/arXiv.2404.06531)
- Dutton, A. A., & van den Bosch, F. C. 2012, *MNRAS*, 421, 608, doi: [10.1111/j.1365-2966.2011.20339.x](https://doi.org/10.1111/j.1365-2966.2011.20339.x)
- Eisenstein, D. J., Willott, C., Alberts, S., et al. 2023a, arXiv e-prints, arXiv:2306.02465, doi: [10.48550/arXiv.2306.02465](https://doi.org/10.48550/arXiv.2306.02465)
- Eisenstein, D. J., Johnson, B. D., Robertson, B., et al. 2023b, arXiv e-prints, arXiv:2310.12340, doi: [10.48550/arXiv.2310.12340](https://doi.org/10.48550/arXiv.2310.12340)
- Ellis, R. S., McLure, R. J., Dunlop, J. S., et al. 2013, *ApJ*, 763, L7, doi: [10.1088/2041-8205/763/1/L7](https://doi.org/10.1088/2041-8205/763/1/L7)
- Fall, S. M., & Efstathiou, G. 1980, *MNRAS*, 193, 189, doi: [10.1093/mnras/193.2.189](https://doi.org/10.1093/mnras/193.2.189)
- Fall, S. M., & Romanowsky, A. J. 2013, *ApJ*, 769, L26, doi: [10.1088/2041-8205/769/2/L26](https://doi.org/10.1088/2041-8205/769/2/L26)
- . 2018, *ApJ*, 868, 133, doi: [10.3847/1538-4357/aaeb27](https://doi.org/10.3847/1538-4357/aaeb27)
- Ferguson, H. C., Dickinson, M., Giavalisco, M., et al. 2004, *ApJ*, 600, L107, doi: [10.1086/378578](https://doi.org/10.1086/378578)
- Ferreira, L., Adams, N., Conselice, C. J., et al. 2022, *ApJ*, 938, L2, doi: [10.3847/2041-8213/ac947c](https://doi.org/10.3847/2041-8213/ac947c)
- Ferreira, L., Conselice, C. J., Sazonova, E., et al. 2023, *ApJ*, 955, 94, doi: [10.3847/1538-4357/acec76](https://doi.org/10.3847/1538-4357/acec76)
- Finkelstein, S., Bagley, M., & Yang, G. 2023a, Data from The Cosmic Evolution Early Release Science Survey (CEERS), STScI/MAST, doi: [10.17909/Z7P0-8481](https://doi.org/10.17909/Z7P0-8481)
- Finkelstein, S. L., Bagley, M. B., Arrabal Haro, P., et al. 2022, *ApJ*, 940, L55, doi: [10.3847/2041-8213/ac966e](https://doi.org/10.3847/2041-8213/ac966e)
- Finkelstein, S. L., Bagley, M. B., Ferguson, H. C., et al. 2023b, *ApJ*, 946, L13, doi: [10.3847/2041-8213/acade4](https://doi.org/10.3847/2041-8213/acade4)
- Finkelstein, S. L., Leung, G. C. K., Bagley, M. B., et al. 2024, *ApJ*, 969, L2, doi: [10.3847/2041-8213/ad4495](https://doi.org/10.3847/2041-8213/ad4495)
- Finkelstein, S. L., Bagley, M. B., Arrabal Haro, P., et al. 2025, arXiv e-prints, arXiv:2501.04085, doi: [10.48550/arXiv.2501.04085](https://doi.org/10.48550/arXiv.2501.04085)
- Fraternali, F., Karim, A., Magnelli, B., et al. 2021, *A&A*, 647, A194, doi: [10.1051/0004-6361/202039807](https://doi.org/10.1051/0004-6361/202039807)
- Fujimoto, S., Bezanson, R., Labbe, I., et al. 2023, arXiv e-prints, arXiv:2309.07834, doi: [10.48550/arXiv.2309.07834](https://doi.org/10.48550/arXiv.2309.07834)
- Fujimoto, S., Ouchi, M., Kohno, K., et al. 2024, arXiv e-prints, arXiv:2402.18543, doi: [10.48550/arXiv.2402.18543](https://doi.org/10.48550/arXiv.2402.18543)
- Fukushima, H., & Yajima, H. 2021, *MNRAS*, 506, 5512, doi: [10.1093/mnras/stab2099](https://doi.org/10.1093/mnras/stab2099)
- Fukushima, H., Yajima, H., Sugimura, K., et al. 2020, *MNRAS*, 497, 3830, doi: [10.1093/mnras/staa2062](https://doi.org/10.1093/mnras/staa2062)
- Gardner, J. P. 2001, *ApJ*, 557, 616, doi: [10.1086/321631](https://doi.org/10.1086/321631)
- Gardner, J. P., Mather, J. C., Clampin, M., et al. 2006, *Space Sci. Rev.*, 123, 485, doi: [10.1007/s11214-006-8315-7](https://doi.org/10.1007/s11214-006-8315-7)
- Gardner, J. P., Mather, J. C., Abbott, R., et al. 2023, *PASP*, 135, 068001, doi: [10.1088/1538-3873/acd1b5](https://doi.org/10.1088/1538-3873/acd1b5)
- Géron, T., Smethurst, R. J., Dickinson, H., et al. 2025, *ApJ*, 987, 74, doi: [10.3847/1538-4357/add7d0](https://doi.org/10.3847/1538-4357/add7d0)
- Gillman, S., Gullberg, B., Brammer, G., et al. 2023, *A&A*, 676, A26, doi: [10.1051/0004-6361/202346531](https://doi.org/10.1051/0004-6361/202346531)
- Grazian, A., Castellano, M., Fontana, A., et al. 2012, *A&A*, 547, A51, doi: [10.1051/0004-6361/201219669](https://doi.org/10.1051/0004-6361/201219669)
- Guo, J., Onoue, M., Inayoshi, K., et al. 2024, arXiv e-prints, arXiv:2409.19205, doi: [10.48550/arXiv.2409.19205](https://doi.org/10.48550/arXiv.2409.19205)
- Hainline, K. N., Johnson, B. D., Robertson, B., et al. 2024, *ApJ*, 964, 71, doi: [10.3847/1538-4357/ad1ee4](https://doi.org/10.3847/1538-4357/ad1ee4)
- Harikane, Y., Ouchi, M., Oguri, M., et al. 2023, *ApJS*, 265, 5, doi: [10.3847/1538-4365/aca9a9](https://doi.org/10.3847/1538-4365/aca9a9)
- Harikane, Y., Inoue, A. K., Ellis, R. S., et al. 2024, arXiv e-prints, arXiv:2406.18352, doi: [10.48550/arXiv.2406.18352](https://doi.org/10.48550/arXiv.2406.18352)
- Harris, C. R., Millman, K. J., van der Walt, S. J., et al. 2020, *Nature*, 585, 357, doi: [10.1038/s41586-020-2649-2](https://doi.org/10.1038/s41586-020-2649-2)
- Hathi, N. P., Malhotra, S., & Rhoads, J. E. 2008, *ApJ*, 673, 686, doi: [10.1086/524836](https://doi.org/10.1086/524836)
- Häußler, B., Bamford, S. P., Vika, M., et al. 2013, *MNRAS*, 430, 330, doi: [10.1093/mnras/sts633](https://doi.org/10.1093/mnras/sts633)
- Herrera-Camus, R., Förster Schreiber, N. M., Price, S. H., et al. 2022, *A&A*, 665, L8, doi: [10.1051/0004-6361/202142562](https://doi.org/10.1051/0004-6361/202142562)
- Hodge, J. A., da Cunha, E., Kendrew, S., et al. 2024, arXiv e-prints, arXiv:2407.15846, doi: [10.48550/arXiv.2407.15846](https://doi.org/10.48550/arXiv.2407.15846)
- Hogg, D. W. 1999, arXiv e-prints, astro. <https://arxiv.org/abs/astro-ph/9905116>
- Holwerda, B. W., Bouwens, R., Oesch, P., et al. 2015, *ApJ*, 808, 6, doi: [10.1088/0004-637X/808/1/6](https://doi.org/10.1088/0004-637X/808/1/6)
- Holwerda, B. W., Bridge, J. S., Steele, R. L., et al. 2020, *AJ*, 160, 154, doi: [10.3847/1538-3881/aba617](https://doi.org/10.3847/1538-3881/aba617)
- Holwerda, B. W., Hsu, C.-C., Hathi, N., et al. 2024, *MNRAS*, 529, 1067, doi: [10.1093/mnras/stae316](https://doi.org/10.1093/mnras/stae316)
- Huang, K.-H., Ferguson, H. C., Ravindranath, S., & Su, J. 2013, *ApJ*, 765, 68, doi: [10.1088/0004-637X/765/1/68](https://doi.org/10.1088/0004-637X/765/1/68)

- Huang, K.-H., Fall, S. M., Ferguson, H. C., et al. 2017, *ApJ*, 838, 6, doi: [10.3847/1538-4357/aa62a6](https://doi.org/10.3847/1538-4357/aa62a6)
- Huertas-Company, M., Iyer, K. G., Angeloudi, E., et al. 2024, *A&A*, 685, A48, doi: [10.1051/0004-6361/202346800](https://doi.org/10.1051/0004-6361/202346800)
- Huertas-Company, M., Shuntov, M., Dong, Y., et al. 2025, arXiv e-prints, arXiv:2502.03532. <https://arxiv.org/abs/2502.03532>
- Hunter, J. D. 2007, *Computing in Science and Engineering*, 9, 90, doi: [10.1109/MCSE.2007.55](https://doi.org/10.1109/MCSE.2007.55)
- Ishiyama, T., Prada, F., Klypin, A. A., et al. 2021, *MNRAS*, 506, 4210, doi: [10.1093/mnras/stab1755](https://doi.org/10.1093/mnras/stab1755)
- Ito, K., Valentino, F., Brammer, G., et al. 2024, *ApJ*, 964, 192, doi: [10.3847/1538-4357/ad2512](https://doi.org/10.3847/1538-4357/ad2512)
- Ji, Z., Williams, C. C., Suess, K. A., et al. 2024, arXiv e-prints, arXiv:2401.00934, doi: [10.48550/arXiv.2401.00934](https://doi.org/10.48550/arXiv.2401.00934)
- Jia, C., Wang, E., Wang, H., et al. 2024, arXiv e-prints, arXiv:2411.07458, doi: [10.48550/arXiv.2411.07458](https://doi.org/10.48550/arXiv.2411.07458)
- Jiang, L., Egami, E., Fan, X., et al. 2013, *ApJ*, 773, 153, doi: [10.1088/0004-637X/773/2/153](https://doi.org/10.1088/0004-637X/773/2/153)
- Joye, W. A., & Mandel, E. 2003, in *Astronomical Society of the Pacific Conference Series*, Vol. 295, *Astronomical Data Analysis Software and Systems XII*, ed. H. E. Payne, R. I. Jedrzejewski, & R. N. Hook, 489
- Kartaltepe, J. S., Rose, C., Vanderhoof, B. N., et al. 2023, *ApJ*, 946, L15, doi: [10.3847/2041-8213/acad01](https://doi.org/10.3847/2041-8213/acad01)
- Kawamata, R., Ishigaki, M., Shimasaku, K., Oguri, M., & Ouchi, M. 2015, *ApJ*, 804, 103, doi: [10.1088/0004-637X/804/2/103](https://doi.org/10.1088/0004-637X/804/2/103)
- Kawamata, R., Ishigaki, M., Shimasaku, K., et al. 2018, *ApJ*, 855, 4, doi: [10.3847/1538-4357/aaa6cf](https://doi.org/10.3847/1538-4357/aaa6cf)
- Kennicutt, Jr., R. C. 1998, *ARA&A*, 36, 189, doi: [10.1146/annurev.astro.36.1.189](https://doi.org/10.1146/annurev.astro.36.1.189)
- Kim, J.-G., Kim, W.-T., & Ostriker, E. C. 2018, *ApJ*, 859, 68, doi: [10.3847/1538-4357/aabe27](https://doi.org/10.3847/1538-4357/aabe27)
- Kimm, T., Cen, R., Devriendt, J., Dubois, Y., & Slyz, A. 2015, *MNRAS*, 451, 2900, doi: [10.1093/mnras/stv1211](https://doi.org/10.1093/mnras/stv1211)
- Kocevski, D. D., Finkelstein, S. L., Barro, G., et al. 2024, arXiv e-prints, arXiv:2404.03576, doi: [10.48550/arXiv.2404.03576](https://doi.org/10.48550/arXiv.2404.03576)
- Kokorev, V., Caputi, K. I., Greene, J. E., et al. 2024, *ApJ*, 968, 38, doi: [10.3847/1538-4357/ad4265](https://doi.org/10.3847/1538-4357/ad4265)
- Kravtsov, A. V. 2013, *ApJ*, 764, L31, doi: [10.1088/2041-8205/764/2/L31](https://doi.org/10.1088/2041-8205/764/2/L31)
- LaChance, P., Croft, R., Ni, Y., et al. 2024, arXiv e-prints, arXiv:2401.16608, doi: [10.48550/arXiv.2401.16608](https://doi.org/10.48550/arXiv.2401.16608)
- Lackner, C. N., & Gunn, J. E. 2012, *MNRAS*, 421, 2277, doi: [10.1111/j.1365-2966.2012.20450.x](https://doi.org/10.1111/j.1365-2966.2012.20450.x)
- Laishram, R., Kodama, T., Morishita, T., et al. 2024, *ApJ*, 964, L33, doi: [10.3847/2041-8213/ad3238](https://doi.org/10.3847/2041-8213/ad3238)
- Lambas, D. G., Maddox, S. J., & Loveday, J. 1992, *MNRAS*, 258, 404, doi: [10.1093/mnras/258.2.404](https://doi.org/10.1093/mnras/258.2.404)
- Langeroodi, D., & Hjorth, J. 2023, arXiv e-prints, arXiv:2307.06336, doi: [10.48550/arXiv.2307.06336](https://doi.org/10.48550/arXiv.2307.06336)
- Le Bail, A., Daddi, E., Elbaz, D., et al. 2024, *A&A*, 688, A53, doi: [10.1051/0004-6361/202347465](https://doi.org/10.1051/0004-6361/202347465)
- Lee, J. H., Park, C., Hwang, H. S., & Kwon, M. 2024, *ApJ*, 966, 113, doi: [10.3847/1538-4357/ad3448](https://doi.org/10.3847/1538-4357/ad3448)
- Lelli, F., Di Teodoro, E. M., Fraternali, F., et al. 2021, *Science*, 371, 713, doi: [10.1126/science.abc1893](https://doi.org/10.1126/science.abc1893)
- Li, Z., Cai, Z., Sun, F., et al. 2023, arXiv e-prints, arXiv:2310.09327, doi: [10.48550/arXiv.2310.09327](https://doi.org/10.48550/arXiv.2310.09327)
- Liu, Y., Dai, Y. S., Wuyts, S., Huang, J.-S., & Jiang, L. 2024, *ApJ*, 966, 210, doi: [10.3847/1538-4357/ad3822](https://doi.org/10.3847/1538-4357/ad3822)
- Madau, P., & Dickinson, M. 2014, *ARA&A*, 52, 415, doi: [10.1146/annurev-astro-081811-125615](https://doi.org/10.1146/annurev-astro-081811-125615)
- Maiolino, R., Scholtz, J., Witstok, J., et al. 2024, *Nature*, 627, 59, doi: [10.1038/s41586-024-07052-5](https://doi.org/10.1038/s41586-024-07052-5)
- Martorano, M., van der Wel, A., Baes, M., et al. 2024, *ApJ*, 972, 134, doi: [10.3847/1538-4357/ad5c6a](https://doi.org/10.3847/1538-4357/ad5c6a)
- Martorano, M., van der Wel, A., Bell, E. F., et al. 2023, *ApJ*, 957, 46, doi: [10.3847/1538-4357/acf716](https://doi.org/10.3847/1538-4357/acf716)
- Martorano, M., van der Wel, A., Baes, M., et al. 2025, arXiv e-prints, arXiv:2501.02956. <https://arxiv.org/abs/2501.02956>
- Matthee, J., Naidu, R. P., Brammer, G., et al. 2024, *ApJ*, 963, 129, doi: [10.3847/1538-4357/ad2345](https://doi.org/10.3847/1538-4357/ad2345)
- McElwain, M. W., Feinberg, L. D., Perrin, M. D., et al. 2023, *PASP*, 135, 058001, doi: [10.1088/1538-3873/acada0](https://doi.org/10.1088/1538-3873/acada0)
- Miller, T. B., Suess, K. A., Setton, D. J., et al. 2024, arXiv e-prints, arXiv:2412.06957. <https://arxiv.org/abs/2412.06957>
- Mo, H. J., Mao, S., & White, S. D. M. 1998, *MNRAS*, 295, 319, doi: [10.1046/j.1365-8711.1998.01227.x](https://doi.org/10.1046/j.1365-8711.1998.01227.x)
- Morishita, T., Stiavelli, M., Chary, R.-R., et al. 2024, *ApJ*, 963, 9, doi: [10.3847/1538-4357/ad1404](https://doi.org/10.3847/1538-4357/ad1404)
- Mosleh, M., Williams, R. J., Franx, M., et al. 2012, *ApJ*, 756, L12, doi: [10.1088/2041-8205/756/1/L12](https://doi.org/10.1088/2041-8205/756/1/L12)
- Nadolny, J., Michałowski, M. J., Parente, M., et al. 2025, *A&A*, 693, L6, doi: [10.1051/0004-6361/202452794](https://doi.org/10.1051/0004-6361/202452794)
- Nakane, M., Ouchi, M., Nakajima, K., et al. 2024, *ApJ*, 976, 122, doi: [10.3847/1538-4357/ad84e8](https://doi.org/10.3847/1538-4357/ad84e8)
- Nakazato, Y., Ceverino, D., & Yoshida, N. 2024, *ApJ*, 975, 238, doi: [10.3847/1538-4357/ad7d0b](https://doi.org/10.3847/1538-4357/ad7d0b)
- Neeleman, M., Prochaska, J. X., Kanekar, N., & Rafelski, M. 2020, *Nature*, 581, 269, doi: [10.1038/s41586-020-2276-y](https://doi.org/10.1038/s41586-020-2276-y)
- Neeleman, M., Walter, F., Decarli, R., et al. 2023, *ApJ*, 958, 132, doi: [10.3847/1538-4357/ad05d2](https://doi.org/10.3847/1538-4357/ad05d2)

- Neeleman, M., Novak, M., Venemans, B. P., et al. 2021, *ApJ*, 911, 141, doi: [10.3847/1538-4357/abe70f](https://doi.org/10.3847/1538-4357/abe70f)
- Nelson, E., Brammer, G., Giménez-Arteaga, C., et al. 2024, *ApJ*, 976, L27, doi: [10.3847/2041-8213/ad7b17](https://doi.org/10.3847/2041-8213/ad7b17)
- Newman, A. B., Ellis, R. S., Bundy, K., & Treu, T. 2012, *ApJ*, 746, 162, doi: [10.1088/0004-637X/746/2/162](https://doi.org/10.1088/0004-637X/746/2/162)
- Ning, Y., Cai, Z., Lin, X., et al. 2024, *ApJ*, 963, L38, doi: [10.3847/2041-8213/ad292f](https://doi.org/10.3847/2041-8213/ad292f)
- Oesch, P. A., Bouwens, R. J., Carollo, C. M., et al. 2010, *ApJ*, 709, L21, doi: [10.1088/2041-8205/709/1/L21](https://doi.org/10.1088/2041-8205/709/1/L21)
- Oesch, P. A., Brammer, G., van Dokkum, P. G., et al. 2016, *ApJ*, 819, 129, doi: [10.3847/0004-637X/819/2/129](https://doi.org/10.3847/0004-637X/819/2/129)
- Okamura, T., Shimasaku, K., & Kawamata, R. 2018, *ApJ*, 854, 22, doi: [10.3847/1538-4357/aaa423](https://doi.org/10.3847/1538-4357/aaa423)
- Oke, J. B., & Gunn, J. E. 1983, *ApJ*, 266, 713, doi: [10.1086/160817](https://doi.org/10.1086/160817)
- Ono, Y., Ouchi, M., Curtis-Lake, E., et al. 2013, *ApJ*, 777, 155, doi: [10.1088/0004-637X/777/2/155](https://doi.org/10.1088/0004-637X/777/2/155)
- Ono, Y., Harikane, Y., Ouchi, M., et al. 2023, *ApJ*, 951, 72, doi: [10.3847/1538-4357/acd44a](https://doi.org/10.3847/1538-4357/acd44a)
- . 2024, *PASJ*, 76, 219, doi: [10.1093/pasj/psae004](https://doi.org/10.1093/pasj/psae004)
- Ormerod, K., Conselice, C. J., Adams, N. J., et al. 2024, *MNRAS*, 527, 6110, doi: [10.1093/mnras/stad3597](https://doi.org/10.1093/mnras/stad3597)
- Parlanti, E., Carniani, S., Pallottini, A., et al. 2023, *A&A*, 673, A153, doi: [10.1051/0004-6361/202245603](https://doi.org/10.1051/0004-6361/202245603)
- Peng, C. Y., Ho, L. C., Impey, C. D., & Rix, H.-W. 2002, *AJ*, 124, 266, doi: [10.1086/340952](https://doi.org/10.1086/340952)
- . 2010, *AJ*, 139, 2097, doi: [10.1088/0004-6256/139/6/2097](https://doi.org/10.1088/0004-6256/139/6/2097)
- Pérez-González, P. G., Barro, G., Rieke, G. H., et al. 2024, *ApJ*, 968, 4, doi: [10.3847/1538-4357/ad38bb](https://doi.org/10.3847/1538-4357/ad38bb)
- Planck Collaboration, Aghanim, N., Akrami, Y., et al. 2020, *A&A*, 641, A6, doi: [10.1051/0004-6361/201833910](https://doi.org/10.1051/0004-6361/201833910)
- Posses, A. C., Aravena, M., González-López, J., et al. 2023, *A&A*, 669, A46, doi: [10.1051/0004-6361/202243399](https://doi.org/10.1051/0004-6361/202243399)
- Prada, F., Klypin, A. A., Cuesta, A. J., Betancort-Rijo, J. E., & Primack, J. 2012, *MNRAS*, 423, 3018, doi: [10.1111/j.1365-2966.2012.21007.x](https://doi.org/10.1111/j.1365-2966.2012.21007.x)
- Ravindranath, S., Giavalisco, M., Ferguson, H. C., et al. 2006, *ApJ*, 652, 963, doi: [10.1086/507016](https://doi.org/10.1086/507016)
- Rieke, M., Robertson, B., Tacchella, S., et al. 2023a, Data from the JWST Advanced Deep Extragalactic Survey (JADES), STScI/MAST, doi: [10.17909/8TDJ-8N28](https://doi.org/10.17909/8TDJ-8N28)
- Rieke, M. J., Kelly, D., & Horner, S. 2005, in *Society of Photo-Optical Instrumentation Engineers (SPIE) Conference Series*, Vol. 5904, *Cryogenic Optical Systems and Instruments XI*, ed. J. B. Heaney & L. G. Burriesci, 1–8, doi: [10.1117/12.615554](https://doi.org/10.1117/12.615554)
- Rieke, M. J., Kelly, D. M., Misselt, K., et al. 2023b, *PASP*, 135, 028001, doi: [10.1088/1538-3873/acac53](https://doi.org/10.1088/1538-3873/acac53)
- Rieke, M. J., Robertson, B., Tacchella, S., et al. 2023c, *ApJS*, 269, 16, doi: [10.3847/1538-4365/acf44d](https://doi.org/10.3847/1538-4365/acf44d)
- Rinaldi, P., Bonaventura, N., Rieke, G. H., et al. 2024, *arXiv e-prints*, arXiv:2411.14383, doi: [10.48550/arXiv.2411.14383](https://doi.org/10.48550/arXiv.2411.14383)
- Rizzo, F., Kohandel, M., Pallottini, A., et al. 2022, *A&A*, 667, A5, doi: [10.1051/0004-6361/202243582](https://doi.org/10.1051/0004-6361/202243582)
- Rizzo, F., Vegetti, S., Powell, D., et al. 2020, *Nature*, 584, 201, doi: [10.1038/s41586-020-2572-6](https://doi.org/10.1038/s41586-020-2572-6)
- Roberts-Borsani, G., Treu, T., Shapley, A., et al. 2024, *ApJ*, 976, 193, doi: [10.3847/1538-4357/ad85d3](https://doi.org/10.3847/1538-4357/ad85d3)
- Robertson, B. E., Tacchella, S., Johnson, B. D., et al. 2023, *ApJ*, 942, L42, doi: [10.3847/2041-8213/aca086](https://doi.org/10.3847/2041-8213/aca086)
- Rodriguez-Gomez, V., Genel, S., Vogelsberger, M., et al. 2015, *MNRAS*, 449, 49, doi: [10.1093/mnras/stv264](https://doi.org/10.1093/mnras/stv264)
- Rodriguez-Gomez, V., Snyder, G. F., Lotz, J. M., et al. 2019, *MNRAS*, 483, 4140, doi: [10.1093/mnras/sty3345](https://doi.org/10.1093/mnras/sty3345)
- Roman-Oliveira, F., Fraternali, F., & Rizzo, F. 2023, *MNRAS*, 521, 1045, doi: [10.1093/mnras/stad530](https://doi.org/10.1093/mnras/stad530)
- Romanowsky, A. J., & Fall, S. M. 2012, *ApJS*, 203, 17, doi: [10.1088/0067-0049/203/2/17](https://doi.org/10.1088/0067-0049/203/2/17)
- Romeo, A. B., Agertz, O., & Renaud, F. 2023, *MNRAS*, 518, 1002, doi: [10.1093/mnras/stac3074](https://doi.org/10.1093/mnras/stac3074)
- Rowland, L. E., Hodge, J., Bouwens, R., et al. 2024, *MNRAS*, 535, 2068, doi: [10.1093/mnras/stae2217](https://doi.org/10.1093/mnras/stae2217)
- Salpeter, E. E. 1955, *ApJ*, 121, 161, doi: [10.1086/145971](https://doi.org/10.1086/145971)
- Salucci, P., Lapi, A., Tonini, C., et al. 2007, *MNRAS*, 378, 41, doi: [10.1111/j.1365-2966.2007.11696.x](https://doi.org/10.1111/j.1365-2966.2007.11696.x)
- Saxena, A., Cameron, A. J., Katz, H., et al. 2024, *arXiv e-prints*, arXiv:2411.14532, doi: [10.48550/arXiv.2411.14532](https://doi.org/10.48550/arXiv.2411.14532)
- Schouws, S., Bouwens, R. J., Ormerod, K., et al. 2024, *arXiv e-prints*, arXiv:2409.20549, doi: [10.48550/arXiv.2409.20549](https://doi.org/10.48550/arXiv.2409.20549)
- Senchyna, P., Plat, A., Stark, D. P., et al. 2024, *ApJ*, 966, 92, doi: [10.3847/1538-4357/ad235e](https://doi.org/10.3847/1538-4357/ad235e)
- Sersic, J. L. 1968, *Atlas de Galaxias Australes*
- Shen, S., Mo, H. J., White, S. D. M., et al. 2003, *MNRAS*, 343, 978, doi: [10.1046/j.1365-8711.2003.06740.x](https://doi.org/10.1046/j.1365-8711.2003.06740.x)
- Shen, X., Borrow, J., Vogelsberger, M., et al. 2024a, *MNRAS*, 527, 2835, doi: [10.1093/mnras/stad3397](https://doi.org/10.1093/mnras/stad3397)
- Shen, X., Vogelsberger, M., Borrow, J., et al. 2024b, *MNRAS*, 534, 1433, doi: [10.1093/mnras/stae2156](https://doi.org/10.1093/mnras/stae2156)
- Shibuya, T., Ouchi, M., & Harikane, Y. 2015, *ApJS*, 219, 15, doi: [10.1088/0067-0049/219/2/15](https://doi.org/10.1088/0067-0049/219/2/15)
- Smethurst, R. J., Simmons, B. D., Géron, T., et al. 2025, *MNRAS*, 539, 1359, doi: [10.1093/mnras/staf506](https://doi.org/10.1093/mnras/staf506)
- Smit, R., Bouwens, R. J., Carniani, S., et al. 2018, *Nature*, 553, 178, doi: [10.1038/nature24631](https://doi.org/10.1038/nature24631)

- Stark, D. P., Topping, M. W., Endsley, R., & Tang, M. 2025, arXiv e-prints, arXiv:2501.17078, doi: [10.48550/arXiv.2501.17078](https://doi.org/10.48550/arXiv.2501.17078)
- Steidel, C. C., Adelberger, K. L., Giavalisco, M., Dickinson, M., & Pettini, M. 1999, *ApJ*, 519, 1, doi: [10.1086/307363](https://doi.org/10.1086/307363)
- Steinmetz, M., & Bartelmann, M. 1995, *MNRAS*, 272, 570, doi: [10.1093/mnras/272.3.570](https://doi.org/10.1093/mnras/272.3.570)
- Suess, K. A., Bezanson, R., Nelson, E. J., et al. 2022, *ApJ*, 937, L33, doi: [10.3847/2041-8213/ac8e06](https://doi.org/10.3847/2041-8213/ac8e06)
- Sun, W., Ho, L. C., Zhuang, M.-Y., et al. 2024, *ApJ*, 960, 104, doi: [10.3847/1538-4357/acf1f6](https://doi.org/10.3847/1538-4357/acf1f6)
- Tacchella, S., Eisenstein, D. J., Hainline, K., et al. 2023, *ApJ*, 952, 74, doi: [10.3847/1538-4357/acdbcf](https://doi.org/10.3847/1538-4357/acdbcf)
- Tacconi, L. J., Neri, R., Genzel, R., et al. 2013, *ApJ*, 768, 74, doi: [10.1088/0004-637X/768/1/74](https://doi.org/10.1088/0004-637X/768/1/74)
- Tody, D. 1986, in *Society of Photo-Optical Instrumentation Engineers (SPIE) Conference Series*, Vol. 627, *Instrumentation in astronomy VI*, ed. D. L. Crawford, 733, doi: [10.1117/12.968154](https://doi.org/10.1117/12.968154)
- Tody, D. 1993, in *Astronomical Society of the Pacific Conference Series*, Vol. 52, *Astronomical Data Analysis Software and Systems II*, ed. R. J. Hanisch, R. J. V. Brissenden, & J. Barnes, 173
- Tohill, C., Bamford, S. P., Conselice, C. J., et al. 2024, *ApJ*, 962, 164, doi: [10.3847/1538-4357/ad17b8](https://doi.org/10.3847/1538-4357/ad17b8)
- Tokuoka, T., Inoue, A. K., Hashimoto, T., et al. 2022, *ApJ*, 933, L19, doi: [10.3847/2041-8213/ac7447](https://doi.org/10.3847/2041-8213/ac7447)
- Topping, M. W., Stark, D. P., Endsley, R., et al. 2024, *MNRAS*, 529, 4087, doi: [10.1093/mnras/stae800](https://doi.org/10.1093/mnras/stae800)
- Treu, T., Calabrò, A., Castellano, M., et al. 2023, *ApJ*, 942, L28, doi: [10.3847/2041-8213/ac9283](https://doi.org/10.3847/2041-8213/ac9283)
- Tsukui, T., & Iguchi, S. 2021, *Science*, 372, 1201, doi: [10.1126/science.abe9680](https://doi.org/10.1126/science.abe9680)
- Umehata, H., Kubo, M., Smail, I., et al. 2025, arXiv e-prints, arXiv:2502.01868, <https://arxiv.org/abs/2502.01868>
- van den Bosch, F. C., Abel, T., Croft, R. A. C., Hernquist, L., & White, S. D. M. 2002, *ApJ*, 576, 21, doi: [10.1086/341619](https://doi.org/10.1086/341619)
- van der Wel, A., Franx, M., van Dokkum, P. G., et al. 2014, *ApJ*, 788, 28, doi: [10.1088/0004-637X/788/1/28](https://doi.org/10.1088/0004-637X/788/1/28)
- van der Wel, A., Martorano, M., Häußler, B., et al. 2024, *ApJ*, 960, 53, doi: [10.3847/1538-4357/ad02ee](https://doi.org/10.3847/1538-4357/ad02ee)
- Varadaraj, R. G., Bowler, R. A. A., Jarvis, M. J., et al. 2024, *MNRAS*, 533, 3724, doi: [10.1093/mnras/stae2022](https://doi.org/10.1093/mnras/stae2022)
- Vega-Ferrero, J., Huertas-Company, M., Costantin, L., et al. 2024, *ApJ*, 961, 51, doi: [10.3847/1538-4357/ad05bb](https://doi.org/10.3847/1538-4357/ad05bb)
- Virtanen, P., Gommers, R., Oliphant, T. E., et al. 2020, *Nature Methods*, 17, 261, doi: [10.1038/s41592-019-0686-2](https://doi.org/10.1038/s41592-019-0686-2)
- Vitvitska, M., Klypin, A. A., Kravtsov, A. V., et al. 2002, *ApJ*, 581, 799, doi: [10.1086/344361](https://doi.org/10.1086/344361)
- Wang, F., Yang, J., Fan, X., et al. 2024, *ApJ*, 968, 9, doi: [10.3847/1538-4357/ad3fb4](https://doi.org/10.3847/1538-4357/ad3fb4)
- Ward, E., de la Vega, A., Mobasher, B., et al. 2024, *ApJ*, 962, 176, doi: [10.3847/1538-4357/ad20ed](https://doi.org/10.3847/1538-4357/ad20ed)
- Warren, M. S., Quinn, P. J., Salmon, J. K., & Zurek, W. H. 1992, *ApJ*, 399, 405, doi: [10.1086/171937](https://doi.org/10.1086/171937)
- Weiß, A., De Breuck, C., Marrone, D. P., et al. 2013, *ApJ*, 767, 88, doi: [10.1088/0004-637X/767/1/88](https://doi.org/10.1088/0004-637X/767/1/88)
- Westcott, L., Conselice, C. J., Harvey, T., et al. 2024, arXiv e-prints, arXiv:2412.14970, <https://arxiv.org/abs/2412.14970>
- White, S. D. M. 1984, *ApJ*, 286, 38, doi: [10.1086/162573](https://doi.org/10.1086/162573)
- Wright, E. L. 2006, *PASP*, 118, 1711, doi: [10.1086/510102](https://doi.org/10.1086/510102)
- Wright, L., Whitaker, K. E., Weaver, J. R., et al. 2024, *ApJ*, 964, L10, doi: [10.3847/2041-8213/ad2b6d](https://doi.org/10.3847/2041-8213/ad2b6d)
- Xu, Y., Ouchi, M., Yajima, H., et al. 2024, *ApJ*, 976, 142, doi: [10.3847/1538-4357/ad82dd](https://doi.org/10.3847/1538-4357/ad82dd)
- Yajima, H., Abe, M., Fukushima, H., et al. 2023, *MNRAS*, 525, 4832, doi: [10.1093/mnras/stad2497](https://doi.org/10.1093/mnras/stad2497)
- Yajima, H., Nagamine, K., Zhu, Q., Khochfar, S., & Dalla Vecchia, C. 2017, *ApJ*, 846, 30, doi: [10.3847/1538-4357/aa82b5](https://doi.org/10.3847/1538-4357/aa82b5)
- Yajima, H., Abe, M., Khochfar, S., et al. 2022, *MNRAS*, 509, 4037, doi: [10.1093/mnras/stab3092](https://doi.org/10.1093/mnras/stab3092)
- Yanagisawa, H., Ouchi, M., Nakajima, K., et al. 2024, arXiv e-prints, arXiv:2411.19893, <https://arxiv.org/abs/2411.19893>
- Yang, L., Morishita, T., Leethochawalit, N., et al. 2022, *ApJ*, 938, L17, doi: [10.3847/2041-8213/ac8803](https://doi.org/10.3847/2041-8213/ac8803)
- Yang, L., Kartaltepe, J. S., Franco, M., et al. 2025, arXiv e-prints, arXiv:2504.07185, doi: [10.48550/arXiv.2504.07185](https://doi.org/10.48550/arXiv.2504.07185)
- Yao, Y., Song, J., Kong, X., et al. 2023, *ApJ*, 954, 113, doi: [10.3847/1538-4357/ace7b5](https://doi.org/10.3847/1538-4357/ace7b5)
- Yue, M., Yang, J., Fan, X., et al. 2021, *ApJ*, 917, 99, doi: [10.3847/1538-4357/ac0af4](https://doi.org/10.3847/1538-4357/ac0af4)
- Zavala, J. A., Castellano, M., Akins, H. B., et al. 2024a, *Nature Astronomy*, doi: [10.1038/s41550-024-02397-3](https://doi.org/10.1038/s41550-024-02397-3)
- Zavala, J. A., Bakx, T., Mitsunashi, I., et al. 2024b, *ApJ*, 977, L9, doi: [10.3847/2041-8213/ad8f38](https://doi.org/10.3847/2041-8213/ad8f38)
- Zjupa, J., & Springel, V. 2017, *MNRAS*, 466, 1625, doi: [10.1093/mnras/stw2945](https://doi.org/10.1093/mnras/stw2945)

APPENDIX

A. $z \sim 10$ –16 GALAXY CATALOGS IN THE CEERS AND JADES FIELDS USED IN OUR SIZE MEASUREMENTS

In Section 2, we have compiled $z \sim 10$ –16 galaxies from the high- z galaxy catalogs of CEERS and JADES (Finkelstein et al. 2024; Hainline et al. 2024; Carniani et al. 2024a; Schouws et al. 2024; Carniani et al. 2024b). Table A.1 summarizes the IDs, coordinates, redshifts, and UV magnitudes of objects in the CEERS field, while Table A.2 provides the same information for the JADES fields. Since the decision to perform size measurements individually is based on whether the S/N of the aperture magnitudes exceeded 10, the aperture magnitudes measured by SExtractor (Bertin & Arnouts 1996) are also included. Among these, two objects in CEERS and one object in JADES are included in the little red dots catalog of Kocevski et al. (2024). For these objects, we mark them with a dagger symbol and list their IDs in the table notes. Figure A.1 presents the pseudo-color images of the $z \sim 10$ –16 galaxies analyzed in this study, for which the S/Ns of the aperture magnitude are larger than 10 and the surface brightness profile fitting has been successfully performed with GALFIT.

Table A.1. $z > 9.5$ Galaxies in the CEERS Fields Used in Our Size Analysis

ID	R.A.	Decl.	field	z_{photo}	z_{spec}	$m_{\text{UV}}^{(\text{ap})}$	M_{UV}
	(deg)	(deg)				(mag)	(mag)
(1)	(2)	(3)	(4)	(5)	(6)	(7)	(8)
$L/L_{z=3}^* = 0.3$ –1							
CEERS-87379	214.932064	52.841873	C9	$11.08^{+0.24}_{-0.48}$	Nz	28.56	−20.7
CEERS-99715	214.811852	52.737110	C10	$9.76^{+0.60}_{-0.09}$	$9.77^{+0.37}_{-0.29}$	28.26	−20.5
CEERS-85546	214.885963	52.819060	C9	$11.08^{+0.24}_{-0.60}$	—	28.41	−20.3
CEERS-35590	214.732525	52.758090	C4	$10.15^{+0.36}_{-0.42}$	$10.01^{+0.14}_{-0.19}$	28.12	−20.2
CEERS-16943	214.943152	52.942442	C2	$11.08^{+0.39}_{-0.36}$	$11.416^{+0.005}_{-0.005}$	28.41	−20.2
CEERS-2067	215.010026	53.013641	C1	$12.70^{+0.09}_{-0.72}$	Nz	28.87	−20.1
CEERS-77367	214.989018	52.879278	C8	$10.84^{+0.54}_{-0.51}$	—	28.91	−20.0
CEERS-11384	214.906640	52.945504	C2	$11.53^{+0.30}_{-0.30}$	$11.043^{+0.003}_{-0.003}$	28.67	−20.0
CEERS-98518 ^{†1}	214.817113	52.748343	C10	$10.09^{+0.18}_{-0.39}$	—	27.83	−19.9
CEERS-36796	214.727248	52.748045	C4	$12.28^{+1.59}_{-0.24}$	—	29.04	−19.9
CEERS-26112	214.818999	52.865299	C3	$11.38^{+0.30}_{-0.81}$	—	29.57	−19.9
$L/L_{z=3}^* = 0.12$ –0.3							
CEERS-70831	215.100921	52.936270	C7	$12.07^{+1.98}_{-1.08}$	—	29.50	−19.6
CEERS-101746	214.881212	52.772963	C10	$10.33^{+0.24}_{-0.72}$	—	28.83	−19.6
CEERS-10332	215.044001	52.994302	C1	$10.57^{+0.18}_{-1.05}$	Nz	28.58	−19.5
CEERS-34685	214.700083	52.752419	C4	$11.53^{+0.51}_{-0.72}$	—	29.02	−19.4
CEERS-13452	214.861602	52.904604	C2	$9.55^{+0.78}_{-0.09}$	Nz	29.07	−19.4
CEERS-57400	214.869658	52.843646	C6	$10.60^{+0.60}_{-0.66}$	Nz	28.58	−19.4
CEERS-54306	214.858815	52.850712	C6	$11.23^{+0.36}_{-0.36}$	—	28.40	−19.3
CEERS-74300	214.969256	52.882119	C8	$10.51^{+0.30}_{-0.57}$	—	99.99	−19.3
CEERS-19996	214.922787	52.911529	C2	$11.32^{+0.30}_{-0.90}$	$10.10^{+0.13}_{-0.26}$	29.08	−19.3
CEERS-76686	214.976311	52.873417	C8	$11.11^{+0.33}_{-0.36}$	—	28.76	−19.2
CEERS-16984	214.866488	52.887854	C2	$10.63^{+0.39}_{-0.24}$	—	29.06	−19.2
CEERS-76575	215.015299	52.913706	C8	$9.55^{+0.33}_{-0.06}$	—	28.56	−19.1
CEERS-34925	214.738486	52.765665	C4	$11.89^{+1.92}_{-1.68}$	—	29.67	−19.0
CEERS-77647	215.054220	52.923839	C8	$12.70^{+0.09}_{-0.66}$	—	29.11	−18.9
CEERS-92463 ^{†2}	214.975831	52.841961	C9	$10.51^{+0.69}_{-0.60}$	—	29.47	−18.8

NOTE— The values presented in this table have been obtained in [Finkelstein et al. \(2024\)](#), except for the 4th column and 7th column. (1) Object ID. (2) Right ascension. (3) Declination. (4) Field flag. C_i indicates that the object is located in the CEERS i region. (5) Photometric redshift. (6) Spectroscopic redshift. Nz indicates that the object has been observed spectroscopically but its redshift is not determined. (7) Aperture magnitude in F200W measured in a $0''.2$ diameter circular aperture. (8) Total absolute UV magnitude.

^{†1} CEERS 23931 ([Kocevski et al. 2024](#)).

^{†2} CEERS 36308 ([Kocevski et al. 2024](#)).

Table A.2. $z > 9.5$ Galaxies in the JADES Fields Used in Our Size Analysis

ID	R.A.	Decl.	field	z_{photo}	z_{spec}	$m_{\text{UV}}^{(\text{ap})}$	M_{UV}
	(deg)	(deg)				(mag)	(mag)
(1)	(2)	(3)	(4)	(5)	(6)	(7)	(8)
$L/L_{z=3}^* > 1$							
JADES-GN-189.10604+62.24204	189.106043	62.242045	JN	11.0	10.603	26.45	−22.02
$L/L_{z=3}^* = 0.3\text{--}1$							
JADES-GS-z14-0	53.082937	−27.855629	JS	—	$14.1793^{+0.0007}_{-0.0007}$	28.14	−20.81
JADES-GS-53.13918-27.84849	53.139176	−27.84849	JSm	10.45	—	28.64	−20.40
JADES-GN-189.28497+62.22039	189.284974	62.220395	JN	11.4	—	29.20	−20.38
JADES-GS-53.05511-27.84555	53.055107	−27.845547	JSm	9.65	—	28.41	−20.36
JADES-GN-189.21769+62.19949	189.217687	62.199492	JN	10.31	—	28.11	−20.15
JADES-GS-53.06683-27.87294	53.066830	−27.872939	JSm	10.64	—	28.02	−20.13
JADES-GS-53.07597-27.80654	53.075972	−27.806544	JSm	11.27	—	28.70	−20.08
JADES-GN-189.26202+62.20109	189.262023	62.201085	JN	9.69	—	28.81	−20.08
JADES-GS-53.17551-27.78064	53.175513	−27.780641	JS	9.66	9.712	28.31	−20.00
JADES-GN-189.26284+62.23415	189.262835	62.234150	JN	9.65	—	28.98	−19.99
JADES-GS-53.06131-27.90656	53.061314	−27.906563	JSm	11.21	—	29.12	−19.94
JADES-GS-53.1216-27.90813	53.121605	−27.908134	JSm	11.66	—	28.55	−19.88
JADES-GN-189.28903+62.22905	189.289034	62.229046	JN	10.39	—	28.53	−19.82
JADES-GN-189.27641+62.20724	189.276408	62.207237	JN	12.19	—	29.20	−19.82
JADES-GN-189.26804+62.15158	189.268037	62.151578	JN	10.99	—	28.80	−19.75
JADES-GS-53.16476-27.77463	53.164762	−27.774626	JS	12.31	11.671	28.79	−19.74
$L/L_{z=3}^* = 0.12\text{--}0.3$							
JADES-GS-53.16594-27.83424	53.165936	−27.834236	JS	10.75	—	28.46	−19.61
JADES-GS-53.10798-27.8776	53.107985	−27.877602	JSm	10.97	—	28.42	−19.55
JADES-GS-53.07076-27.86544	53.070763	−27.865438	JSm	11.03	—	28.71	−19.49
JADES-GN-189.2887+62.22923	189.288700	62.229233	JN	10.83	—	29.58	−19.49
JADES-GS-53.16736-27.80751	53.167357	−27.807508	JS	9.54	9.691	28.56	−19.48
JADES-GN-189.25354+62.19416	189.253536	62.194165	JN	9.63	—	28.58	−19.48
JADES-GN-189.30296+62.21075	189.302960	62.210749	JN	10.3	—	28.53	−19.47
JADES-GN-189.25361+62.18821	189.253611	62.188207	JN	9.96	—	29.32	−19.45
JADES-GS-53.06422-27.8932	53.064224	−27.8932	JSm	9.73	—	29.45	−19.45
JADES-GN-189.18021+62.1804	189.180211	62.180405	JN	10.76	—	99.99	−19.37
JADES-GS-53.14528-27.82359	53.145281	−27.823595	JS	10.81	—	29.42	−19.36
JADES-GN-189.2619+62.2012	189.261902	62.201201	JN	11.05	—	29.66	−19.36
JADES-GN-189.25115+62.18742	189.251150	62.187420	JN	10.45	—	29.32	−19.35
JADES-GS-53.13142-27.84713	53.131424	−27.847134	JSm	10.25	—	29.67	−19.32
JADES-GN-189.2234+62.19885	189.223400	62.198847	JN	10.64	—	30.54	−19.29
JADES-GS-53.14297-27.84042	53.142965	−27.840424	JSm	10.24	—	29.75	−19.28
JADES-GS-53.06715-27.88317	53.067152	−27.883171	JSm	10.95	—	30.01	−19.27

Table A.2 *continued*

Table A.2 (*continued*)

ID	R.A.	Decl.	field	z_{photo}	z_{spec}	$m_{\text{UV}}^{(\text{ap})}$	M_{UV}
	(deg)	(deg)				(mag)	(mag)
(1)	(2)	(3)	(4)	(5)	(6)	(7)	(8)
JADES-GS-53.13269-27.84466	53.132690	−27.84466	JSm	10.68	—	99.99	−19.23
JADES-GN-189.24008+62.21415	189.240084	62.214146	JN	10.58	—	29.24	−19.21
JADES-GN-189.28011+62.15677	189.280110	62.156770	JN	9.91	—	29.29	−19.18
JADES-GS-53.11763-27.88818	53.117627	−27.888176	JSm	11.47	—	28.68	−19.17
JADES-GS-53.19051-27.74982	53.190505	−27.749824	JS	12.08	—	28.84	−19.15
JADES-GS-53.06708-27.80877	53.067076	−27.808773	JS	11.53	—	29.16	−19.14
JADES-GS-53.06699-27.80884	53.066989	−27.808839	JS	11.1	—	29.39	−19.11
JADES-GN-189.22085+62.22288	189.220850	62.222879	JN	10.22	—	29.23	−19.04
JADES-GS-53.18993-27.77149	53.189927	−27.771494	JS	11.48	—	29.81	−19.03
JADES-GS-z14-1	53.074271	−27.885927	JS	—	$13.90^{+0.17}_{-0.17}$	29.77	−19.0
JADES-GS-53.16635-27.82156	53.166346	−27.821557	JS	12.46	12.535	29.42	−18.99
JADES-GN-189.24382+62.24059	189.243820	62.240593	JN	10.51	—	29.05	−18.99
JADES-GN-189.27993+62.21553	189.279929	62.215533	JN	11.99	—	29.75	−18.98
JADES-GS-53.19592-27.7555	53.195917	−27.755498	JS	15.32	—	30.42	−18.98
JADES-GS-53.14988-27.7765	53.149881	−27.776503	JS	13.41	13.274	29.83	−18.96
JADES-GS-53.16863-27.79276	53.168628	−27.792759	JS	11.71	—	29.49	−18.95
JADES-GN-189.2432+62.21009	189.243201	62.210094	JN	9.72	—	29.36	−18.95
JADES-GS-53.05177-27.88727	53.051769	−27.887272	JS	9.51	—	29.35	−18.91
JADES-GS-53.12903-27.85492	53.129030	−27.854924	JS	10.66	—	29.59	−18.90
JADES-GS-53.12692-27.89778	53.126918	−27.897781	JSm	10.76	—	29.77	−18.86
JADES-GS-53.09748-27.85698	53.097475	−27.856984	JS	9.64	—	29.61	−18.84
JADES-GS-53.12025-27.88573	53.120253	−27.885728	JSm	9.68	—	29.28	−18.80
JADES-GS-53.18057-27.7455	53.180572	−27.745496	JS	11.47	—	29.68	−18.72
JADES-GS-53.1985-27.79675	53.198498	−27.796753	JSm	9.72	—	29.44	−18.71
$L/L_{z=3}^* = 0.048$ –0.12							
JADES-GS-53.11375-27.88316	53.113749	−27.883159	JSm	10.4	—	29.28	−18.68
JADES-GN-189.27797+62.20034	189.277970	62.200342	JN	11.23	—	29.45	−18.66
JADES-GS-53.10763-27.86014	53.107626	−27.860139	JS	14.44	—	30.48	−18.65
JADES-GS-53.15637-27.74844	53.156375	−27.748444	JS	10.22	—	29.65	−18.65
JADES-GS-53.02868-27.89301	53.028683	−27.893012	JS	12.39	—	29.84	−18.61
JADES-GS-53.12297-27.89089	53.122972	−27.890891	JSm	11.69	—	29.91	−18.61
JADES-GS-53.08138-27.8858	53.081379	−27.885803	JSm	11.72	—	30.14	−18.61
JADES-GS-53.06568-27.84119	53.065678	−27.841188	JSm	11.73	—	29.65	−18.60
JADES-GS-53.06671-27.87783	53.066706	−27.877826	JSm	10.22	—	29.32	−18.55
JADES-GS-53.09208-27.85278	53.092076	−27.852783	JS	10.68	—	29.84	−18.55
JADES-GS-53.06475-27.89024	53.064754	−27.890238	JS	14.0	—	30.16	−18.54
JADES-GS-53.16553-27.82303	53.165528	−27.823027	JS	9.96	—	29.88	−18.51
JADES-GN-189.32099+62.18479	189.320992	62.184791	JN	10.34	—	29.54	−18.50
JADES-GN-189.34241+62.15816	189.342411	62.158156	JN	10.56	—	29.73	−18.49

Table A.2 *continued*

Table A.2 (*continued*)

ID	R.A.	Decl.	field	z_{photo}	z_{spec}	$m_{\text{UV}}^{(\text{ap})}$	M_{UV}
	(deg)	(deg)				(mag)	(mag)
(1)	(2)	(3)	(4)	(5)	(6)	(7)	(8)
JADES-GN-189.30304+62.16551	189.303038	62.165511	JN	11.68	—	29.84	−18.47
JADES-GN-189.25292+62.2362	189.252917	62.236195	JN	10.74	—	29.43	−18.46
JADES-GS-53.06131-27.81951	53.061314	−27.819506	JS	9.86	—	29.78	−18.46
JADES-GS-53.14159-27.87173	53.141588	−27.87173	JSm	9.92	—	29.59	−18.45
JADES-GS-53.04813-27.86053	53.048134	−27.860527	JSm	10.73	—	29.83	−18.45
JADES-GN-189.22825+62.22154	189.228245	62.221540	JN	10.42	—	29.54	−18.43
JADES-GS-53.15883-27.7735	53.158829	−27.773498	JS	10.84	10.420	29.59	−18.42
JADES-GS-53.05715-27.81617	53.057155	−27.816173	JSm	10.25	—	29.35	−18.39
JADES-GS-53.07607-27.85602	53.076073	−27.856023	JS	9.62	—	29.78	−18.34
JADES-GS-53.20065-27.79802	53.200650	−27.798022	JSm	11.71	—	30.43	−18.32
JADES-GN-189.20016+62.18314	189.200159	62.183138	JN	9.94	—	30.11	−18.29
JADES-GN-189.32172+62.19397	189.321719	62.193966	JN	10.5	—	99.99	−18.29
JADES-GS-53.14673-27.77901	53.146726	−27.779009	JS	13.68	—	30.42	−18.28
JADES-GN-189.33638+62.16733	189.336380	62.167326	JN	12.53	—	29.82	−18.27
JADES-GN-189.30384+62.15493	189.303836	62.154925	JN	10.19	—	29.82	−18.27
JADES-GS-53.12239-27.78814	53.122385	−27.788141	JS	11.5	—	30.94	−18.24
JADES-GN-189.22712+62.14806	189.227122	62.148063	JN	9.85	—	29.64	−18.24
JADES-GS-53.21339-27.76951	53.213386	−27.76951	JS	11.13	—	30.70	−18.21
JADES-GN-189.26099+62.20112	189.260990	62.201124	JN	9.85	—	29.48	−18.21
JADES-GS-53.079-27.86359	53.079003	−27.86359	JS	10.5	—	30.34	−18.20
JADES-GS-53.18602-27.81748	53.186023	−27.81748	JS	10.03	—	30.00	−18.20
JADES-GS-53.1485-27.74159	53.148504	−27.741589	JS	11.2	—	30.20	−18.20
JADES-GS-53.10469-27.86187	53.104686	−27.861872	JSm	12.27	—	30.37	−18.19
JADES-GN-189.26695+62.20538	189.266955	62.205384	JN	10.33	—	29.64	−18.18
JADES-GS-53.09789-27.90578	53.097895	−27.905785	JSm	9.68	—	30.10	−18.16
JADES-GS-53.07477-27.84542	53.074768	−27.845421	JS	9.92	—	30.18	−18.15
JADES-GS-53.14501-27.87926	53.145007	−27.879264	JSm	10.76	—	29.82	−18.14
JADES-GS-53.17847-27.75591	53.178469	−27.755909	JS	15.13	—	30.85	−18.13
JADES-GS-53.09872-27.8602	53.098718	−27.860204	JS	10.69	—	30.49	−18.12
JADES-GS-53.13506-27.79161	53.135065	−27.791608	JS	11.24	—	30.16	−18.12
JADES-GS-53.17301-27.80085	53.173013	−27.800852	JS	11.28	—	30.64	−18.12
JADES-GS-53.08468-27.86666	53.084682	−27.866663	JS	12.48	—	30.35	−18.12
JADES-GS-53.03138-27.87219	53.031381	−27.872188	JS	10.65	—	30.33	−18.11
JADES-GS-53.09967-27.87844	53.099670	−27.878442	JSm	10.68	—	30.12	−18.08
JADES-GS-53.13871-27.819	53.138705	−27.819003	JS	10.05	—	30.12	−18.07
JADES-GS-53.17345-27.81217	53.173448	−27.812166	JS	9.58	—	29.64	−18.07
JADES-GS-53.08188-27.84431	53.081885	−27.844315	JS	10.46	—	30.73	−18.06
JADES-GS-53.07901-27.87154	53.079012	−27.871536	JS	11.97	—	30.31	−18.05
JADES-GS-53.14124-27.80343	53.141244	−27.803431	JS	10.38	—	30.51	−18.04

Table A.2 *continued*

Table A.2 (*continued*)

ID	R.A.	Decl.	field	z_{photo}	z_{spec}	$m_{\text{UV}}^{(\text{ap})}$	M_{UV}
	(deg)	(deg)				(mag)	(mag)
(1)	(2)	(3)	(4)	(5)	(6)	(7)	(8)
JADES-GN-189.31881+62.18663	189.318808	62.186627	JN	10.76	—	30.27	−18.04
JADES-GS-53.06006-27.89143	53.060058	−27.891429	JS	10.92	—	29.88	−18.04
JADES-GN-189.28836+62.22878	189.288362	62.228776	JN	9.59	—	29.86	−18.03
JADES-GS-53.02619-27.88716	53.026185	−27.887162	JS	11.35	—	30.26	−18.03
JADES-GS-53.07557-27.87268	53.075568	−27.872677	JS	15.31	—	31.53	−18.02
JADES-GN-189.24505+62.21991	189.245048	62.219905	JN	10.09	—	30.01	−17.98
JADES-GS-53.1551-27.75395	53.155100	−27.753951	JS	10.29	—	30.39	−17.97
JADES-GS-53.16874-27.81698	53.168738	−27.816975	JS	9.92	—	30.36	−17.95
JADES-GS-53.06235-27.84774	53.062349	−27.847743	JSm	10.18	—	29.85	−17.92
JADES-GS-53.17153-27.84392	53.171530	−27.843922	JS	9.92	—	30.35	−17.92
JADES-GN-189.15382+62.21145	189.153820	62.211454	JN	9.71	—	29.77	−17.91
JADES-GS-53.04017-27.87602	53.040167	−27.876022	JS	11.92	—	30.33	−17.90
JADES-GS-53.08537-27.85047	53.085365	−27.850474	JS	9.69	—	29.92	−17.90
JADES-GS-53.02804-27.86158	53.028043	−27.861585	JSm	9.74	—	99.99	−17.87
JADES-GS-53.13918-27.78273	53.139184	−27.782726	JS	10.49	—	30.45	−17.85
JADES-GS-53.07277-27.85209	53.072767	−27.852093	JS	9.88	—	30.81	−17.84
JADES-GS-53.04887-27.89045	53.048871	−27.890447	JS	9.61	—	30.11	−17.83
JADES-GS-53.07248-27.85535 ^{†1}	53.072480	−27.855352	JS	10.6	—	30.24	−17.81
JADES-GS-53.13018-27.89975	53.130183	−27.899752	JSm	10.62	—	99.99	−17.80
JADES-GS-53.12737-27.81805	53.127367	−27.818052	JS	10.71	—	30.41	−17.80
JADES-GS-53.13639-27.81306	53.136386	−27.813064	JS	11.01	—	30.33	−17.79
JADES-GS-53.16627-27.81377	53.166270	−27.813766	JS	11.46	—	30.34	−17.79
JADES-GS-53.17016-27.82454	53.170158	−27.824542	JS	10.7	—	30.50	−17.79
JADES-GN-189.31828+62.20169	189.318282	62.201687	JN	11.53	—	30.46	−17.79
JADES-GS-53.09871-27.86016	53.098714	−27.860157	JS	9.59	—	30.73	−17.78
JADES-GS-53.10484-27.86807	53.104839	−27.868072	JSm	9.94	—	29.84	−17.78
JADES-GS-53.18129-27.81043	53.181291	−27.810427	JS	12.52	—	30.20	−17.75
JADES-GS-53.13274-27.7967	53.132735	−27.796699	JS	10.47	—	30.04	−17.71
JADES-GN-189.27007+62.21786	189.270070	62.217863	JN	10.53	—	30.37	−17.70

NOTE— The values presented in this table have been obtained in [Hainline et al. \(2024\)](#) and [Carniani et al. \(2024a\)](#), except for the 4th column and 7th column. (1) Object ID. (2) Right ascension. (3) Declination. (4) Field flag. JS, JSm, and JN indicate that the object is located in JADES Deep, JADES Medium, and JADES GOODS-N, respectively. (5) Photometric redshift. (6) Spectroscopic redshift. (7) Aperture magnitude measured in a $0''.2$ diameter circular aperture. For $z < 13$, F200W images are used, and for $z > 13$, F277W images are used. (8) Total absolute UV magnitude.

^{†1} JADES 67592 ([Kocevski et al. 2024](#)).

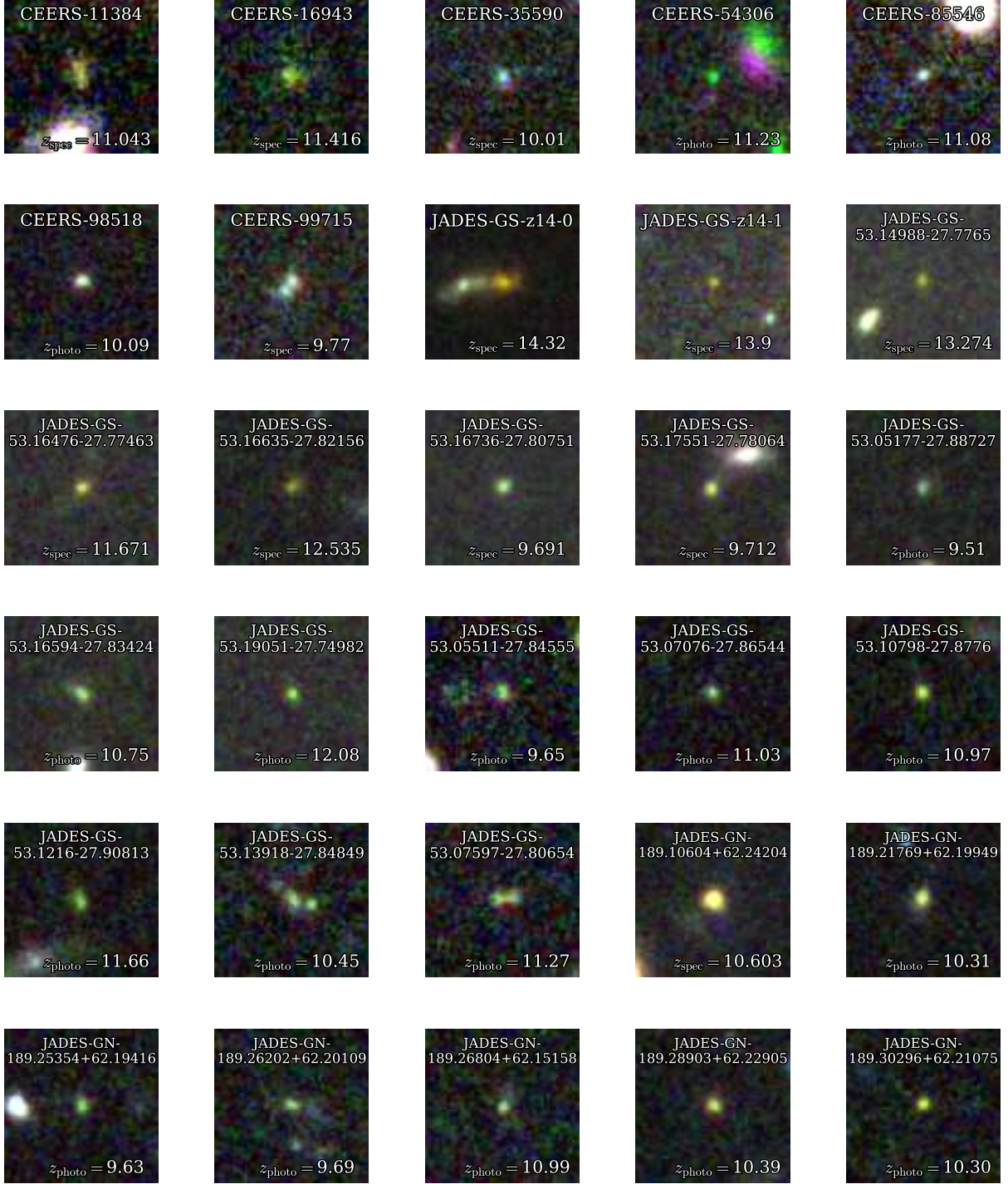


Figure A.1. Pseudo-color images of the $z \sim 10$ – 16 galaxies analyzed in this study, for which the aperture magnitude $S/N > 10$ and individual surface brightness profile fitting is successfully performed with GALFIT. Blue, green, and red represent the F150W, F200W, and F277W images, respectively. For spectroscopically confirmed galaxies, their spectroscopic redshifts are indicated, while photometric redshifts are provided for the others. Each image has a size of $1''.5 \times 1''.5$.